HOLLOW MULTI-SHELLED STRUCTURED TiO_2/$MAPbI_3$ COMPOSITES: PREPARATION AND APPLICATION IN PHOTOCATALYTIC HYDROGEN EVOLUTION

By

Wensheng Han

Hollow Multi-shelled Structured TiO_2/$MAPbI_3$ Composites: Preparation and Application in Photocatalytic Hydrogen Evolution

By

Wensheng Han

A Ph.D. Thesis Submitted to the

Division of Environment Engineering Science

Graduate School of Science and Technology,

Gunma University

Japan

Supervisor: Professor Dan Wang

Professor Nobuyoshi Nakagawa

August 2022

Contents

Abstract

During the development of industries and technologies, energy consumption is sharply increasing in the recent hundred years. Solar energy is considered to be one of the potential renewable energy sources. The utilizations of solar energy are classified as photothermal, photocatalytic, and photovoltaic. With fossil energy consumption, the emission of carbon dioxide is also corresponding to growth. Hydrogen with the advantages of clean energy and environmentally friendly has been widely studied. Photocatalytic hydrogen generation is realized by photocatalysts under light illumination. In this thesis, loading narrow bandgap semiconductors as a light sensitizer inside hollow multi-shelled structures provides a way to improve photocatalytic activity. To improve photocatalytic efficiency, heterogeneous interfaces are constructed to improve charges separation. Design and synthesis of heterogeneous interfaces between TiO_2 hollow multi-shelled structures and $MAPbI_3$ perovskite were carried out in the first. Then the $MAPbI_3/Pt/TiO_2$ composites were applied in the photocatalytic hydrogen evolution reaction. The impacts of morphology and heterogeneous interfaces of photocatalysts on photocatalytic performance have been studied. Besides, to optimize electron transfer from $MAPbI_3$ to TiO_2 surface, the different phase ratios of anatase and rutile were synthesized and used for photocatalytic reaction. The following are the main contents in detail:

(1) In the past decade, numerous studies have been made on the design and synthesis of hollow structures, including different compositions and geometric characteristics. The synthesis of hollow structures by sequential templating approach (STA) is universal and widely applicable, especially in hollow multi-shelled structures. The pretreatment of carbonaceous microspheres is a very important step in the STA synthesis process. The pretreatment process affects the surface morphology and the surface groups of carbonaceous microspheres. In this chapter, the pretreatment of carbonaceous microspheres by ethanol was studied. With the prolongation of pretreatment time, the pore size of the carbon sphere increases. Turning the adsorption duration time, pretreatment duration time, and heating rate can control the shells number of TiO_2. And the morphology and phase of obtained TiO_2 HoMSs samples were characterized by XRD, Raman, XPS, TEM, and SEM. Besides, the composite photocatalysts of methylammonium lead iodide perovskite ($MAPbI_3$) within TiO_2 hollow multi-shelled structures (HoMSs) were designed and synthesized.

(2) Interfacial photogenerated charge separation and transport have been demonstrated as a great impactor on photocatalytic performance. The results indicate that the heterogenous

interface of $MAPbI_3/TiO_2$-HoMSs can efficiently promote the separation of photogenerated carriers. Thanks to the thin shell structure, it can also reduce the transmission distance of the carriers to reduce the charge recombination and improve the charge utilization. Additionally, HoMSs assembled with multiple shells can support abundant available surfaces for building heterogeneous interfaces and photocatalytic reactions. As a result, samples of $MAPbI_3$/Pt/triple-shelled TiO_2 hollow structure displayed an H_2 evolution rate of 6856.2 μmol h^{-1} g^{-1} under visible-light illumination, which is much faster than that of Pt/$MAPbI_3$ (268.6 μmol h^{-1} g^{-1}).

(3) Optimizing electrons transfer is contributed to improving photocatalytic performance in hydrogen evolution. The electrons transfer pathways of $MAPbI_3$/Pt/TiO_2 HoMSs include $MAPbI_3$ bulk, interfaces of $MAPbI_3$ and TiO_2 HoMSs, TiO_2 bulk, interfaces of TiO_2 and cocatalyst. Rutile TiO_2 and anatase TiO_2 show differences in interface transfer and TiO_2 bulk transfer. To investigate the influence of rutile TiO_2 and anatase TiO_2 on electrons transfer, the different anatase ratios of TiO_2 are synthesized by calcined at different temperatures. The contrast of electrons transport between anatase and rutile was characterized by EIS, transient photocurrent response, and linear sweep voltammetry method. The experimental results prove that electrons transfer in $MAPbI_3$/anatase is faster than $MAPbI_3$/rutile. $MAPbI_3$/anatase possesses smaller transfer resistance and higher transient photocurrent value. Compared with the faster interface transport, the faster bulk transport in anatase is possibly beneficial to improving performance.

List of Figures

List of Tables

List of Acronyms/Abbreviations

Acronyms/Abbreviations	Full Spelling
AQE	Apparent Quantum Efficiency
BT	Bulk Transfer
CB	Conduction Band
CBM	Conduction Band Minimum
CMSs	Carbonaceous Microspheres
DMF	N,N-dimethyl Formamide
DMSO	Dimethyl Sulfoxide
EIS	Electrochemical Impedance Spectroscopy
FT-IR	Fourier Transform Infrared Spectrums
HER	Hydrogen Evolution Reaction
HoMSs	Hollow Multi-shelled Structures
HRTEM	High Resolution Transmission Electron Microscopy
ICP	Inductively Coupled Plasma
IT	Interface Transfer
MAI	Methylamine Iodide
$MAPbI_3$	Methylammonium Lead Iodide Perovskite
NHE	Normal Hydrogen Electrode
OER	Oxygen Evolution Reaction
OWS	Overall Water Splitting
SAED	Selected Area Electron Diffraction
SEM	Scanning Electron Microscopy

STA	Sequential Templating Approach
STH	Solar-to-hydrogen Transfer Efficiency
TEM	Transmission Electron Microscopy
UPS	Ultraviolet Photoelectron Spectroscopy
VB	Valence Band
VBM	Valence Band Maximum
XPS	X-ray Photoelectron Spectroscopy
XRD	X-ray Diffraction
0 D	Zero Dimension
1 D	One Dimension
2 D	Two Dimension
3 D	Three Dimension

CHAPTER 1.

Introduction

1.1 Overview of Photocatalytic Water Splitting

1.1.1 Background

The shortage of energy is one of the major problems that humans facing now while energy consumption is sharply increased during the recent one hundred years. Traditional non-renewable energy, such as coal, gasoline, and natural gas, is insufficient to meet the needs of social progress and development. At the same time, emissions generated from conventional resources are polluting the climate and environment. The development of clean and renewable energy is the key to solving the ever-increasing demand for energy. Clean energy provides an effective way to solve the environmental pollution caused by the burning of fossil fuels. Clean and renewable energy includes six categories, such as wind power, solar energy, geothermal energy, ocean energy, hydropower, and biomass-waste energy. Solar power is extensively accepted as a sustainable, continuous, and renewable clean energy that can satisfy the needs of mankind at present and in the future. Therefore, the efficient use of solar energy is necessary.

Sunlight has been utilized as thermal (heat engine or process heating), photochemical (photosynthesis), and photophysical (photovoltaic).[1] Photo chemically applications include photocatalytic chemical synthesis, photosynthesis, photocatalytic carbon reduction, and photocatalytic water splitting. Despite the natural photosynthesis-inspired photocatalysis,[2] there are some differences between photosynthesis and photocatalysis. In a general way, a material drives a thermodynamic increase reaction by light as energy force (positive Gibbs free energy change, $\Delta G > 0$), this process is defined as photosynthesis. When photons participate in the reaction process as a reactant, the material is defined as a "photocatalyst". At the same time, the photocatalyst after light illumination changes the kinetics of the reaction instead of changing the thermodynamics of the reaction.[3] The concept of catalyst is defined as a material able to produce chemical transformations of the reaction partners after

absorption of light by “the International Union of Pure and Applied Chemistry”.

Photocatalytic water-splitting is known as an effective way to ameliorate both the shortage of non-renewable resources and environmental pollution problems. According to different photocatalysts, hydrogen or oxygen or both will generate after the photocatalytic water-splitting process. Hence, three kinds of splitting situations in the research may happen, including hydrogen evolution reaction (HER), oxygen evolution reaction (OER), and overall water splitting (OWS). Hydrogen is known as a higher heating value of combustion fuel and clean energy. The bond strength of the H-H bond is about 435 $kJ \cdot mol^{-1}$ in the diatomic molecule.[4] Owing to the higher heating value of combustion, hydrogen has been applied in many fields, including spacecraft, fuel cell cars, and generating electricity. Hence, hydrogen will become the most potential energy in the future because of its environmental and friendly, renewable, and higher heating value of combustion advantages.

1.1.2 The Principle of Photocatalytic Water-Splitting

In 1972, Akira Fujishima and Kenichi Honda have reported a paper in Nature about water splitting.[5] The experiment results indicated that the OER occurs at the TiO_2 electrode and HER at the platinum black electrode when illuminated in ultraviolet light. The water splitting reaction equation is as follows:

$$TiO_2 + 2hv \rightarrow 2e^- + 2h^+ \quad (1)$$

$$\text{OER: } H_2O + 2(h^+) \rightarrow O_2 + 2H^+ \qquad E_{ox} = -1.23\ eV\ for\ pH = 0 \quad (2)$$

$$\text{HER: } 2H^+ + 2e^- \rightarrow H_2 \qquad E_{red} = 0.0\ eV \quad (3)$$

$$\text{Overall reaction: } H_2O \rightarrow {}^1/_2\, O_2 + H_2 \quad \Delta G = 237\ kJ \cdot mol^{-1}\ \ E_{overall} = 1.23\ eV \quad (4)$$

The water-splitting process is a process of uphill Gibbs free energy change. In the following research, the reactions principle of HER and OER has been confirmed. Figure 1.1 shows the relationship between semiconductor band position and reaction energy position.[6] In the HER process, the conduction band minimum potential of catalyst is a more negative potential than H^+/H_2 hydrogen reduction potential ($E_{red} = 0 - 0.059$ pH, V versus NHE). In the OER process, the valence band maximum potential of catalyst is more positive than the oxygen oxidation potential ($E_{red} = 1.23 - 0.059$ pH, V versus NHE). And in the OWS process, the energy band is required to meet both HER and OER. When the light is absorbed by a photocatalyst, the electrons are transferred to the conduction band (CB) and holes are generated in the valance band (VB). The holes in the VB combine with water to generate oxygen and hydrogen ions.

The excited electrons in the CB combine with hydrogen ions to generate hydrogen.

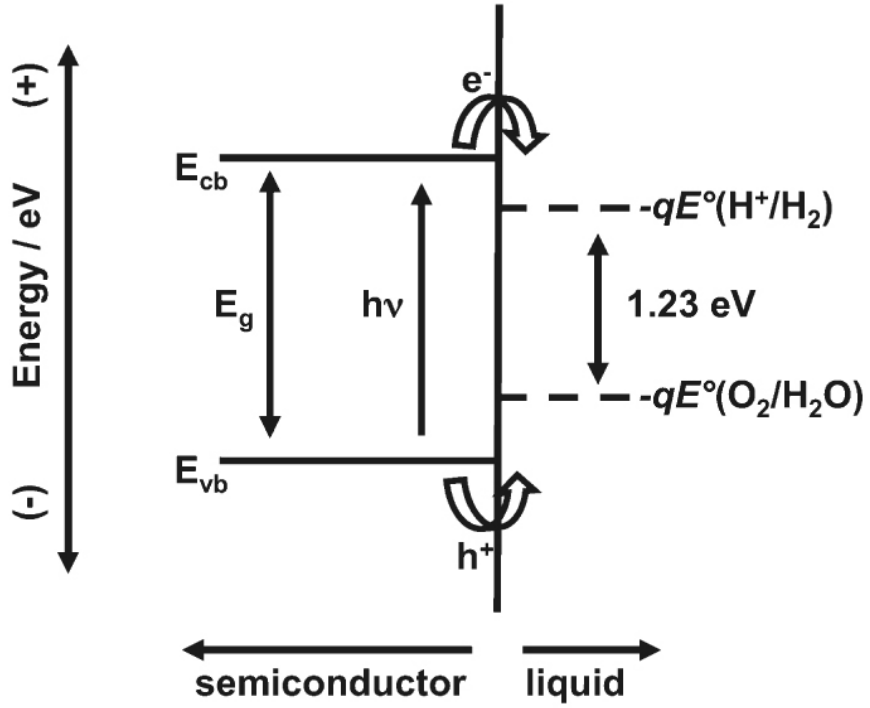

Figure 1.1 The band position and electrochemical potentials of ideal photocatalysts splitting water under light illumination are represented by the absolute energy scale. Left axis for E_{cb} and E_{vb} and the electrochemical potentials for $qE°$.[6]

1.1.3 Main Processes of Photocatalytic HER

During photocatalytic research of past decades, the photocatalytic water splitting processes are gradually cleared and corresponding optimization strategies are constantly put forward. The main processes of photocatalytic OWS are shown in figure 1.2.[7] In the first step, light is captured by a photocatalyst then excited charges are generated. Next, the excited photogenerated electrons and holes are separated and transferred into the photocatalyst surface reactive sites or cocatalyst. The partial excited electrons and holes may recombine in the bulk or defects. In the end, the electrons and holes participate chemical HER and OER in the photocatalyst surface or co-catalyst. Hence, the influence factors of photocatalytic activity mainly include light absorption, charges separation and transfer, and surface chemical reactions.

1.1.4 Performance Evaluation Parameters

The performance evaluation parameters mainly include hydrogen evolution volume (hydrogen evaluation rate), splitting efficiency, apparent quantum efficiency (AQE), and

photocatalysts stability. The hydrogen evolution volume, splitting efficiency, and apparent quantum efficiency (AQE) are used to evaluate photocatalytic activity. Besides photocatalytic activity and AQE, the excellent photocatalysts should have preeminent long-term steady H_2 and/or O_2 photocatalytic performance. To measure the stability of photocatalysts, repeatability test or long-term experiments is always necessary.[8]

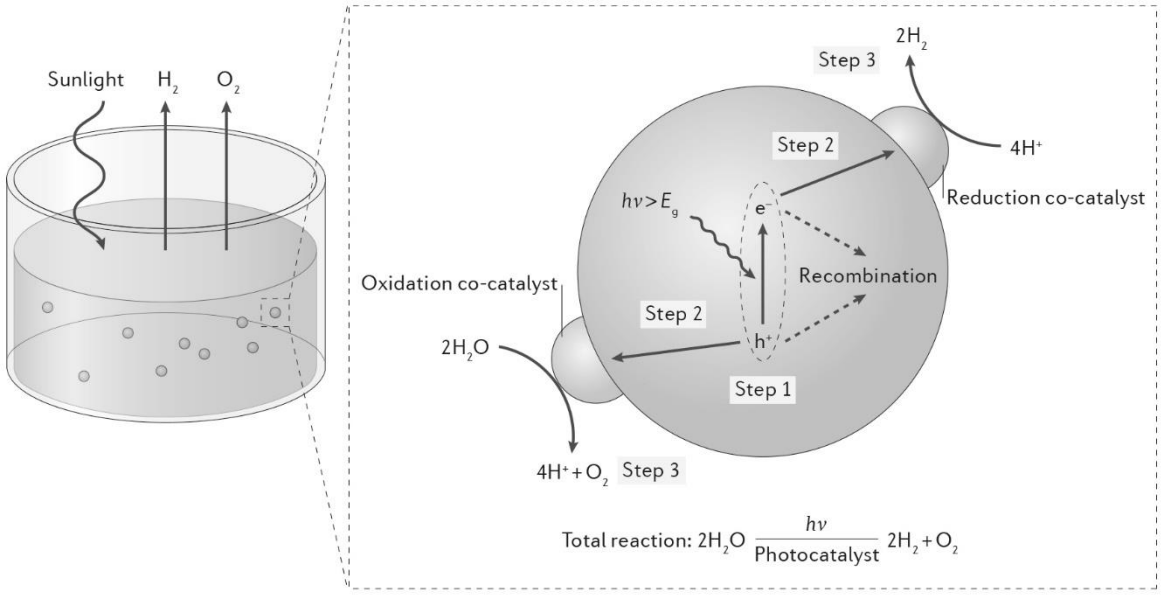

Figure 1.2 Schematic illustration of the main processes of the OWS reaction.[7]

1.2 Photocatalytic HER Performance Optimization Strategies

1.2.1 Light Absorption Optimization Strategies

According to literature reported,[9] the quantum efficiency approaches to 100 % when absorption range up to 400 nm, the solar-to-hydrogen conversion efficiency (STH) is limited to 2 % in theory. But when absorption range up to 700 nm or 1000 nm and quantum efficiency up to 100 %, the theoretically limited solar-to-hydrogen conversion efficiency is 25 % or 47 %. Hence, enhancing light wavelength absorption range (up to visible light) is beneficial to obtaining higher STH. But many oxides semiconductor photocatalysts cannot meet the appropriate more negative CB for hydrogen reaction and lower bandgap to adsorb visible light as shown in the figure 1.3A. Therefore, to achieve better HER performance, narrow bandgap photocatalysts with a wide light absorption wavelength range have been studied. Up to now, there are many strategies applied to improve light absorption wavelength range, such as nonmetal doping,[10-11] mental doping,[12-14] solid solutions,[15-16] dye sensitization,[17] localized surface plasmon resonance effect,[18] quantum confinement effect,[19] Z-Scheme configurations,[20-22] and corresponding principles is shown in the figure 1.3.[9]

The nonmetal doping strategy is realized through doping nonmetal elements, such as nitrogen, sulfur, and halogen.[23] As shown in figure 1.3B, the hybridization of nonmetallic elements with valence bands makes the VB closer to the CB. Different from nonmetal doping, metal doping is also widely applied in enhancing visible light absorption by narrowing bandgap. The principle of bandgap variation of photocatalysts doped by metal elements is different from photocatalysts doped by nonmetal elements. The metal doping strategy is carried out by creating impurity levels in the forbidden band of the semiconductor.[8] It is worth noting that catalysts doped by metal also present valence band potential variation, such as copper.[24] But the variation mechanism of valence band doped by metal elements is different from nonmetallic elements doping. In the metal doping strategies, there is a donor level above the original valence band in the forbidden band as shown in figure 1.3C. Similar to the donor lever, narrowing the bandgap may cause by an acceptor level below the original conduction band in the forbidden band after being doped with metal elements. The solid solution strategy always needs two kinds of semiconductors with a narrow bandgap and a wide bandgap as shown in the figure 1.3D. The orbital hybridizations between different atoms come from two kinds of semiconductors with narrow bandgap.[15] the bandgap width and valence/ conduction band position can be controlled by changing the proportion of the wide bandgap semiconductor and the narrow semiconductor.[25]

The dye sensitization strategy is inspired by dye-sensitized solar cells reported by Michael Grätzel in 1991.[26] In the dye-sensitized solar cells, the dye as a light sensitization adsorbs visible light to generate photoelectrons. The photoelectrons transfer into semiconductor CB from dye CB as shown in figure 1.3E. Reasonable values of VB and CB are required for this strategy. Similar to the dye sensitization strategy, the quantum confinement effect also possesses a semblable transfer pathway of electrons. The quantum dot plays a role of light sensitizer for visible light. The photoelectrons transfer into the CB of wide bandgap semiconductor from the VB of the quantum dot as shown in figure 1.3G. The localized surface plasmon resonance effect is defined as a phenomenon that the absorption band generated while the incident photon frequency resonates with the collective oscillation of the electrons in the conduction band.[27] The electrons derived from nano particles inject into the CB of wide bandgap semiconductor then participated in the next reaction as shown in figure 1.3F. The Z-scheme configuration is constructed by two narrow bandgap photocatalysts as shown in figure 1.3H. When the semiconductor type II is illuminated under visible-light, the photogenerated electrons are excited to the CB of type II and then transfer into the VB of the semiconductor

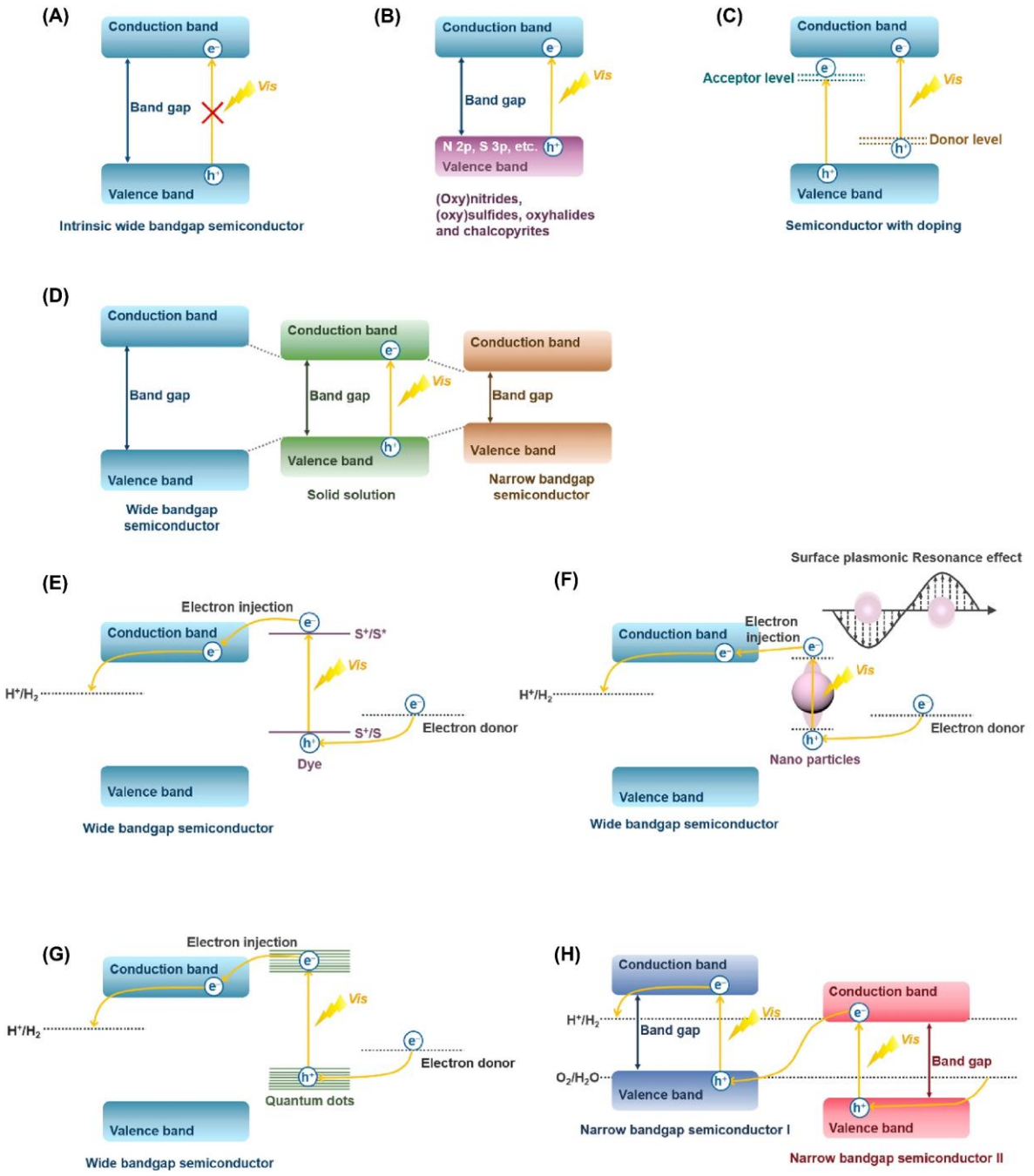

Figure 1.3 Schematics energy band adjusted by optimization strategies: (A) Catalysts with a wide bandgap, (B) Nonmetallic doping, (C) Metal doping, (D) Solid solution, (E) Dye sensitization, (F) Surface plasmon resonance, (G) Quantum confinement effect, and (H) Z-scheme configuration.[9]

type I. Meanwhile, the electrons in the VB of semiconductor type I are excited into CB of semiconductor type I under visible light. The electrons are rich in the CB of semiconductor type I and the holes are rich in the VB of semiconductor type II.[28] This kind of configuration promotes effective charges separation and suppresses recombination.[29]

1.2.2 Charges Separation and Transfer Optimization Strategies.

The photogenerated charge separation and transfer process are very important for efficient photocatalysts. During the past decades, there are mainly five kinds of strategies for optimizing charges utilization, including facet control,[30-31] creating junctions,[32] defect engineering,[33] cocatalyst loading,[34] short charge carrier transfer distances.[35]

(1) Controlling crystal facets

The crystal facet control resulting in surface atom structure can tune electronic band structure, surface redox sites, surface free energy, reactant adsorption, product desorption, and charge transfer and separation.[36] Generally speaking, ferroelectric field or/and polar surface terminations in semiconductors build an internal electric field through band bending between different Fermi levels. The internal electric fields in the semiconductor drive photoinduced charges in different directions and lead to the fast separation of photogenerated electrons and holes.[37] A research about BiOCl single-crystalline nanosheets exposed with different facets is reported as shown in figure 1.4A.[38] the direction of internal electric fields are parallel to the (010) facet of nanosheets BOC and perpendicular to the (001) facet of BOC. The internal electric field in the (001) facet of BOC is facilitating electrons transport and transfer with a shorter diffusion distance.

(2) Constructing junctions

The fabrication of junctions is an effective and common strategy for charges separation and transfer. Although many heterojunctions (Schottky junction, Z-scheme heterojunction, type I heterojunction, type II heterojunction, p-n heterojunction, and S-scheme heterojunction) have been developed, the different junctions have one thing in common. The electrons generated from one semiconductor transfer into another semiconductor.[39] Hence, the junctions are beneficial to electrons separation and depress recombination. The fabrication of junctions discusses detailly in the next 1.2.4 section.

(3) Creating engineering

The defects engineering is more complex compared with other strategies. The defects or impurity states are usually the recombination center in the electron transfer process. The enhancing crystallinity steps through calcined in a special atmosphere or reducing impurities in the semiconductor are effective methods.[40] For example, the photocatalytic HER activity of g-C_3N_4 is reduced by defects as shown in the figure 1.4B.[41] The two types of defects (above

VBM and below CBM of g-C_3N_4) provide recombination sites that reduce the concentration of electrons and holes. But in some situations, introducing defects can improve HER performance because shallow trapping sites defects improve charge separation.[42]

(4) Shortening transfer distance

Except for the defect traps and charges separation driving force, the charges transfer distance affects whether the charges can transfer from bulk to surface before quencher. The effective method is to shorter the charges transfer distance from the bulk to the surface. The different semiconductor materials have different diffusion lengths for electrons and holes. For example, the electrons diffusion length of hybrid perovskite $MAPbI_3$ materials is almost 1 micrometer.[44] As shown in the figure 1.4C, if the radius of $MAPbI_3$ materials (R) is smaller than the diffusion length (L_D, 1 micrometer), the electrons can transfer from center to surface. In contrast, the radius of $MAPbI_3$ materials is larger than 1 micrometer, and the electrons

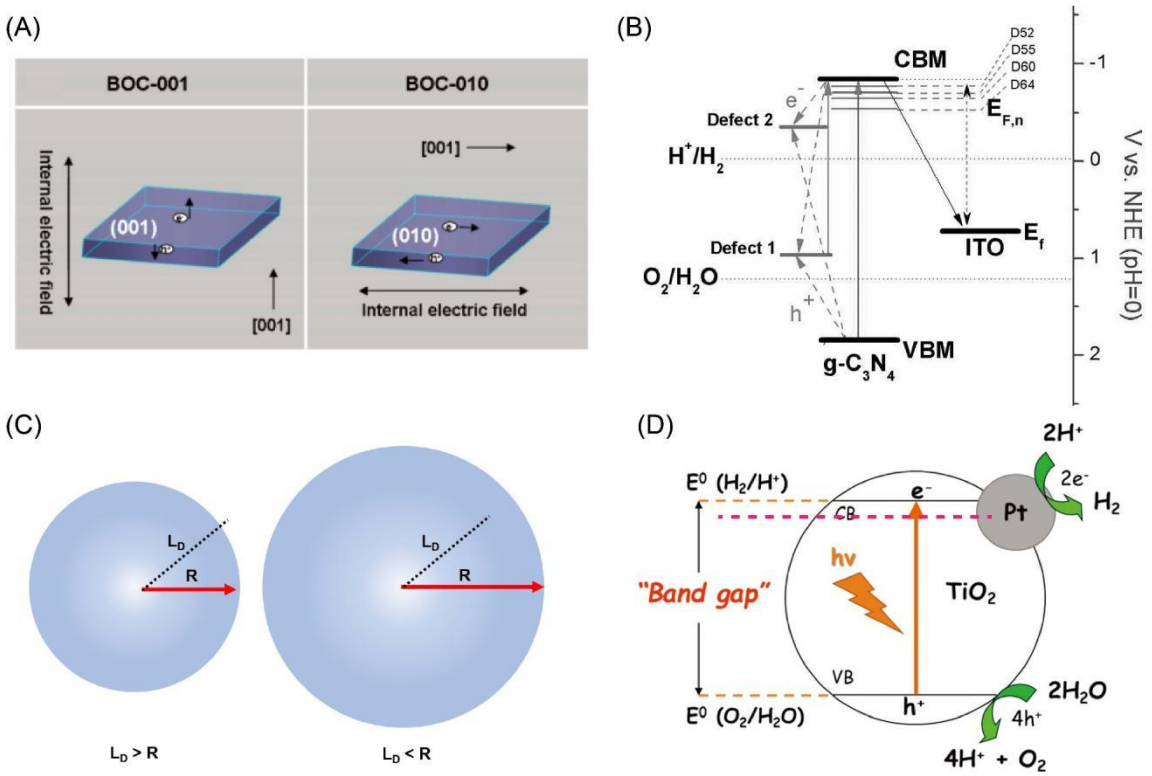

Figure 1.4 Illustration of the effects of optimization strategies on charges separation and transfer**:** (A) The internal electric field of the BOC single-crystalline nanosheets;[38] (B) Effect of defects on energy alignment of g-C_3N_4;[41] (C) Effect of particle sizes on charges transfer, L_D presents diffusion length and R presents radius of the particle; (D) Schematic band energy level diagram of Pt/TiO_2 photocatalyst.[43]

generated in the center of materials cannot transfer to the surface. It is worth noting that an extremely smaller size of particles possibly absorbing insufficient light causes reducing the number of photogenerated charges. Hence, applying the two-dimensional materials and hollow structures materials as photocatalysts have been attracts researcher's attention.[45-46]

(5) Loading cocatalysts

Loading cocatalysts on photocatalysts as reactive sites is one of the optimization strategies. The cocatalysts include noble metal cocatalysts (Au, Pd, Pt)[47-49] and noble metal cocatalysts (Fe, Co, Ni, Cu).[43, 50-51] The cocatalyst offers trapping sites for the photogenerated electrons in reducing cocatalyst or holes in oxidizing cocatalyst. The trapping sites promote the charges separation and then enhance apparent quantum efficiency. For example, when cocatalyst Pt is deposited on TiO_2 photocatalyst, the photogenerated electrons are trapped by Pt cocatalyst because the Fermi energy level of Pt cocatalyst is below the conduction band of TiO_2 photocatalyst as shown in the figure 1.4D.[34, 43] Therefore, loading cocatalysts can promote charges separation and depress photogenerated charges recombination.

1.2.3 Surface Reactions Optimization Strategies

The photogenerated electrons and holes take part in photocatalytic reactions on the surface of photocatalysts. The forward photocatalytic water splitting can generate H_2 and O_2. At the same time, there is a possibility that the generated H_2 and O_2 react rapidly on the surface of cocatalyst.[52-53] The backward reaction is satisfied the thermodynamic conditions of the generation of H_2O.[53] Therefore, the H_2O can be obtained in the backward reaction from gaseous H_2 and O_2. Hence, to depress backward reaction, there are three strategies promoted to solve this situation, including loading cocatalysts, surface modification, and morphology design.

The loading cocatalysts strategy is beneficial to accelerate the surface chemical reaction. The cocatalysts can reduce the activation energy when cocatalysts catalyze the reactions as shown in figure 1.5A.[34] Loading of oxidizing cocatalyst on the photocatalyst reduces the activation energy (E_a) of the water oxidation process.[34] For the surface modification strategies, the surface can be modified by organic groups or compounds such as semiconductor polymer, elementary substance, and metal oxide. The surface modified by organic groups is beneficial to the desorption of generated gases from the surface.[54] While modifying the surface by compounds forms a core-shell-like structure which presents contact between cocatalysts and generated gases.[55-57] For example, The iodine was adsorbed on the surface of cocatalyst Pt as

shown in figure 1.5B.[52] The shell layer of iodine formed on the Pt surface suppresses backward reaction because the Pt cocatalysts surface is untouchable.

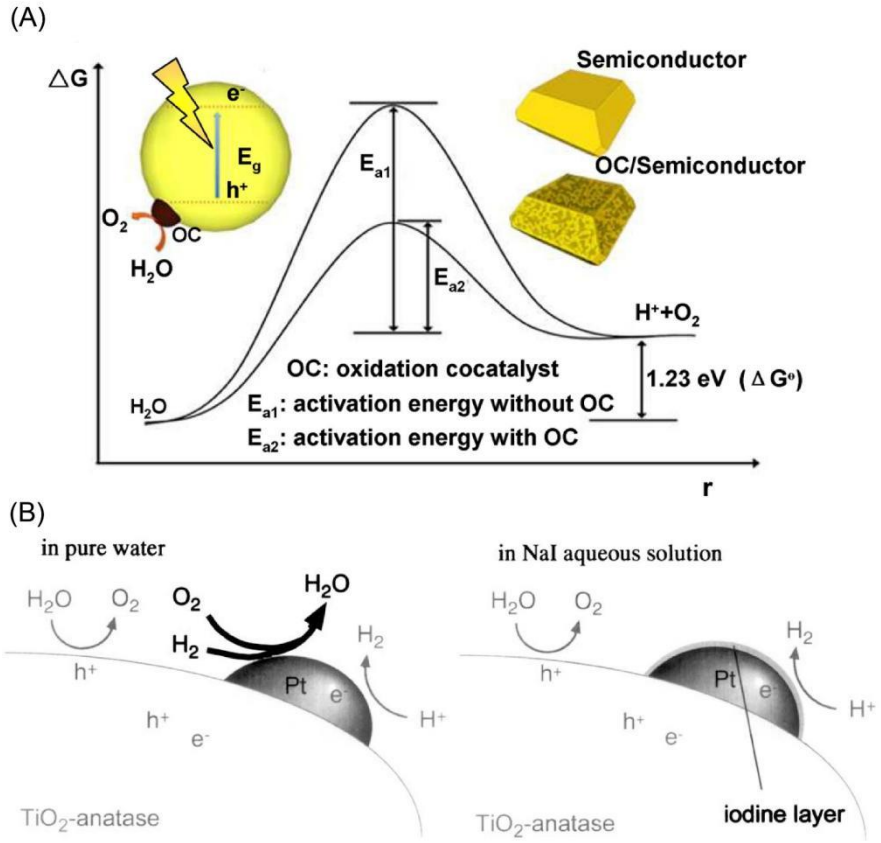

Figure 1.5 Illustration of surface reactions optimization strategies: (A) Effect of oxidation cocatalyst on activation energy;[34] (B) Depress backward reaction by iodine layer.[52]

1.3 Design of HER Photocatalysts

1.3.1 Composition Design of Photocatalyst

The heterojunctions have been used as an efficient method for optimizing light absorption, charges separation and transfer. There are mainly four kinds of heterojunctions, including type-I heterojunctions, type-II heterojunctions, all solid-state Z-scheme, and direct Z-scheme heterojunctions as shown in the figure 1.6.[58]

The band diagram of type-I heterojunction photocatalyst is constructed with a narrow bandgap semiconductor and a wide bandgap semiconductor as shown in figure 1.6A. The electrons transfer from the conduction band (CB) of semiconductor A to the CB of semiconductor B. And the holes transfer from the valence band (VB) of semiconductor A to the valence band of semiconductor B. The electrons and holes are accumulated in CB and VB

of semiconductor B. But the type-II heterojunction photocatalyst as shown in figure 1.6B, shows the CB and VB energy levels of semiconductor A are higher than semiconductor B. Compared with type-I heterojunction photocatalyst, the electrons and holes are accumulated at two semiconductors. The effective separation of electrons and holes into two semiconductors is beneficial to depressing recombination.

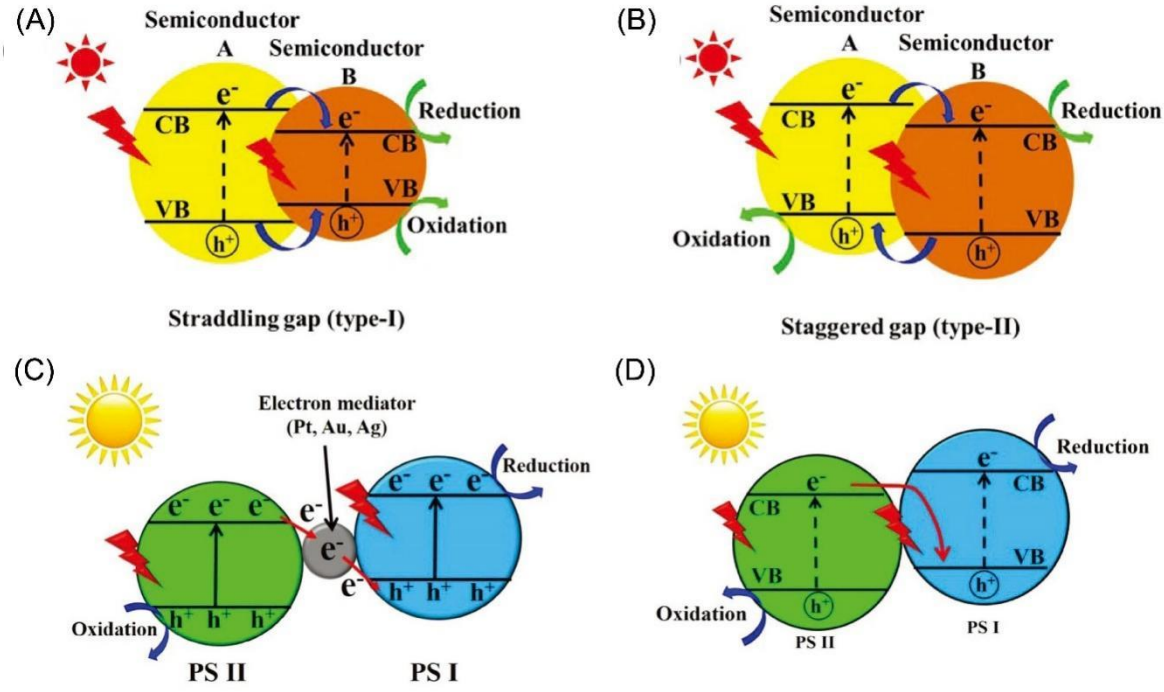

Figure 1.6 Schematic illustration of four heterojunction types of photocatalysts: (A) Type-I heterojunction; (B) Type-II heterojunction; (C) All-solid-state Z-scheme heterojunction; (D) Direct Z-scheme heterojunction.[58]

The Z-scheme heterojunctions are classified into two categories, all-solid-state Z-scheme heterojunction and direct Z-scheme heterojunction as shown in figure 1.6C and figure 1.6D. In the all-solid-state Z-scheme heterojunction, the photogenerated electrons in CB of the photocatalytic semiconductor II (PS II) migrate to VB of the photocatalytic semiconductor I (PS I) through an electron mediator. Then these electrons in VB of PS I are excited to CB of PS I under light illumination. The holes in VB of the PS II participate in the oxidation reaction. the electrons in CB of PS I participate in the reduction reaction. The migration pathway of direct Z-scheme heterojunction is similar to All-solid-state Z-scheme heterojunction. The difference is without an electron mediator in Z-scheme heterojunction. The photogenerated electron in CB of the PS II directly migrates to VB of PS I.

1.3.2 Morphology Design of Photocatalyst

Abundant semiconductor materials with different dimensional have been applied in the photocatalytic fields, such as zero dimension (0 D), one dimension (1 D), two dimensions (2 D), and three dimensions (3 D). The different dimensional materials have different properties in light capture, charges transfer and surface reaction sites. The zero-dimensional (0 D) material such as quantum dot has been summarized in section 1.3.2. And this section summarizes the relationship between the morphology of photocatalysts in 1 to 3 dimensions and photocatalytic performance.

(1) One dimensional Photocatalyst

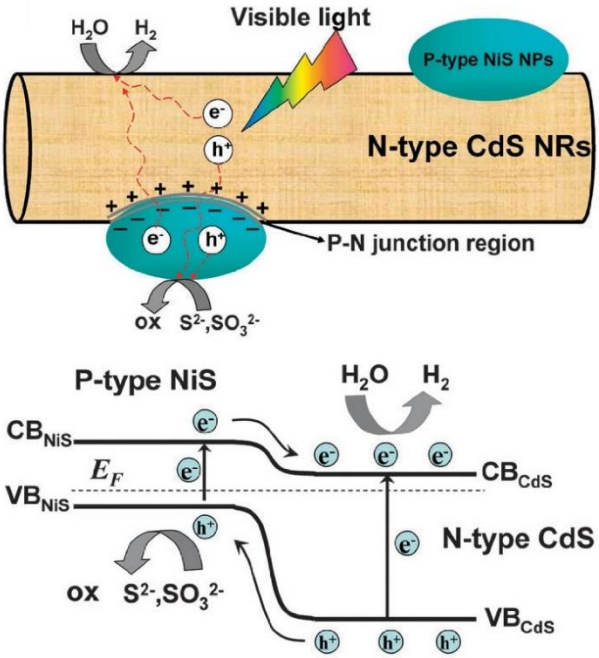

Figure 1.7 Schematic illustration of charges transfer and separation process of 1D p-n junctions.

One dimensional (1D) photocatalysts have been widely researched in photocatalytic HER because of their special physicochemical properties and structures. According to different shapes, the one-dimensional materials are classified as nanobelts, nanowires, nanorods, nanotubes, and corresponding hollow structures.[59] The 1D nanomaterials with a big surface area expose a mass of reaction active centers which can absorb reactants on the surface of photocatalysts. On the other hand, the 1D photocatalyst has a relatively small size compared with another two dimensions. In addition, the channel structures of 1D photocatalysts provide a transfer pathway for charges.[60] Therefore, the reaction active sites and transfer pathway of

1D photocatalysts are contributed to charge separation and surface chemical reaction.

Yu and coworkers have synthesized NiS nanoparticles/CdS nanorod p-n junction photocatalysts by hydrothermal method and applied them in HER.[61] The proposed schematic charges transfer of photocatalyst under visible light and band diagram of p-n junction are shown in figure 1.7.[61] The p-type NiS particles are located on the surface of n-type CdS nanorods and abundant p-n junctions are obtained. The electrons are rich in the CB of CdS nanorods and HER is taken in the CdS nanorods' surface. The electrons in the bulk of CdS nanorods are easily transferred to CdS nanorods' surface because of shorter transfer distance. In the results, the NiS nanoparticles deposited on 1D CdS nanorods present excellent HER performance.

(2) Two dimensional Photocatalyst

The two dimensional (2D) photocatalyst means that the range of charges moves in two dimensions. Compared with 1D photocatalysts, the 2D photocatalysts provide an excellent supporting platform for cocatalysts loading or mixing with other semiconductors.[62] As mentioned in the optimization strategies, the fabrication of heterojunctions is beneficial to light absorption range, charge separation and transfer. The 2D morphology can expose more desired crystalline facets through precise control of synthesis parameters. In addition, the thickness of 2D materials can decrease to nanoscale and even atomic level.[63] The shorter photogenerated charges transfer distance from bulk to surface are greatly reducing the possibilities of charges recombination. The 1D/2D heterojunctions combine the advantages of 1D and 2D, such as fast charges transfer along with 1D structures and accelerating surface reaction by desired crystalline facet.[64]

The ultrathin 2D photocatalysts with the thickness of only a few atoms layers (typically less than 5 nm) are emerging because of high surface activity, electronic anisotropy, tunable energy band structure, and planar conductivity.[65] Yang and coworkers prepare 2D/2D g-C_3N_4@$ZnIn_2S_4$ ultrathin 2D heterojunctions by solvothermal method.[66] The research compares the difference between 2D/0D heterojunction and 2D/2D heterojunction in the same composition. The schematic illustration comparison of contact interfaces for 2D/0D heterojunction and 2D/2D heterojunction is shown in the figure 1.8.[66] 2D/0D sample with point contact results a limited photocatalytic HER performance and slow charges transfer efficiency. 2D/2D sample with face-to-face contact brings abundant charges transfer pathways which promote charges separation and migration and remarkable HER

performance.[67]

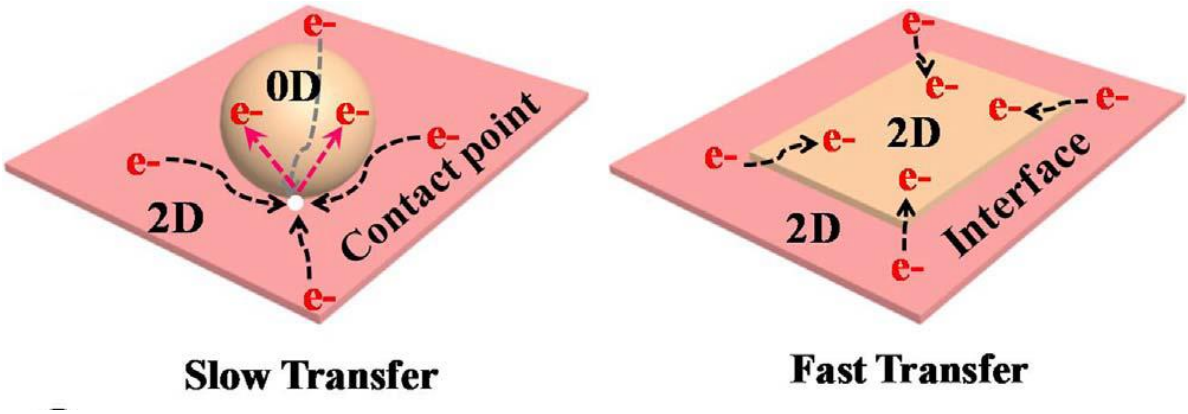

Figure 1.8 Schematic illustration comparison of contact interfaces for 2D/0D heterojunction and 2D/2D heterojunction.[66]

(3) Three dimensional Photocatalyst

The three dimensional (3D) photocatalysts such as solid spheres, cubic, and columnar-like, are investigated in water splitting. Compared with 1D photocatalyst and 2D photocatalyst, the transfer pathway of photogenerated carriers in solid 3D photocatalyst is without limited routes. Hence, 3D hollow framework structures and hollow structures are gradually synthesized with varied methods. Among these hollow structures, hollow multi-shelled structures (HoMSs) with a lot of advantages in the photocatalytic field have been studied extensively. According to reported literature,[68] the HoMSs possesses a big effective surface area and loading ability through a few cavities between different shells. In addition, shell thickness, layer number, and porosity can be accurately adjusted and controlled. Up to now, the HoMSs materials show special advantages, such as light capture ability, charge separation and transfer ability, and accelerating surface chemical reaction through abundant exposed active sites.[68]

i. Enhancing light capture ability

The enhancing light capture ability is contributed by light reflection and light scatting. The shells in HoMSs materials can enhance the light reflection and increase light absorption. The Beer's law can be used to describe the light absorption, as shown in formula 5,[45] in where A presents absorbance, I_0 and I are incident light and transmitted light intensity, respectively. ε as the molar absorption coefficient (usually determined by the nature of the material to A constant), L is the thickness of the sample, and C is the concentration of a sample (for solid materials is a constant). Light absorption can be adjusted to reduce reflection by adjusting the

thickness of the material. In other words, hollow materials with thin shells absorb more light than solid materials as shown in figure 1.9B.[69]

$$A = -\lg\frac{I}{I_0} = \varepsilon LC \quad (5)$$

Scattering enhancement is the increase of optical path through the mutual scattering between shells of hollow structures as shown in figure 1.9A.[69] Different sizes of materials have different Rayleigh scattering effects on light.[70] The Rayleigh scattering ability of micron-scale materials is stronger than that of nanomaterials.[71] Compared with solid materials, hollow structures have a higher light absorption and light scattering ability. $SrTiO_3$-TiO_2 heterogeneous HoMSs synthesized by sequential template method (STA) has been applied in photocatalytic water splitting as shown in figure 1.9D.[72] The HER performance is gradually improved through the increase of shell number. To further understand the light capture ability of multi-shell photoanode microspheres, the time-domain method (FDTD) was used to simulate the theoretical light scattering of a series of hollow multi-shell structures.[73] The simulation and experimental results also prove that the outer double-layer structure of the hollow sphere enhances the light scattering and reflection ability.

ii. Enhancing charges separation and transfer ability

Charge transport in oxide networks is thought to occur through diffusion, charge capture, destrapping within particles, and grain boundaries causing strong limitations on charge transport.[74] As previously stated, non-radiative recombination of charges during transport occurs mainly at grain boundaries, defects, and impurities.[75] Thus, non-radiative processes can occur at grain boundaries and defects existed inside or outside of the materials. Compared with solid material, HoMSs and cavity material reduce the volume defects of the material itself and reduce the probability of electron capture.

Because of the unavoidable charge recombination in the transport processes, the size distribution of materials is an important parameter for realizing better photocatalytic activity. Reducing the size of photocatalysts can narrow electrons transfer distance. But the nanoparticles are easily aggregating into a big cluster. The hollow structure materials with thinner shells reduce the charge migration distance and can significantly depress charge recombination as shown in figure 1.9B.[45] On the other hand, the close-packed subunits between different shells of HoMSs are beneficial for charge transfer resistance. The steady contacts derived from calcination reduce charge transfer resistance which is proved by the

electrochemical impendence spectrum (EIS) of HoMSs materials.[73, 76-79] The resistance decreases as the number of shells increases. It is generally believed that parallel resistance exists in HoMSs between different shells.[80] Therefore, the fast charge transfer within shells improves the possibility of charges transferred into surface reactions, which is impossibly realized by the simple aggregation of nanoparticles.

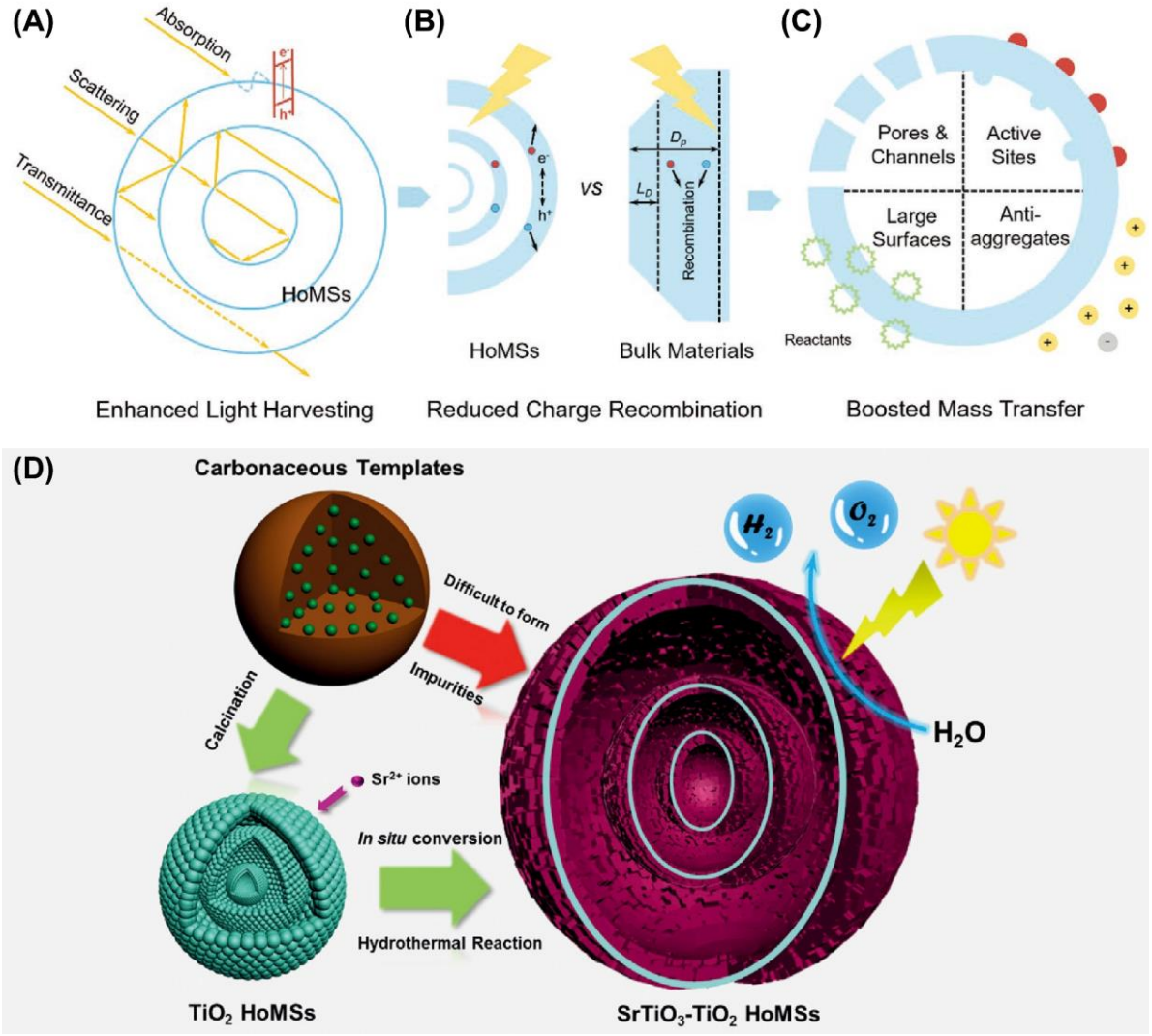

Figure 1.9 Schematic illustration of advantages of HoMSs for photocatalysis: (A) Enhancing light absorption; (B) Charge transfer distance; (C) Surface properties of HoMSs;[69] (D) Synthesis method and application of $SrTiO_3$-TiO_2 HoMSs.[72]

iii. Boosting mass transfer ability

The surface chemical reaction is the main process in photocatalytic HER. The surface chemical reaction process includes three parts. In the first, the reactants are adsorbed by photocatalysts' surface and pores. Next, the reactants after the mass transfer process react

with charges. In the end, the resultant of reaction and charges desorb into the photocatalytic system.[81] The mass transfer process is an important influencing factor for high efficient photocatalyst. The mass transfer process includes exterior mass transfer and interior mass transfer. But the exterior mass transfer can be negligible in a mixing uniformity photocatalytic system whether the catalyst is solid nanoparticles or hollow spheres.[82] The total mass transfer rate is sometimes decided by interior mass transfer resistance. The interior mass transfer process depends on what kind of catalyst. The HoMSs material with controllable shell space, pore size, and porosity is a wonderful candidate for photocatalysts. For mass transfer, there are two advantages of HoMSs materials as shown in the figure 1.9C.[69] A larger surface area of the HoMSs contributes to improving the absorption process of reactants; The pore size and porosity of shells are beneficial to mass transfer across the shells.[83]

1.4 Synthesis of Hollow Multi-shelled Structures (HoMSs)

The HoMSs material has been widely applied in solar cells, catalysts, drug delivery, lithium-ion batteries (LIBs), and supercapacitors because of a lot of advantages, such as a high surface-to-volume ratio, internal cavities with high loading capacity, low volume density, lower electrons transfer resistance, shorter transfer distance.[84-85] The state-of-the-art synthesis methods mainly include hard template method,[86] soft template method, self-template method, and sequential templating approach.

1.4.1 Hard Template Method

HoMSs materials synthesized by hard template method are obtained after taking complex multi-step experiments. This method can be applied to synthesize many kinds of materials such as metallic oxide and nonmetallic oxide. The multi-step experiments mainly include coating steps and removing template steps.[86] As shown in figure 1.10, TiO_2 HoMSs was synthesized by shell-by-shell method.[87] In the first, the silica/titania core/shell nanoparticles (ST CS NPs) are synthesized by the sol-gel reaction. The ST CS NPs modified by polyvinylpyrrolidone (PVP) is chosen as a seed and coated with silicon dioxide (SiO_2) by the Stober method (tetraethyl orthosilicate (TEOS) as silicon source). The second layer of TiO_2 was synthesized by sol-gel reaction by adding titanium isopropoxide (TTIP). Before removing the template, the composite was calcined at a high temperature to increase crystalline. To obtain hollow multi-shelled spheres, the SiO_2 template was removed by etching at NaOH solution. According to different templates used, the template removing methods include etching at specific chemicals (acid solution, alkali solution, salt solution,

organic solvent) and calcining strategy.[87]

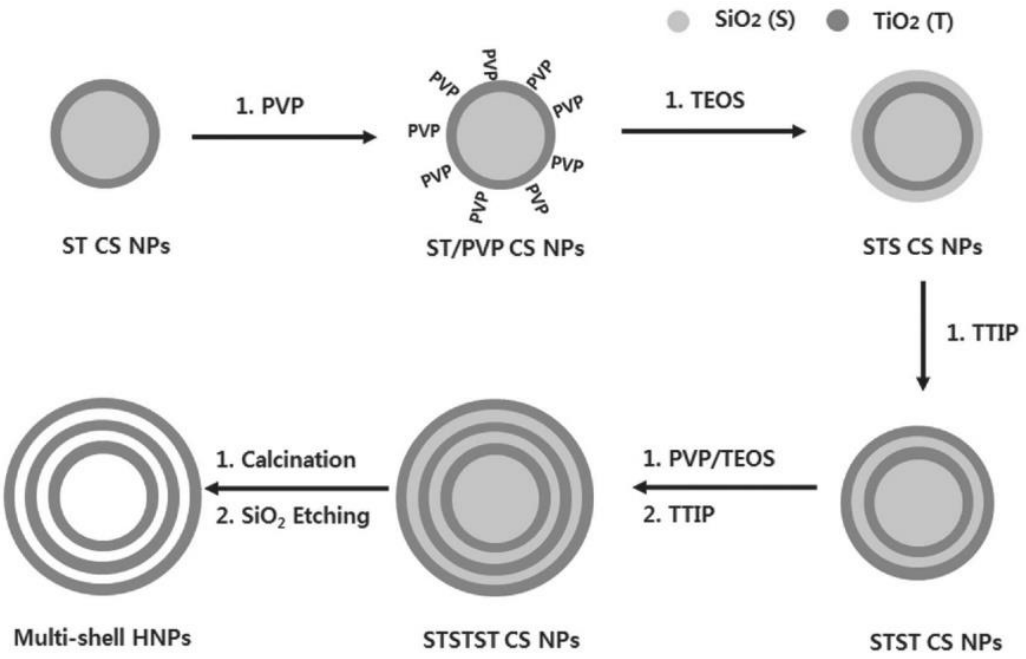

Figure 1.10 Schematic illustration of TiO_2 HoMSs synthesized by shell-by-shell method.[87]

1.4.2 Soft Template Method

The multi-shelled structures synthesized by soft template method are controlled by the surface tension of interfaces in the different systems, such as water and oil emulsion, micelle/vesicle, and gas bubble.[88] Compared with shell-by-shell method, the synthesis process of the soft template method is simple. But the categories of HoMSs materials synthesized by soft template method are less reported. For example, Wang and coworkers reported the first successful synthesis strategy of Cu_2O HoMSs in 2007 as shown in figure 1.11.[89] The bilayers of a vesicle have obvious interfaces and exist as a circle. There are many Br^- suspending bonds in two sides of the bilayers vesicle originating from cetyltrimethylammonium bromide (CTAB). The suspending bonds act as deposition sites for copper ions (Cu^{2+}) through electrostatic interaction. The Cu^{2+} and Br^- suspending bond form the Cu−Br bond closing with hydrophilic groups of CTAB. The concentration of Cu^{2+} in bilayers of vesicle is gradually increasing and turning into cuprous oxide (Cu_2O). After Ostwald ripening process, the hollow spheres are obtained. By turning the concentration of CTAB to control the numbers of the vesicle, the multi-shelled Cu_2O can be synthesized. Except for the concentration of surfactant, the number of vesicles is affected by reaction conditions, including solvent, temperature, pH value, and additive agents.[81] Although the soft template method can synthesize HoMSs in one step, the experiment process requires precise control.

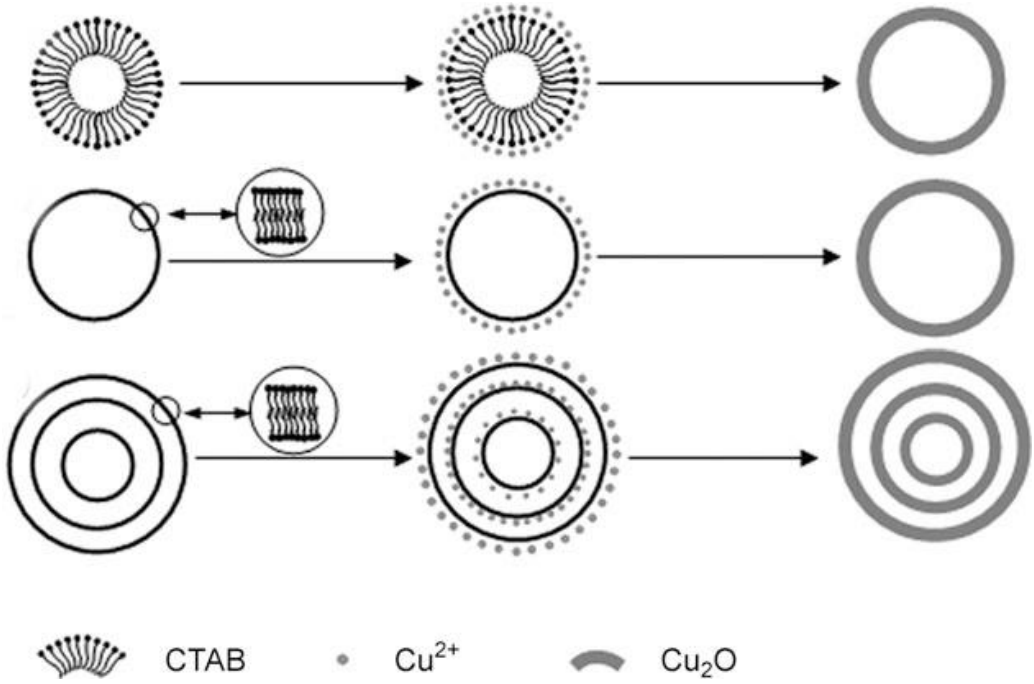

Figure 1.11 The Schematic illustration of Cu_2O HoMSs synthesized by soft template with the multi-lamellar vesicle.[89]

1.4.3 Self-template Method

No external templates are required when using the self-template method to synthesize HoMSs. Hence, the self-template method is also named as template-free method. The mechanism of self-template method primarily includes Kirkendall effect,[90] Ostwald ripening effect[91], and ion exchange effect.[92]

The ion exchange effect has been applied as an efficient self-templating strategy to synthesize HoMSs. The ion exchange method can control the morphology, porous sizes, and adjustable elemental composition of the HoMSs.[92] The ion exchange effect is driven by the electrochemical potential difference value between two kinds of metals.[81] The electrochemical potential brings redox reactions in thermodynamics. Hence, one metal is a reducing agent and another metal is an oxidizing agent. The Ostwald ripening is defined as a dissolved process and redeposited process. The small crystals such as small particles are dissolved first and then the dissolved materials are redeposited on larger crystals or particles.[81] The small crystals turn into spherical larger crystals because the spherical crystals have minimizing interfacial energy.[88] The inside small crystals are generated in the first and then the larger crystal is formed on the outside with lower surfaces energies. To reduce the total surface energy, the inside small crystals begin to dissolve and redeposit into larger crystals size. That is the main reason for hollow structures forming. The Kirkendall effect is applied

to the synthesis of HoMSs because of the different diffusion rates of different elemental ions.[81] Recently, the combination of ion exchange effect and Kirkendall effect are used to synthesize AuAg HoMSs.[92] These novel strategies for the formation of shell and hollow structures are supposed to synthesize more complex HoMSs.

1.4.4 Sequential Templating Approach (STA)

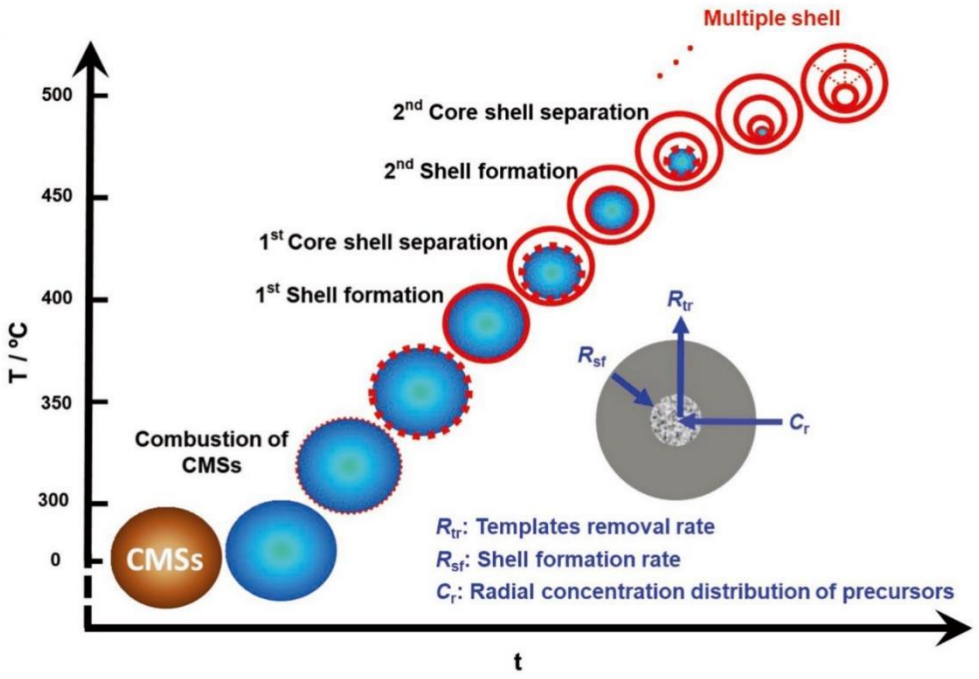

Figure 1.12 The schematic illustration of HoMSs synthesized by STA.[68]

The STA was promoted by professor Dan WANG's group in 2009 and the STA was defined as using a template for rich metal or nonmetal precursors followed by sequential templating multiple times in a one-step annealing process [93] The synthesis of HoMSs by STA requires two prerequisites as shown in the figure 1.12.[68] The first one is the deep penetration depth of precursors located inside of the templates. The corresponding radial concentration distribution of precursors is named Cr. The second prerequisite is that the template removing rate (Rtr) suits the shell forming rate (Rsf). If Rsf is much less than Rtr, the results will obtain dispersed nanoparticles. In contrast, if Rsf is much larger than Rtr, porous microspheres will obtain. During the past decade, STA has achieved tremendous advances in both HoMSs synthesis and application. Turning precursor concentration,[76, 93] heating rate,[79] adsorption duration and temperature,[77, 94] hydrothermal adsorption[95], and pretreatment of carbonaceous spheres[96] can affect the morphology of HoMSs.

1.5 Motivation and Significance of the Topic

Water splitting by solar energy is a green technology. The design of photocatalysts is important for water splitting performance. HoMSs materials have been widely studied in recent years because of a lot of advantages in solar energy conversion. The HoMSs materials such as $SrTiO_3$-TiO_2 HoMSs,[72] TiO_2-Cu_xO HoMSs,[97] $SrTiO_3$ HoMSs [35] have been applied in the photocatalytic field and present wonderful performance. Hence, the further design of HoMSs photocatalysts is essential.

In the synthesis of HoMSs part, the synthesis strategies of HoMSs materials by sequential templating approach (STA) have been summarized.[85] Turning precursor concentration,[76, 93] heating rate,[79] adsorption duration and temperature,[77, 94] hydrothermal adsorption[95] and pretreatment of carbonaceous spheres[96] can affect the morphology of HoMSs. The carbonaceous spheres (CMSs) are chosen as a template to adsorb precursor solution in STA. Adsorbing depth inside carbonaceous spheres is important for the formation of HoMSs. The adsorbed carbonaceous spheres are calcined in the muffle furnace with a fixed heating rate and keep for a few hours at a constant temperature. The HoMSs is gradually formed as the temperature increasing and the burning of the carbonaceous template. The precursor adsorbed in carbonaceous spheres is turning into oxide in the air atmosphere. If there is no more precursor in the deep inside the carbon sphere, the HoMSs with three shells or more is difficult to obtain. Based on the above thought, increasing adsorption depth inside of carbonaceous spheres is beneficial to get HoMSs with three shells or more.

The halide inorganic-organic perovskite (named hybrid perovskite) materials attract more attention because of the adjustable band gap and longer carrier diffusion length.[98] As we all know, hybrid perovskite materials cannot be stable in a moisture environment. But in 2007, Ki Tae Nam and coworkers propose a strategy for stable methylammonium lead iodide in hydroiodic acid solution.[99] After this report, many studies about hybrid perovskite materials applied in photocatalytic HER have been gradually published. The hybrid perovskite is usually applied in solar cells field or light-emitting diode field. The electrons transfer layer always chooses titanium oxide (TiO_2) as the extraction material of electrons. Combining $MAPbI_3$ and TiO_2 can construct a heterojunction which helps charges separation and transfer. At the same time, the empty cavities HoMSs materials contribute to loading more dye molecules and then producing a better light absorption.[73] According to the merits of HoMSs in photocatalytic, loading hybrid perovskite material into cavities of HoMSs materials promises to be a better photocatalyst.

The electrons transfer pathway in heterojunction includes the bulk of hybrid perovskite,

heterojunction interface, and the bulk of TiO_2 HoMSs. The TiO_2 materials have three phases, including anatase, rutile, and brookite. Among these phases, anatase or rutile, or both are commonly used as a photocatalyst in photocatalytic hydrogen evolution. Anatase and rutile have different properties. The electron mobility of anatase and rutile are 10 $cm^2/(V \cdot s)$ and 1 $cm^2/(V \cdot s)$, respectively.[100] In addition, rutile phase TiO_2 and perovskite have better lattice matches which help faster electrons transfer.[101] To study the effects of the electrons transfer pathway on performance, such as TiO_2 HoMSs bulk and heterojunctions interfaces, the different ratio of anatase to rutile is taken. If the anatase ratio is larger than rutile, the electrons transfer in TiO_2 HoMSs bulk is fast. If the rutile ration is larger than anatase, the electrons transfer in heterojunctions interface is fast.

1.6 Research Goals and Strategies

Regarding the synthesis of HoMSs, increasing adsorption depth inside of CMSs is an effective way to get more shells. There are two strategies for increasing adsorption depth. The first one is choosing a smaller ions radius which can diffuse with less resistance. But HoMSs material category is designed as TiO_2 and the Ti^{4+} in TiO_2 precursor solution (titanium tetrachloride aqueous solution) has a fixed radius. The second strategy is enlarging the pores of CMSs. The CMSs are synthesized by hydrothermal method with sucrose as a carbon source. The hydrothermal reaction processes include fragmentation, ring-opening, dehydration, polymerization, and carbonization. In the polymerization and carbonization process, the reactants such as organic acids, polyhydric alcohols, unreacted sucrose, and aldehydes are easily attached to the molecular chain or surfaces of CMSs. The most above reactants are soluble in ethanol. Hence, pretreatment of CMSs with ethanol may enlarge possibly the size of pores and remove surface reactants.

Loading the $MAPbI_3$ materials inside TiO_2 HoMSs constructs a heterojunction to enhance visible-light absorption and improve charges separation. According to reported literatures, there are two strategies for loading perovskite. The first one is loading the lead source firstly. And then synthesis of $MAPbI_3$ by chemical vapor deposition (CVD) at 200 °C in the iodine methylamine atmosphere. The second one is loading $MAPbI_3$ precursor solution and then removing solvents in the solution. Comparing the two strategies, the second strategy is simple and saves chemicals. The $MAPbI_3$ can be dissolved in dimethyl sulfoxide (DMSO) or N, N-dimethyl formamide (DMF). Hence, the $MAPbI_3/TiO_2$ HoMSs is synthesized by the impregnation method through dispersing TiO_2-HoMSs in the $MAPbI_3$ precursor. By adjusting the concentration of $MAPbI_3$ precursor, the different ratios of $MAPbI_3$ in the composite can

be controlled.

The HER performance can be measured at a top-irradiation vessel reaction system. To realize the stability of $MAPbI_3$, a strategy of a saturated solution of $MAPbI_3$ in the mixing of Hydroiodic acid and hypophosphoric acid is chosen. To accelerate charges separation, the noble metal platinum (Pt) can be deposited by photoreduction of chloroplatinic acid. The effects of the morphology of HoMSs on performance can be compared by synthesizing $MAPbI_3$/Pt/TiO_2- HoMSs with different shells.

To study the effects of different phase of TiO_2 HoMSs on performance, regulation of the ratio between anatase and rutile is necessary. The anatase can convert into rutile at high temperatures.[102-103] But the rutile cannot convert into anatase because the rutile phase is more stable than anatase. Hence, the control of TiO_2 HoMSs with the different ratios is realized by adjusting calcination temperature. The proportion of rutile in the mixing phase is increasing as the calcination temperature increases in theoretical rules.

1.7 Thesis Outline

Chapter 1 introduces studies of photocatalytic water splitting over the past few decades. The principle of photocatalytic water splitting is explained briefly in the first. The main processes of photocatalytic HER and corresponding optimization strategies, such as light absorption optimization strategies, charges separation and transfer optimization strategies, and surface reactions optimization strategies, are surveyed. The heterojunction categories and design principles of photocatalysts are also classified and introduced. In addition, the advantages of different dimensional photocatalysts applied in photocatalytic water splitting are summarized, including 1D photocatalysts, 2D photocatalysts, and 3D photocatalysts. And the effect of morphology of photocatalysts on HER performance is also explained. In particular, the merits of 3D HoMSs, such as enhancing light capture ability, enhancing charges separation and transfer ability, and boosting mass transfer ability, are illustrated in detail. According to the above analysis, the motivation, research goals, and strategies are promoted in the end.

Chapter 2 focuses on the synthesis and control of TiO_2 hollow multi-shelled structures (HoMSs) and $MAPbI_3$/Pt/TiO_2-HoMSs. The CMSs pretreated with ethanol with different washing time was chosen as a template to adsorb titanium precursor solution. The TEM results indicate that the pretreated CMSs as the template can obtain more shells of TiO_2 HoMSs when extending pretreatment time. The SEM images indicate the size of the pores was gradually increased when extending pretreatment time. In addition, the FT-IR results

show functional groups of CMSs remain unchanged when extending pretreatment time. The experiments on the duration time of adsorption and heating rate are carried out in this chapter. In the end, obtained TiO_2 HoMSs samples are characterized by XRD, SEM, TEM, Raman, SAED, HRTEM, and XPS. The results show that TiO_2 HoMSs is the mixed-phase with good crystallinity. On the other hand, the synthesis of $MAPbI_3$/Pt/TiO_2-HoMSs materials by immersion method. The samples characterized by XRD, TEM, elemental mappings, and line scan proves that $MAPbI_3$/Pt/TiO_2 HoMSs has been successfully synthesized.

Chapter 3 focuses on the application of $MAPbI_3$/Pt/TiO_2-HoMSs materials in photocatalytic HER. The photocatalytic performance was measured under visible-light. The PL and PL decay results indicate that the heterogenous interface of $MAPbI_3$/TiO_2-HoMSs can efficiently promote the separation of photogenerated carriers. Additionally, HoMSs assembled with multiple shells can support abundant available surfaces for building heterogeneous interfaces and photocatalytic reactions. The interfacial photogenerated charge separation and transport have demonstrated great influence on photocatalytic performance.

Chapter 4 focuses on the effects of different phases of TiO_2 HoMSs on photocatalytic performance. The different phase ratios between anatase and rutile were synthesized at different calcined temperatures. The photocatalytic results show the different properties. The corresponding electron separation and transfer behavior was characterized by transient photocurrent response. Additionally, the electron transfer resistance and conduction band potential were confirmed. Compared with rutile, The $MAPbI_3$/Pt/ anatase TiO_2 HoMSs display better photocatalytic performance.

Chapter 5 summarizes the main conclusions of chapters 2-4. This chapter reviews a few innovations for the synthesis of TiO_2-HoMSs, heterogeneous interfaces of $MAPbI_3$/TiO_2-HoMSs. In addition, more perspective opinions based on current research are promoted. The construction of heterojunctions is an efficient method to enhance light adsorption and charges separation. But the perovskite in this research system is limited to the photocatalytic hydroiodic acid saturated solution splitting system. Hence, the stabilization strategies of hybrid perovskite or all-inorganic perovskite in water need further study. The new photocatalysts with reasonable conduction band and bandgap are needed to find. The heterogeneous in one shell mixed with two kinds of materials.

CHAPTER 2.

Synthesis and Control of TiO_2 Hollow Multi-Shelled Structures and $MAPbI_3/Pt/TiO_2$ HoMSs Composites

2.1 Abstract

In the past decade, abundant researches have been reported about the hollow nanostructures with different compositions and geometric characteristics. The synthesis of hollow structures by sequential templating approach (STA) is universal and widely applicable, especially in hollow multi-shelled structures (HoMSs). The pretreatment of carbonaceous microspheres used in STA is a very important step in the synthesis process. However, how affect the pretreatment process on the surface state has not been reported. In this chapter, the pretreatment of carbonaceous microspheres by ethanol was studied. With the prolongation of pretreatment time, the pores size of the carbon sphere was increased. Turning the adsorption duration time, pretreatment duration time, and heating rate can control the shells' number of TiO_2. And the morphology and phase of obtained TiO_2 HoMSs samples were characterized by XRD, Raman, XPS, TEM, and SEM. Besides, the composite photocatalysts of methylammonium lead iodide perovskite ($MAPbI_3$) inside TiO_2 HoMSs are constructed by the impregnation method. A few characterizations, such as XRD, TEM line scan, TEM mapping, and FTIR, confirm that the $MAPbI_3$ was introduced inside TiO_2 HoMSs successfully.

2.2 Introduction

Over the past decades, hollow structures have been studied extensively in broad fields, such as catalysts, solar energy conversion, drug release, rechargeable batteries, supercapacitors, sensors, and absorption of electromagnetic waves. Up to now, hollow structures usually can be obtained by hard template method, soft template method, and self-template method. The hard templates mainly include polymer-based templates (polystyrene templates,[104] poly(methylmethacrylate),[105] formaldehyde resin templates;[106]), silica-based templates (solid silica templates,[107] silica shell as templates,[108] mesoporous silica templates;[109]), carbon-based

templates (mesoporous carbon templates,[110] solid carbon templates;[111]), metal-based and metal oxide-based templates (nickel,[112] gold,[113] metal oxide;[114]), templates based on salts ($CaCO_3$ nanoparticles as templates[115]), natural materials (natural cellulose fibers[116]). The soft templates mainly include emulsion-based soft templates (direct emulsion templates,[117] reverse emulsion templates,[118] double emulsion templates;[119]), micelle/vesicle-based soft templates,[120] gas bubble-based soft templates,[121] electrospray method.[122] The mechanisms of the self-template method contain Ostwald ripening effect,[91] selective etching[123], Kirkendall effect,[90] and ion exchange effect.[92]

Recently, compared with simple hollow structures, the hollow multi-shelled structures have been proved to be a kind of wonderful functional material with shorter lengths of mass and charge transport, enhanced light capture, and effective charge separation. The mentioned above synthesis methods are always used for simple hollow structures instead of hollow multi-shelled structures. Though these methods can prepare hollow multi-shelled structure, synthetic processes need multi-step complex reaction processes and accurate control. The sequential templating approach (STA) method provides a simple synthetic route to get multi-shelled structures. The desired metal source was adsorbed by carbonaceous microsphere followed by calcined at muffle furnace. After a one-step calcination process, the HoMSs can be obtained. According to the reported literature, the control of morphology can be realized by regulating experimental parameters. The shells of Fe_3O_4 HoMSs and $ZnFe_2O_4$ HoMSs can be adjusted by the precursor concentration of metal ions.[76, 93] The ZnO HoMSs was accurately controlled by changing the heating rate.[79] In addition, using alkali treated CMSs as a template, the unique tin dioxide multi-shell microspheres with higher light trapping ability were successfully prepared.[73] Except for alkali-treated carbonaceous microspheres, manganese oxide hollow microspheres also have been studied with different pH values.[124]

The adsorption amount of metal ions by carbonaceous microspheres determines whether there are enough metal ions to form multiple shells. At the same time, increasing the precursor salt concentration may cause more metal ions to penetrate inside the template and generate more shells after heat treatment. Hence, the microstructure of HoMSs (including interlayer spacing, the thickness of shells, and shell number) can be regulated by adjusting the adsorption amount and embedding depth of metal ions inside of carbonaceous microsphere template and changing the annealing conditions.[85]

Motivated by the effects of adsorption capacity and embedding depth on morphology, the pretreatment manner is really important for the synthesis of HoMSs. Increasing the porosity

of the carbonaceous microsphere (CMSs) can reduce the obstruction of metal ions entering the inside. Metal ions entering the interior of CMSs ensures adsorption capacity and embedding depth. The carbonaceous microsphere used in STA is always obtained from the hydrothermal method with sucrose as a carbon source. In the hydrothermal synthesis process, there is a carbonization step, in which cross-linking process between intermolecular dehydration of linear or branched oligosaccharides or other macromolecules formed in the polymerization step will happen. Meanwhile, some accessory substances in the reaction (such as polyhydric alcohols, furfural compounds, and weak organic acids) also possibly crosslink with the multipolymer.[125] The polyhydric alcohols, furfural compounds, and weak organic acids are usually easily dissolved in ethanol.

The $MAPbI_3$ halide perovskite is soluble in the mixed solvent of DMF-DMSO. At the same time, TiO_2 HoMSs is wettable in the mixed solvent because DMF is an amphipathicity solvent. And Abundant pores in HoMSs provide many pathways for introducing $MAPbI_3$ precursor inside HoMSs. By removing the organic mixed solvent, the $MAPbI_3$ halide perovskite can be introduced inside TiO_2 HoMSs.

In this chapter, the pretreatment of the carbonaceous microsphere by ethanol was carried out. The conditions of the preparation of TiO_2 HoMSs with single, double, and triple shells were obtained through the regulation of adsorption time, carbon sphere pretreatment, and temperature rise rate. The longer adsorption time and pretreatment of carbonaceous microspheres contribute to the adsorption of more Ti precursors by the CMSs template. The TiO_2 HoMSs materials obtained in this chapter are mixed phases of anatase and rutile. And the TiO_2 HoMSs is polycrystalline materials with good crystallinity. Besides, the $MAPbI_3$/Pt/TiO_2 HoMSs have been synthesized and confirmed by XRD and TEM.

2.3 Experiment Section

2.3.1 Chemicals

Titanium tetrachloride ($TiCl_4$), hypophosphite acid (H_3PO_2, 50 wt.% in H_2O), hydroiodic acid (HI, 55 wt.%), and methanol anhydrous were purchased from Sinopharm Chemical Reagent Co., Ltd with analytically grade. Sucrose ($C_{12}H_{22}O_{11}$) was purchased from Beijing Chemical Co., Ltd with analytical grade. Ethanol (Purity, 99%) was purchased from Beijing Tongguang Fine Chemicals Co., Ltd. The deionized water (DI water18.25 MΩ·cm) was made by the Aike lab pure water system. All reagents were directly used without further purification. Dimethyl formamide (DMF) and dimethyl sulfoxide (DMSO) were bought from Sigma-Aldrich.

Methylamine iodide (MAI) (99.99%) and lead iodide (PbI_2) (99.99%) were bought from Xi'an Polymer Light Technology Corp. All reagents were used without further purification.

2.3.2 Experimental Equipment

Precision electronic balance (Beijing Dolly instrument system Co., Ltd. Model: BS224S), magnetic stirring apparatus (Jiangsu Changzhou guohua electronics Co., Ltd. Model: HJ-4A), drying oven (Tianjin Taisite instrument Co., Ltd. Model: 202-1), ultrasonic cleaner (Kunshan ultrasonic instrument Co., Ltd. Model: K-Q250B), Teflon steel reactor (500 mL), refrigerator (Siemens. Model: KG32NV21EC), Aike lab pure water system (Model: AKSW-V-16), vacuum oven (Shanghai yiheng technology co., Ltd. Model: DZF-6020).

2.3.3 Methods

2.3.3.1 Synthesis of Carbonaceous Microspheres (CMSs)

The CMSs were synthesized by the hydrothermal method in an emulsion polymerization reaction of sucrose.[77] Typically, 250 mL of DI water was added firstly into a 500 mL Teflon reactor followed by adding the 130 g sucrose gradually with magnetic stirring. After stirring for 20 minutes to obtain the complete dissolution of a transparent aqueous solution, the Teflon reactor was placed into a steel autoclave. The hydrothermal reaction was kept at 200 °C for 138-142 minutes and then cooled down to room temperature at a slow rate. The brown suspension solution was filtered by a Buchner funnel and then washed three times with deionized water. The obtained brown sample was put in a drying oven and dried at 60 °C for 12 hours. It is worth noting that the reaction time of hydrothermal varies with room temperature. Prolonged reaction time is required at low room temperature.

2.3.3.2 Pretreatment of Carbonaceous Microspheres by Ethanol

The as-prepared carbonaceous microspheres were ground by agate mortar. 2 g CMSs were dispersed at 100 mL ethanol in the beaker with magnetic stirring and ultrasonic dispersion. The whole pretreatment process sustains for 4-18 hours at room temperature. finally, the suspension was filtered by a Buchner funnel and washed with DI water three times, and then dried at 60 °C for 12 hours.

2.3.3.3 Preparation of Titanium Tetrachloride ($TiCl_4$) Aqueous Solution

The chemical of titanium tetrachloride ($TiCl_4$) is the source of titanium. As we all know, titanium tetrachloride is rapidly hydrolyzed through an intense exothermic reaction to

produce a lot of heat and hydrolysates (such as HCl, $Ti(OH)_X$, titanium oxychloride, and titanium dioxide) when contacting with water molecules. For the preparation of $TiCl_4$ aqueous solution, ice was prepared firstly by refrigerator with 300 mL deionized water. 168 mL of titanium tetrachloride ($TiCl_4$) was gradually added into the ice container with continuous shaking. When the adding process was completed and the solution decreased to room temperature, the $TiCl_4$ aqueous solution was shifted to a 500 mL volumetric flask. After volume fixing at 500 mL, 3 mol L^{-1} of $TiCl_4$ aqueous solution was obtained. The $TiCl_4$ aqueous was directly used in the following experiments without dilution.

2.3.3.4 Preparation of Titanium Dioxide (TiO_2) HoMSs

The as-prepared CMSs or pretreated CMSs were firstly ground by agate mortar. Then, the 1.2 g CMSs or pretreated CMSs were well dispersed in 60 mL of the above-prepared $TiCl_4$ aqueous solution and then ultrasonication dispersion for 10 min. The above mixed solution was under stirring for 1-24 hours at the room temperature or 40 °C water bath followed by filtration, washed twice with deionized water, and dried at 60 °C for 6 hours. The black sample obtained after the drying process was placed into a muffle furnace with a heating rate of 5-9 °C min^{-1} and held for 2 hours. When the muffle furnace temperature decreased down to room temperature, white power was obtained.

2.3.3.5 Synthesis of $MAPbI_3$.

The $MAPbI_3$ material was synthesized by simply removing the organic solvent from the precursor solution. In the first, 50 μL 1.2 mol/L perovskite precursor organic solution was dropped into a 10 mL bottle. The 20 μL mixed solvent (DMF and DMSO by volume as 4:1) was placed around the above perovskite precursor solution. Next, the bottle was put in the vacuum oven. In the end, the vacuum oven was kept at 70 °C and held for 5 h. The black product of $MAPbI_3$ was collected.

2.3.3.6 Synthesis of Pt/TiO_2 HoMSs.

The photo-reduction method was chosen to load cocatalyst Pt on TiO_2 HoMSs from reported literature.[126] Detailly, a mixed solution of 15 mL deionized water and 4 mL methanol anhydrous was prepared in the first. Then, 50 mg TiO_2 HoMSs and 75 μL of $H_2PtCl_6 \cdot 6H_2O$ solution (40 mg/mL) were well dispersed in the above mixed solution, followed by ultrasonic dispersion. The obtained suspension liquid was irradiated by a 300 W Xe lamp (Ushio-CERMAXLX 300). After irradiation for 3 hours, the gray products of Pt/TiO_2 HoMSs were centrifuged, washed with deionized water, and finally dried at 50 °C for 6 h in a vacuum oven.

2.3.3.7 Synthesis of $MAPbI_3/Pt/TiO_2$ HoMSs.

The composite was synthesized by the impregnation method. First, 35 mg of Pt/TiO_2 HoMSs were placed in a bottle, and then the gases in the inside TiO_2 HoMSs were drawn out in a vacuum system. Then, 50 μL 0.6 ~1.5 mol/L $MAPbI_3$ precursor solution was dropped rapidly, and the bottle was kept quiescence at room temperature for 24 h. Next, the 20 μL mixed solvent of DMF and DMSO (4:1 by volume) was placed around the above mixture. Finally, the bottle was kept att 70 °C and held for 5 hours.

2.3.4 Characterizations

The composition of materials was characterized by powder X-ray diffraction (XRD), Raman spectra, X-ray Photoelectron Spectroscopy (XPS), and Fourier transform infrared spectrums (FT-IR). XRD patterns were recorded on a Panalytical X'Pert PRO MPD [Cu Ka radiation (λ, 1.5406 Å)], operating voltage at 40 kV, and current at 30 mA. The Raman spectra were performed by an HR-550 (Jobin Yvon). XPS spectrums were measured by ESCALab220i-XL electron spectrometer with VG Scientific using Al Kα radiation (300 W). The binding energy of XPS was amended with reference C 1s (284.8 eV) before analysis. The Fourier transform infrared spectrometer (FT-IR) was carried out by the Varian company (Excalibur 3100). The morphology of materials was characterized by scanning electron microscopy (SEM) and transmission electron microscopy (TEM). SEM images were taken using a JSM-6700 microscope operating at 5.0 kV. TEM, selected area electron diffraction (SAED), high-resolution TEM (HRTEM) images were obtained on a JEOL F2000 instrument using an accelerating voltage of 200 kV. The mass fraction of perovskite was analyzed and calculated from an inductively coupled plasma (ICP) emission spectrometer (Shimadzu, ICPE-9000) test.

2.4 Results and Discussions

2.4.1 Synthesis and Characterizations of TiO_2 HoMSs

2.4.1.1 Different Adsorption Duration Time

The sequential templating approach (STA) method was introduced to the controllable synthesis of hollow multi-shelled structures (HoMSs) in 2009.[93] Conventionally, the STA method adopts CMSs as a template. The CMSs were synthesized by emulsion polymerization reaction[127-128] under hydrothermal conditions with sucrose as a precursor. From the SEM images as shown in figure 2.1, it can be observed that the carbonaceous microspheres are well

dispersed. Through statistical particle size analysis, the range of size distribution is from 1.5 μm to 3.5 μm and the average size of the carbonaceous microspheres is 2.72 μm.

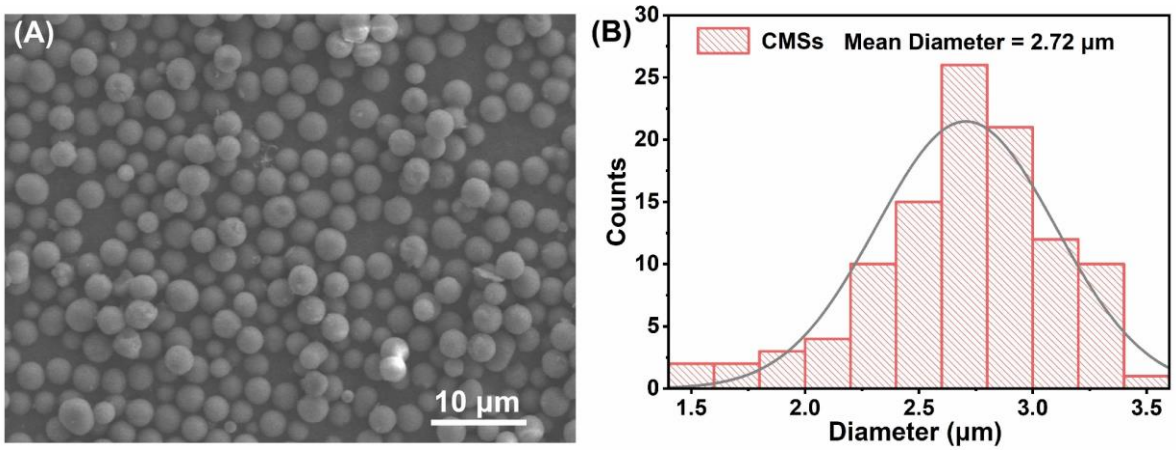

Figure 2.1 (A) SEM images of CMSs synthesized by hydrothermal method; (B) Corresponding statistics of diameter of CMSs.

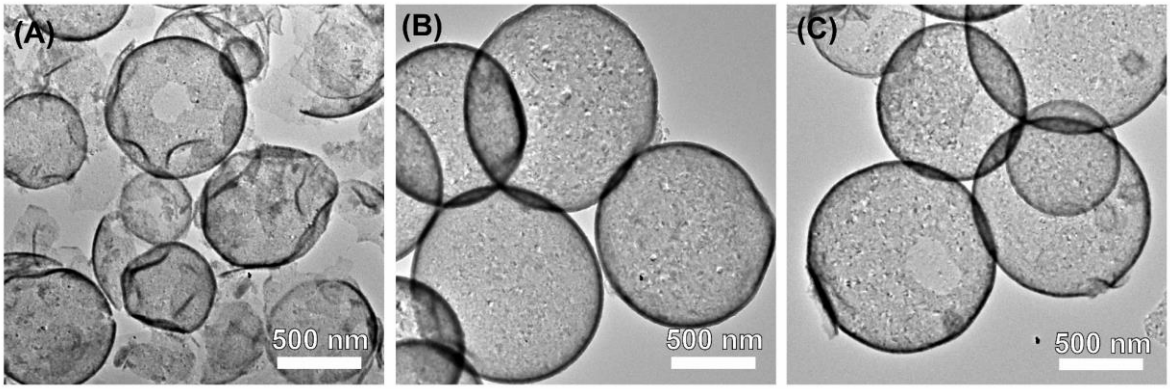

Figure 2.2 TEM images of TiO_2 samples with different adsorption duration times: (A) 3 hours at room temperature; (B) 6 hours at room temperature; (C) 18 hours at room temperature. The heating rate is 5 °C min^{-1}.

To synthesize TiO_2 HoMSs, the above-prepared carbonaceous microspheres (CMSs) were chosen as templates. HoMSs were prepared by STA with different adsorption times and the TEM images were shown in Figure 2.2. When the adsorption time at 3 hours, the sample is a single shell layer, but more fragments of the shells existed around the hollow sphere. And the spherical shape is not regular as shown in figure 2.2A. In figure 2.2B, with the prolongation of the adsorption time to 6 hours, it is noticed that the sample obtained is a hollow monolayer structure with a regular spherical shape. When the adsorption time is further extended to 18 h, a bilayer shape is formed as shown in figure 2.2C. However, the second shell layer in HoMSs is smaller. According to the literature,[85] the adsorption capacity of precursors by

CMSs and the penetration depth inside the CMSs were discovered to have a greater carbonaceous microspheres effect on the formation of the shell layer. Therefore, with the increase of adsorption time, the amount of adsorbed metal ions by CMSs and the penetration depth of titanium ions inside the spheres gradually increase, resulting in a double-layer shape.

2.4.1.2 Pretreatment of CMSs by Ethanol

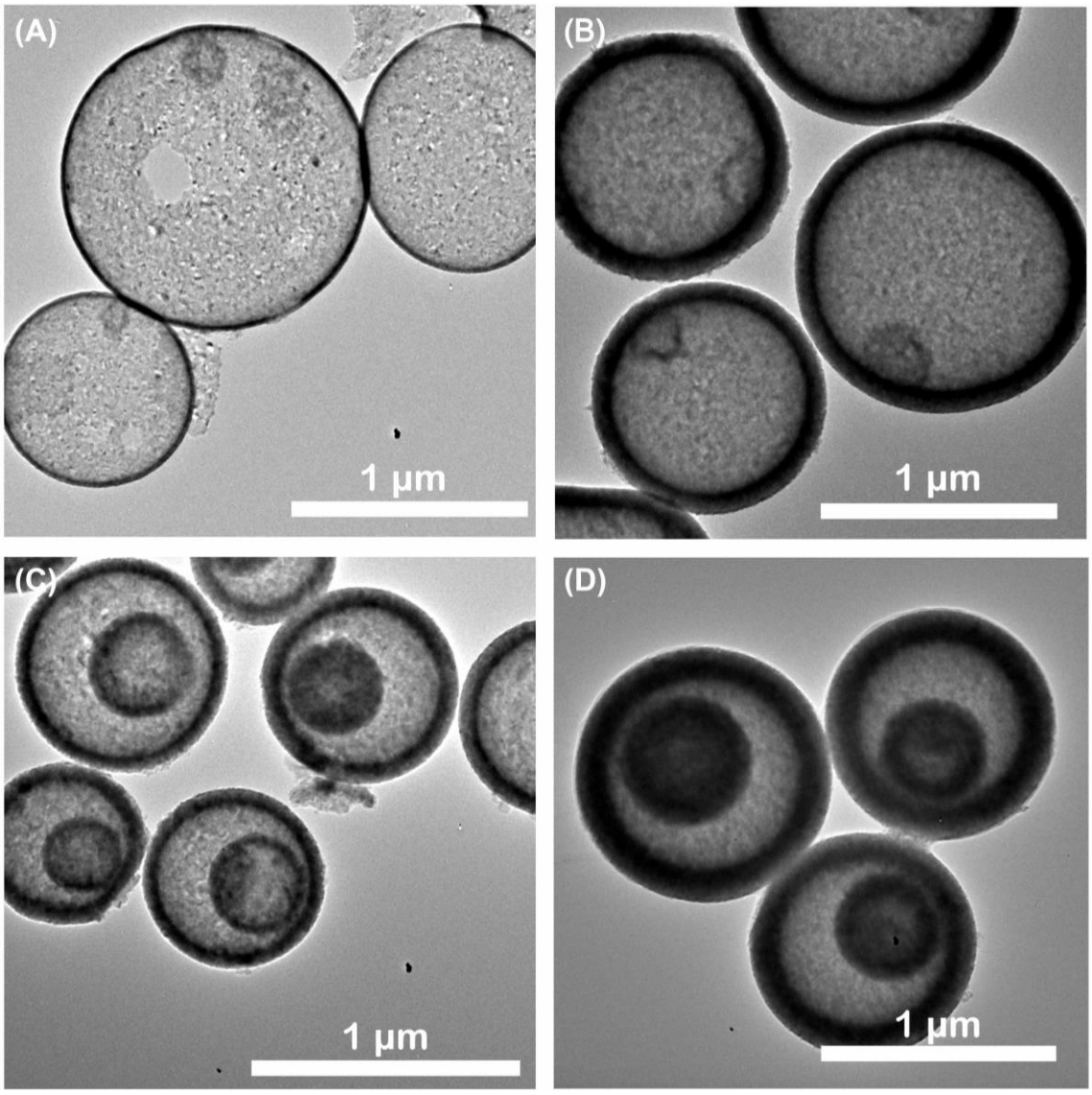

Figure 2.3 TEM images of TiO_2 samples synthesized by carbonaceous microspheres pretreated with different duration times by ethanol: (A) 0 hours, (B) 1 hour, (C) 4 hours, and (D) 18 hours. The adsorption duration time is 6 hours and the heating rate is 5 °C min^{-1}.

To augment the adsorption and penetration depth of titanium precursor by CMSs, the CMSs were pretreated by ethanol and adsorbed under the 40 °C water bath condition. The pretreatment durations were 0 hours, 1 hour, 4 hours, and 18 hours. The pretreated CMSs

were employed as templates to adsorb metal ions, and the TEM images of the obtained samples were shown in Figure 2.3. To contrast the effect of pretreatment on the synthesis of HoMSs, without pretreatment of CMSs were also adsorbed in a water bath at 40 °C as a control sample, as shown in Figure 2.3A. Compared with the adsorption at room temperature (figure 2.2 B), the sample under 40 °C water bath condition forms a bilayer shape of TiO_2 HoMSs. When the pretreatment time of carbonaceous microspheres is 1 hour (figure 2.3B), the thickness of the shell layer of the sample obtained is about 100 nm. While a smaller hollow sphere of TiO_2 was present inside HoMSs. When the pretreatment time is extended to 4 hours, the thickness of the inner shell layer of the double TiO_2 HoMSs changed to thicker. When the pretreatment time was further extended to 18 h, the three-shell layer of TiO_2 HoMSs is formed. The pretreatment improves shells number of samples.

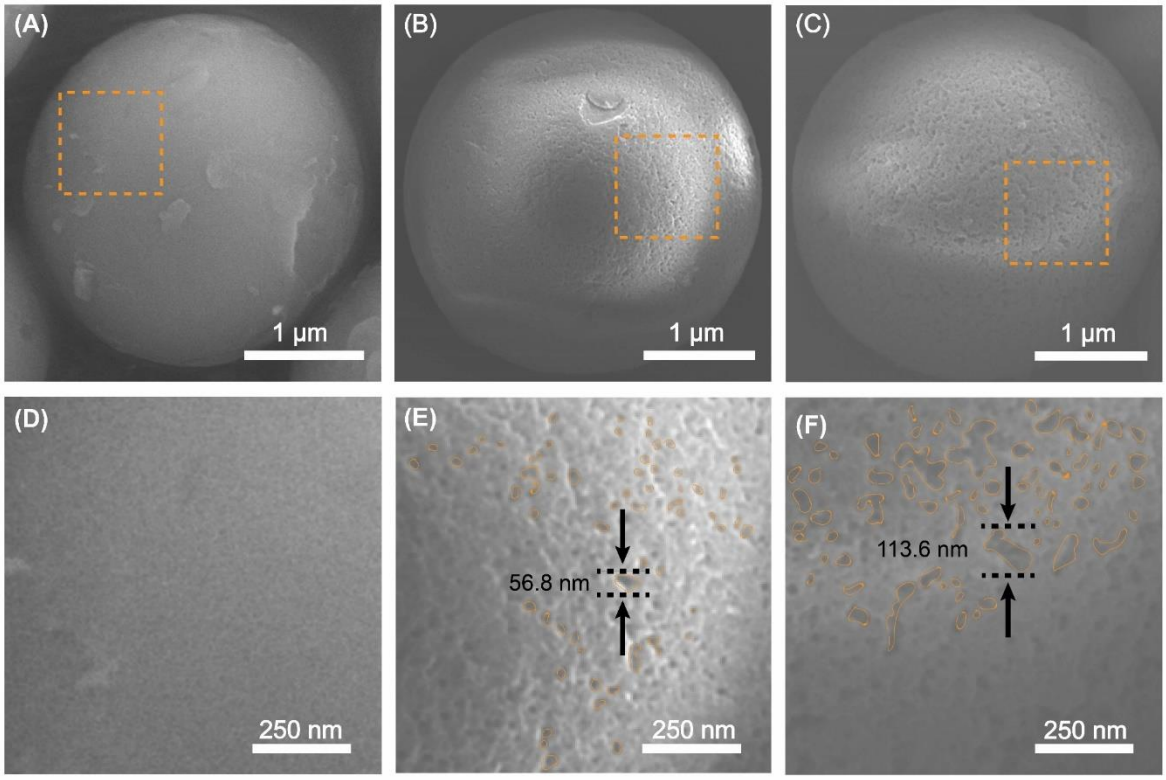

Figure 2.4 High-resolution SEM images of carbonaceous microspheres pretreated by ethanol at different times: (A) and (D) 0 hours; (B) and (E) 4 hours; (C) and (F) 18 hours.

For purpose of comparative effect of ethanol on the morphology of CMSs, the SEM characterization of CMSs with different pretreatment times was performed, and the results were shown in Figure 2.4. The surface of the CMSs without ethanol washing presents smooth and without obvious pore channels. When the CMSs are washed with ethanol for 4 hours, the surface of the CMSs is rougher and the pore size of the surface reaches 56.8 nm. When the

ethanol washing duration of the CMSs is further extended to 18 hours, the pore size of the CMSs surface reaches a peak at 113.6 nm. The pores size on the surface of CMSs increases after the pretreatment of CMSs by ethanol. These pores may contribute to easier penetration of the titanium sources into the interior of the CMSs.

To investigate the effect of ethanol pretreatment on the surface groups of CMSs, FT-IR spectrums have been performed, and the results were as shown in figure 2.5. The spectra at 3200-3700 cm^{-1} correspond to characteristic peaks of O-H (hydroxyl or carboxyl) stretching vibrations.[128-129] The peak position at 2926 cm^{-1} corresponds to the characteristic peak of C-H stretching vibrations. Meanwhile, the peak position at 800 cm^{-1} corresponds to the out-of-plane bending vibrations of C-H.[129] The peak position at 1712 cm^{-1} corresponds to the C=O stretching vibration peak, which may originate from quinone, carbonyl, and ester.[127, 130] The peaks at 1618 cm^{-1} and 1514 cm^{-1} correspond to C=C vibrational absorption peaks. The peak position at 1022 cm^{-1} corresponds to the C-O stretching vibration, which may be derived from hydroxyl, ether, or ester).[125] In comparation with the CMSs, the positions of the vibrational absorption peaks of the different groups do not change for the CMSs pretreated with ethanol for 4 hours and 18 hours. This result suggests that the group species on the surface of the carbonaceous microspheres remained unchanged after ethanol washing.

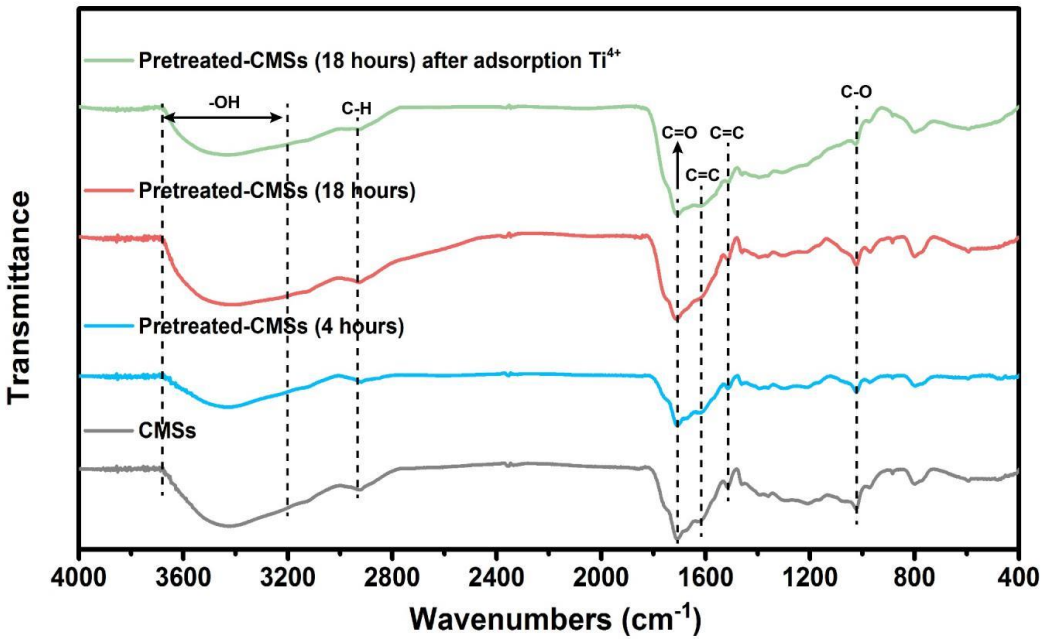

Figure 2.5 The FT-IR spectra of carbonaceous microspheres washed by ethanol at different times.

To investigate the surface potential of CMSs, the Zeta potential of CMSs pretreated by ethanol

at different times was tested as shown in figure 2.6. Compared with the potential of CMSs without pretreated (-58.2 mV), there is no more difference in Zeta potential for pretreatment time at 4 h (-57 mV) and 18 h (-57.4 mV). The surface electronegativity is possibly caused by hydroxy groups on the surface. The electronegativity is beneficial to adsorb titanium precursors. Almost constant Zeta potential means pretreatment will not enhance the numbers of hydroxy groups on the surface. Hence, the increased number of TiO_2 shells in figure 2.3 is possibly induced by the pores size of pretreated CMSs.

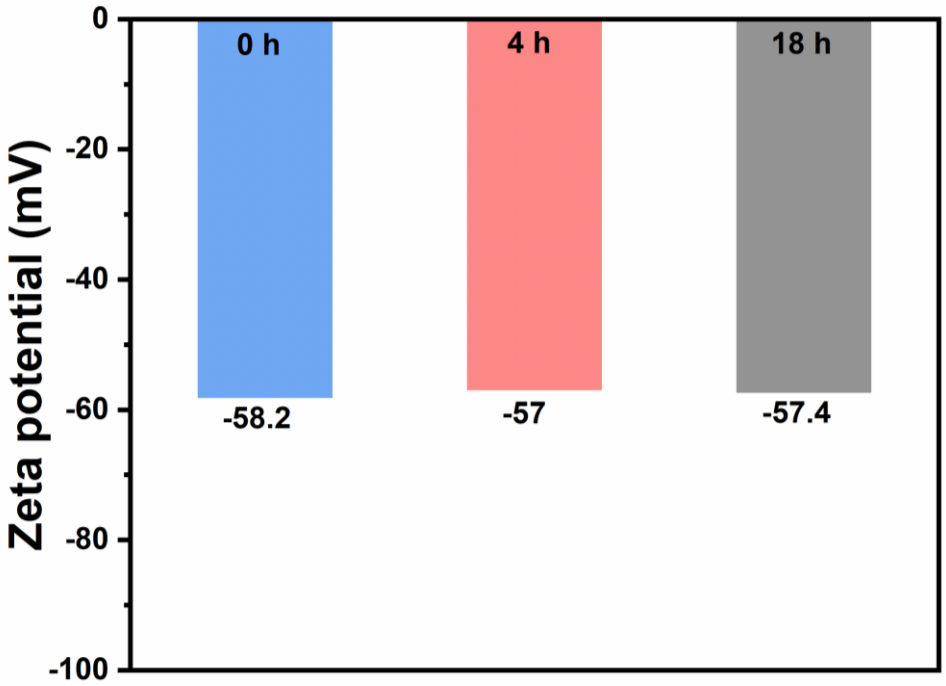

Figure 2.6 The Zeta potential of CMSs pretreated by ethanol at different times.

2.4.1.3 Effect of Heating Rate

To prepare titanium oxide with a thinner shell layer thickness, reducing the amount of precursor adsorption can be realized by decreasing the CMSs adsorption time. On the other hand, the heating rate of calcination temperature requires matching the removal rate of the CMSs template. Therefore, regulating different temperature heating rates during calcination is experimentally performed to contribute to the generation of multi-shell layers of TiO_2 HoMSs, and the TEM results were shown in Figure 2.7. With the heating rate increasing from 5 °C min^{-1} to 9 °C min^{-1}, the shell numbers of TiO_2 HoMSs are increased from 2 to 3 shells. This is mainly caused by the increment in the removal rate of CMSs template as the heating rate increases. When the removal of the CMSs template is accelerated in calcination, the titanium precursors adsorbed on the template are gradually formed as titanium oxide shell layers under the atmosphere of air. The first one is the presence of sufficient precursor ions

inside the CMSs template in a certain penetration depth. For the second and third shells, the removal rate of the CMSs template with an appropriate matching relationship to the oxide shell layer formation rate is required.

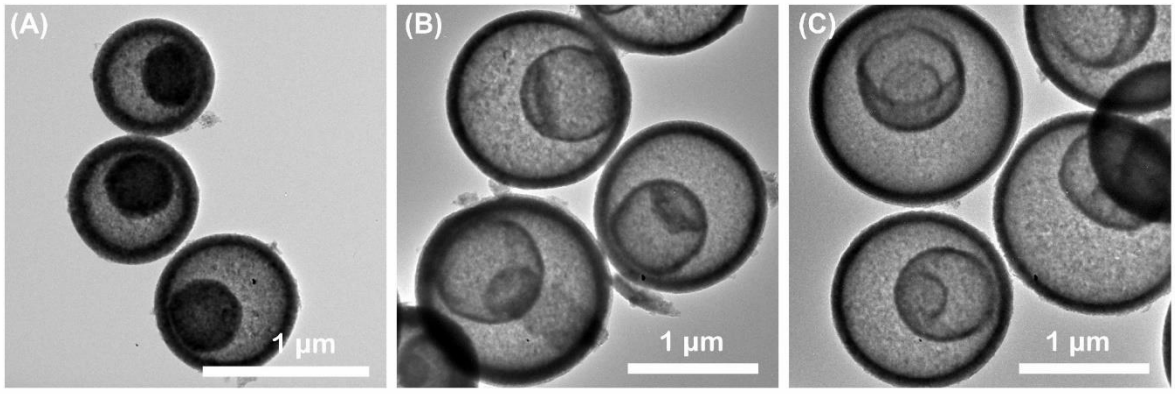

Figure 2.7 TEM images of TiO_2 samples with different heating rate: (A) 5 °C min^{-1}, (B) 7 °C min^{-1}, and (C) 9 °C min^{-1}. The CMSs were treated with ethanol for 4 hours and the adsorption duration time was 7 hours.

2.4.1.4 Characterizations of TiO_2 HoMSs

According to the TEM results of TiO_2 HoMSs in the above parts and further trial experiments, the preparation conditions of single, double, and triple shells were obtained. And these synthetic experiment parameters of TiO_2 HoMSs were summarized as shown in Table 2.1. The XRD spectra of TiO_2 HoMSs exhibited in Figure 2.8 reveal that the TiO_2 HoMSs is mixed phases of anatase (JCPDF: 21-1272) and rutile (JCPDF: 21-1276). Compared with the standard PDF cards, the diffraction spectra with 2θ at 25.5, 38.1, 48.3, 54.5(55.3), 62.9, 69.2 (70.6) correspond to anatase (101), (103), (200), (105), (213), (116) crystal planes. Simultaneously the diffraction spectra of 2θ at 27.7, 36.2, 41.6 are referred to as rutile (JCPDF: 21-1276) (110), (101), (111) crystalline planes. The weight fraction of rutile (W_R) is calculated by equation 2.1:[103]

$$W_R = \frac{A_R}{0.884A_A + A_R} \qquad 2.1$$

where A_A is the integrated intensity of the anatase (101) peak, and A_R is the integrated intensity of the rutile (110) peak. The computation results yielded about 4:1 for anatase compared with rutile.

Raman spectrum is a useful characterization for investigating the structure phase of materials. The Raman spectra were used to study the phase of anatase TiO_2 or rutile TiO_2 as shown in

figure 2.9. The characteristic peaks of anatase and rutile likewise confirm that the TiO_2 HoMSs are mixed phases. The peaks in spectra at 140 cm^{-1}, 392 cm^{-1}, 515.8 cm^{-1}, 636 cm^{-1} correspond to anatase phase.[131-132] The peaks at 443 cm^{-1} and 612 cm^{-1} present the rutile phase.[132]

Table 2.1 The synthetic experiment parameters of TiO_2 HoMSs used in the following experiments.

Sample	Pretreatment time (h)	Adsorption time (h)	Temperature (°C)	Heating rate (°C/min)
1S-TiO_2 HSs	0	6	Room temperature	5
2S-TiO_2 HoMSs	4	5	40	7
3S-TiO_2 HoMSs	4	7	40	9

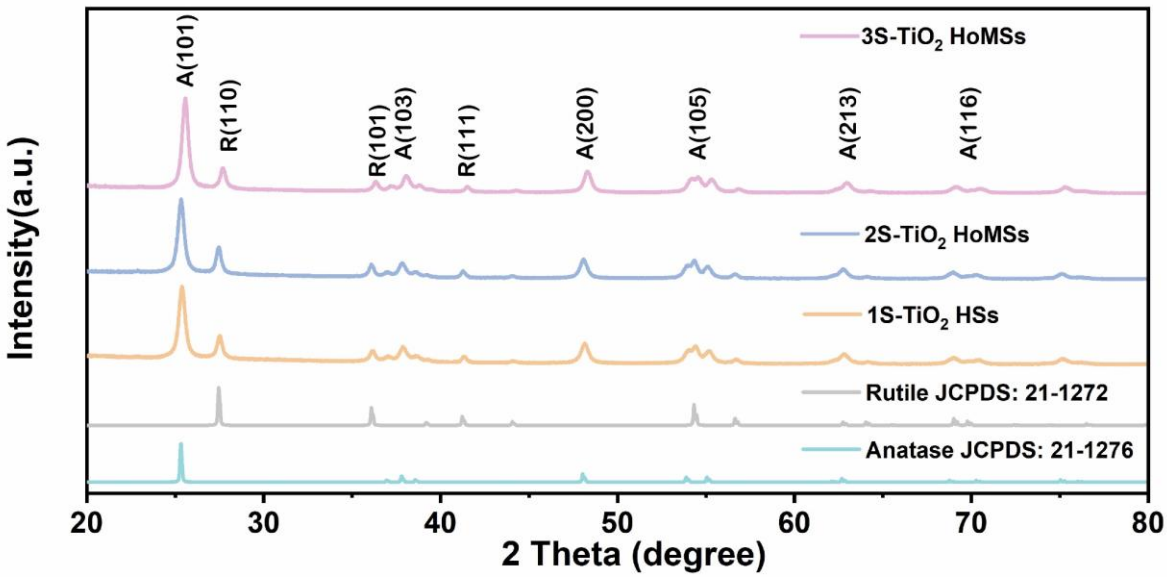

Figure 2.8 XRD patterns of TiO_2 HoMSs calcined at 550 °C.

To further characterize the crystallization of TiO_2 HoMSs, SAED and HRTEM characterizations of 3S-TiO_2 HoMSs were carried out, and the results are shown in Figure 2.10. The SAED pattern consists of multiple bright and dark diffraction rings, indicating that the synthesized 3S-TiO_2 HoMSs are polycrystalline oxides. The formation of polycrystals is mainly explained by the fact that each shell layer of TiO_2 HoMSs is composed of multiple nanoparticles. In addition, the lattice diffraction streaks with good crystallinity appears in the HRTEM results, corresponding to (101) facets of anatase and (110) facets of rutile, respectively. The analysis of the above results concludes that the TiO_2 HoMSs prepared by

the STA method is a mixed phase with a 4:1 ratio of anatase and rutile phases, and polycrystalline TiO_2 with good crystallinity.

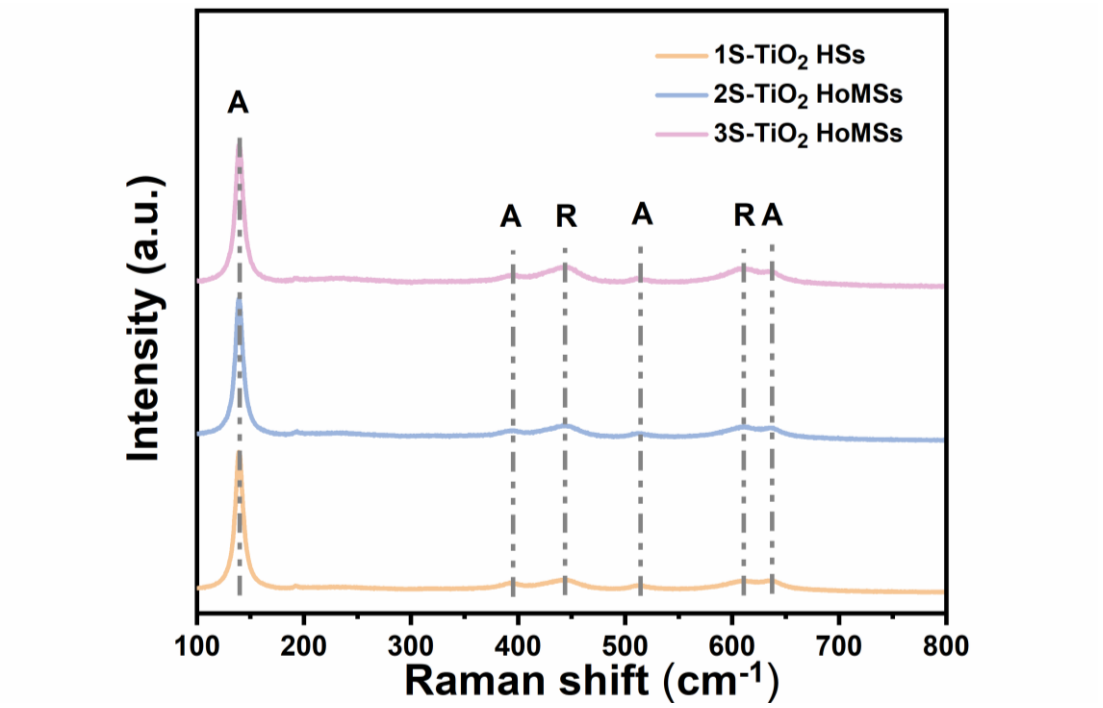

Figure 2.9 Raman spectrum of TiO_2 HoMSs, A presents anatase TiO_2 and R presents rutile TiO_2.

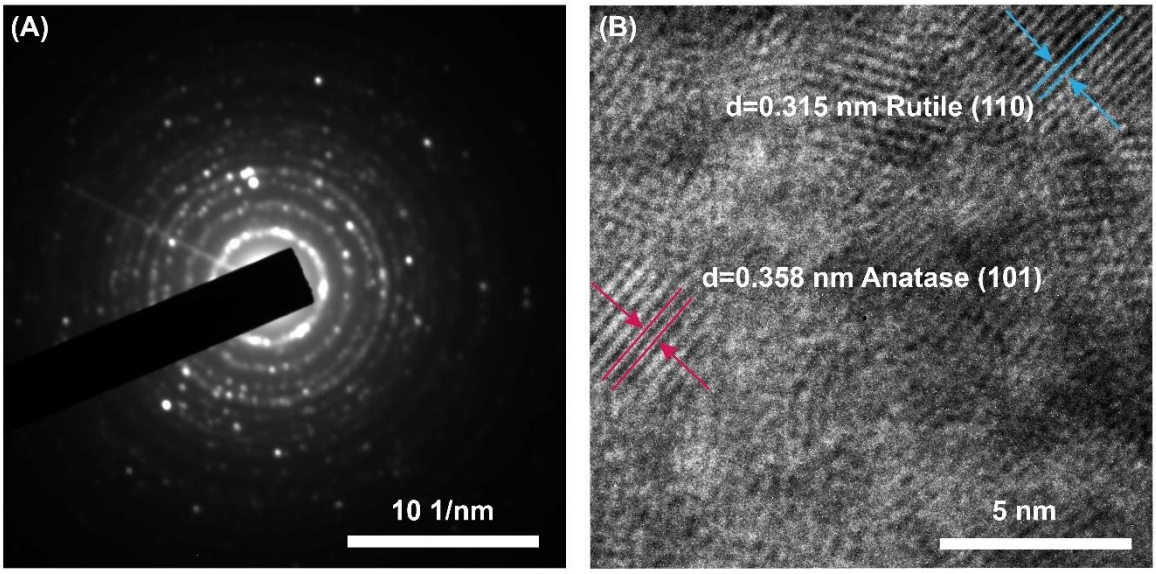

Figure 2.10 (A) SAED pattern of 3S-TiO_2 HoMSs; (B) HRTEM image of 3S-TiO_2 HoMSs.

Aiming to evaluate more whether there are defects on the surface of titanium oxide, XPS characterization of 3S-TiO_2 HoMSs was performed, and the results were shown in Figure

2.11. Figure 2.11A presents the XPS full spectrum of 3S-TiO_2 HoMSs, and peaks corresponding to O1s and Ti 2p can be detected. Further study of the High-resolution XPS Ti 2p orbital spectra of 3S-TiO_2 HoMSs in figure 2.11B, the peak positions at 464.5 eV and 458.7 eV correspond to Ti $2p_{1/2}$ and Ti $2p_{3/2}$ of anatase. And this result indicates that Ti exists at +4 valence.[133-134] In addition, in the high-resolution XPS O 1s orbital spectra of 3S-TiO_2 HoMSs in figure 2.11C, the O1s peaks of surface hydroxyl oxygen, Ti-O band originated from anatase and rutile are from the left to right side, respectively.[135-136]

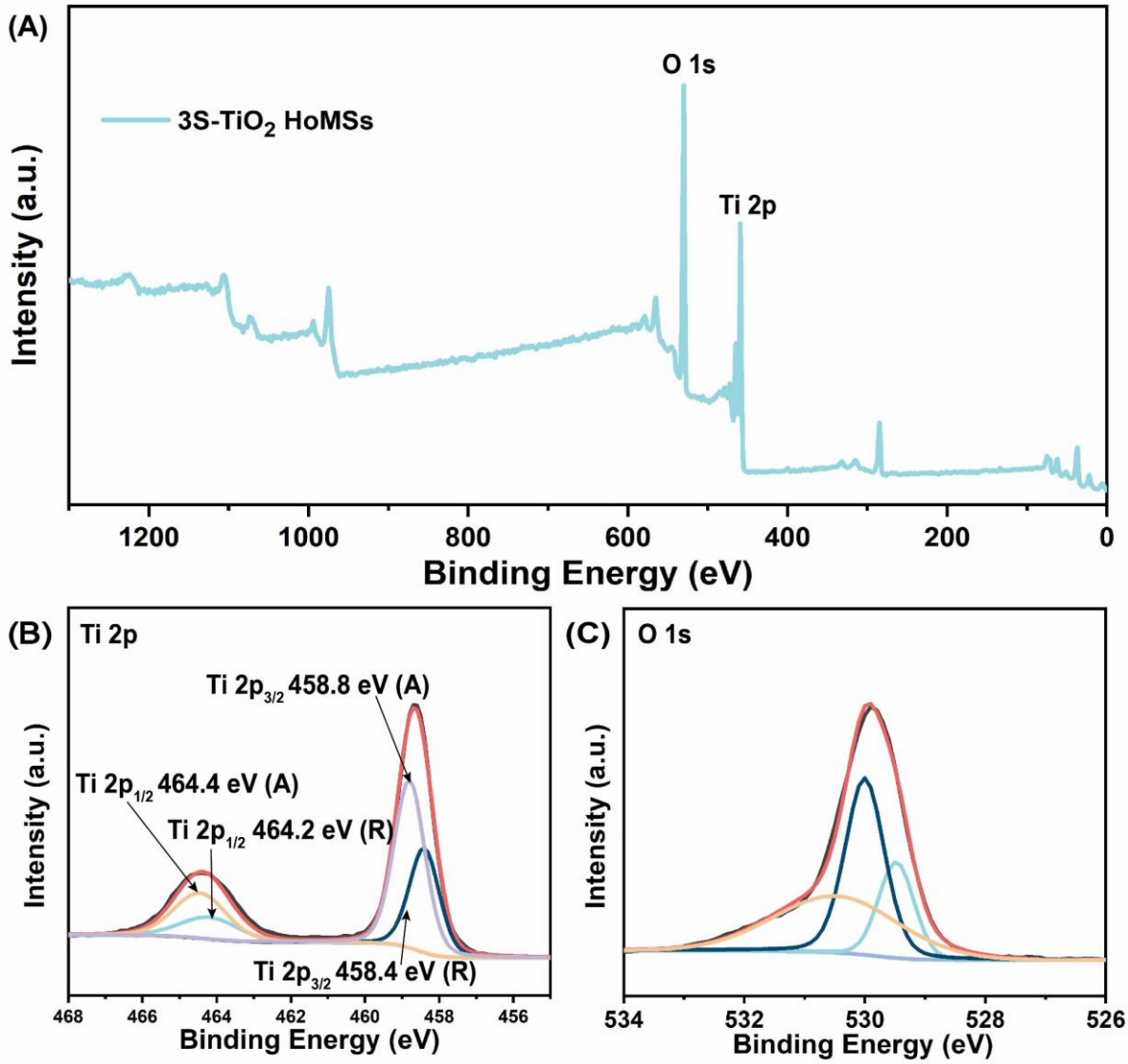

Figure 2.11 (A) XPS survey spectra of 3S-TiO_2 HoMSs; (B) High-resolution XPS Ti 2p orbital spectra of 3S-TiO_2 HoMSs; (C) High-resolution XPS O 1s orbital spectra of 3S-TiO_2 HoMSs.

Eventually, the TiO_2 HoMSs with different shell layers were characterized by SEM and the

results were shown in Figure 2.12. The results indicate that the TiO_2 is composed of multiple nanoparticles, which is consistent with the previously reported results. The outer shell layer, as well as the inner core, are visible through the broken HoMSs. The particle size statistics of the TiO_2 HoMSs reveal that the size distribution range of TiO_2 is mainly concentrated around 1 μm. The average particle sizes of 1S-TiO_2 HSs, 2S-TiO_2 HoMSs, and 3S-TiO_2 HoMSs are 1.04 μm, 1.01 μm, and 1.02 μm, respectively.

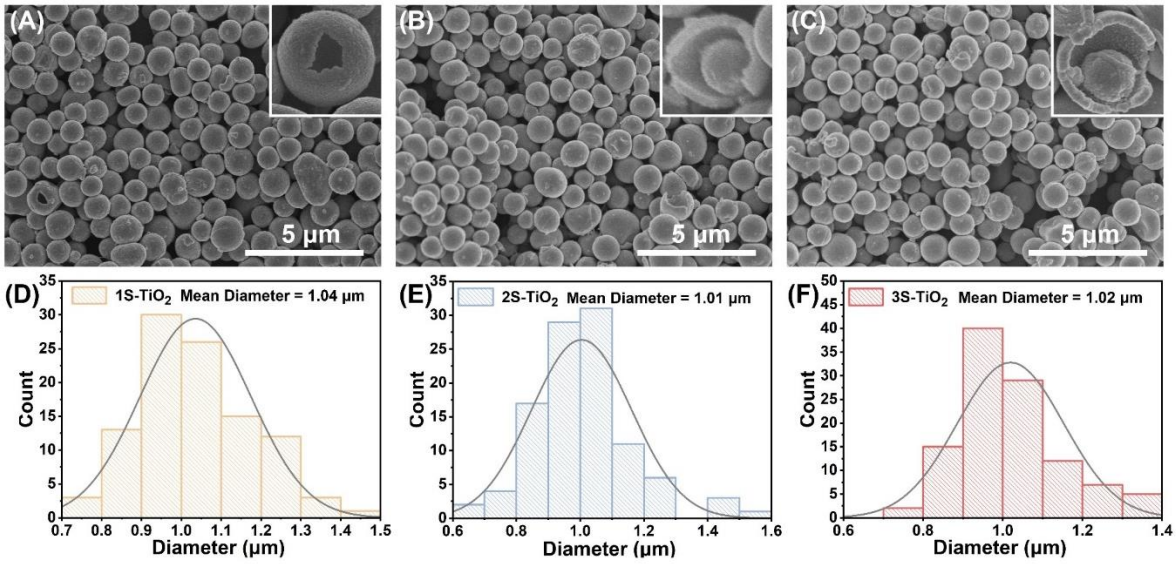

Figure 2.12 SEM images and corresponding diameter statistics of TiO_2 HoMSs: (A) and (D) 1S-TiO_2 HSs, (B) and (E) 2S-TiO_2 HoMSs, (C) and (F) 3S-TiO_2 HoMSs.

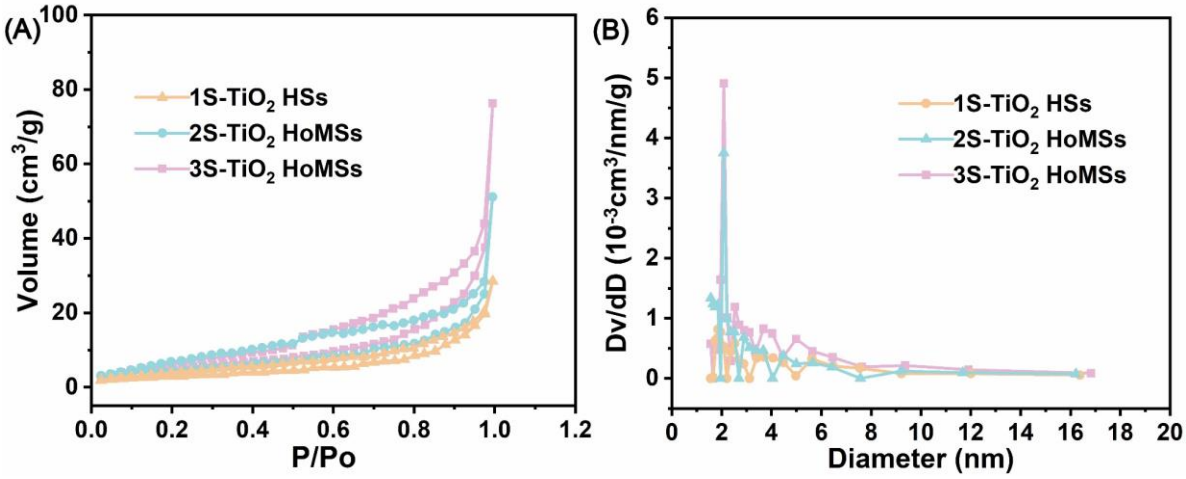

Figure 2.13 (A) The Nitrogen adsorption-desorption isotherms of TiO_2 HoMSs; (B) The BJH pore size distributions of TiO_2 HoMSs.

The nitrogen adsorption-desorption isotherm and pore size distribution curves of TiO_2

HoMSs were measured as shown in figure 2.13 and table 2.2. According to the results, the specific surface area of 3S-TiO_2 HoMSs is 19.752 $m^2 \cdot g^{-1}$ which is bigger than 1S-TiO_2 HSs (11.039 $m^2 \cdot g^{-1}$) and 2S-TiO_2 HoMSs (16.375 $m^2 \cdot g^{-1}$). The higher specific surface area of 3S-TiO_2 HoMSs exposes more reaction activity sites. The pore size distribution in figure 2.13B analyzed by Barret Joyner Halenda's (BJH) method shows that the distribution of TiO_2 HoMSs is mainly around a range from 2 nm to 8 nm. These pores provide pathways for impregnating perovskite precursor solution inside TiO_2 HoMSs. Similarly, the 3S-TiO_2 HoMSs presents the highest pore volume (0.118 $cm^3 \cdot g^{-1}$) as shown in table 2.2.

Table 2.2 The values of the specific surface area and pore volume of TiO_2 HoMSs.

Sample	Specific surface area ($m^2 \cdot g^{-1}$)	Pore volume ($cm^3 \cdot g^{-1}$)
1S-TiO_2 HSs	11.039	0.04415
2S-TiO_2 HoMSs	16.375	0.0791
3S-TiO_2 HoMSs	19.752	0.118

2.4.2 Synthesis and Characterizations of Pt/TiO_2

The deposition of platinum (Pt) on TiO_2 HoMSs was carried out by the photo-deposition method. When TiO_2 HoMSs is illuminated under ultraviolet light, photogenerated electrons are excited into the conduction band (CB) and holes stay in the valence band (VB). The $PtCl_6^{2-}$ adsorbed on TiO_2 HoMSs surface reacts with photogenerated electrons to form Pt/TiO_2 HoMSs composites eventually.[137]

To verify the deposition of Pt on TiO_2 HoMSs, the samples were characterized by TEM as shown in figure 2.14. Compared with TEM results of TiO_2 HoMSs in chapter 2, no obvious difference in morphology is observed, suggesting no big Pt clusters formed. But the HRTEM results as shown in figure 2.14D, there are two kinds of lattice fringes which correspond to anatase (101) and Pt (111). To survey the distribution of Pt elements, the EDX mappings were measured as shown in figure 2.14E. The elements distribution of Ti, O, and Pt are shown as green, red, and yellow, respectively. The distributions of Ti and O elements are completely in conformity. Besides, the distribution range of Pt is consistent with the morphology of TiO_2 HoMSs. This result indicates that platinum grains disperse well on the surface of the TiO_2 substrate.

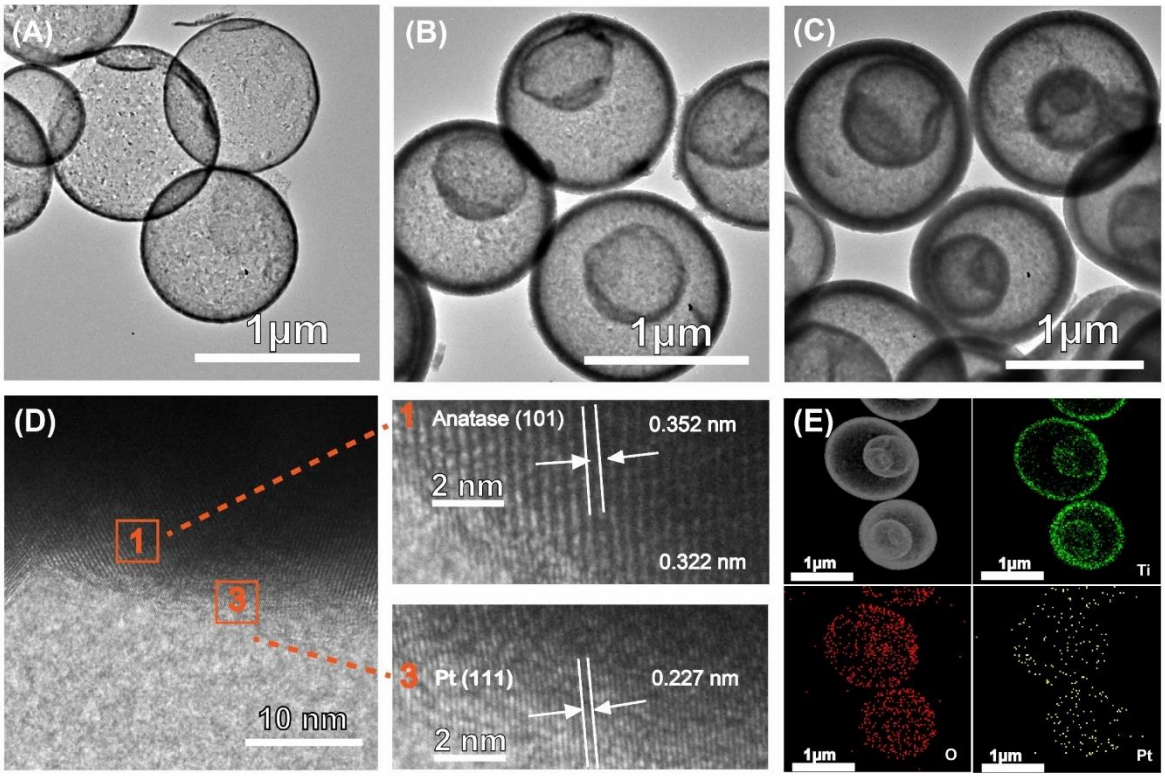

Figure 2.14 TEM images of Pt/TiO_2 HoMSs: (A) Pt/TiO_2-1S HSs, (B) Pt/TiO_2-2S HoMSs, and (C) Pt/TiO_2-3S HoMSs. (D) HRTEM images of Pt/TiO_2-3S HoMSs; (E) The elemental mappings of $Pt/3S\text{-}TiO_2$ HoMS show the distribution of Ti (green), O (red), Pt (yellow).

2.4.3 Synthesis and Characterizations of $MAPbI_3/Pt/TiO_2$

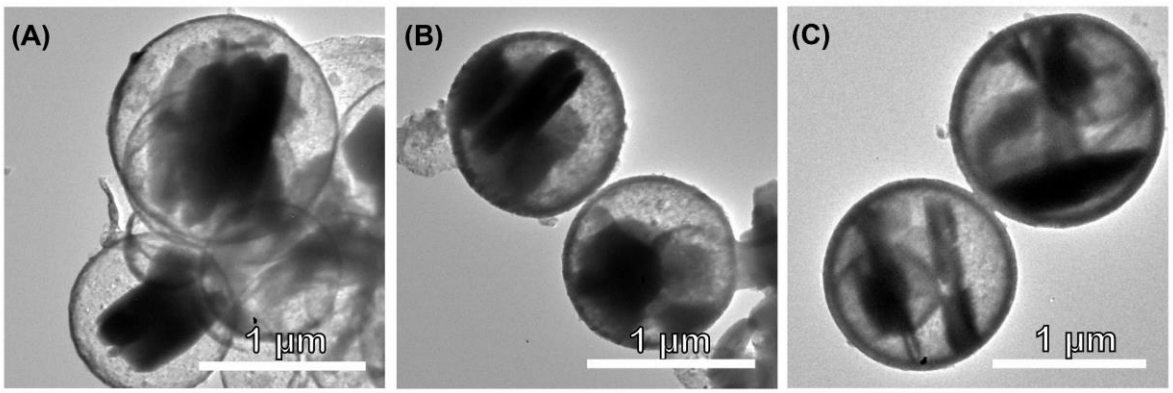

Figure 2.15 TEM images of (A) $MAPbI_3/Pt/1S\text{-}TiO_2$ HSs, (B) $MAPbI_3/Pt/2S\text{-}TiO_2$ HoMSs, (C) $MAPbI_3/Pt/3S\text{-}TiO_2$ HoMSs.

$MAPbI_3/Pt/TiO_2$ HoMSs were constructed by impregnating the perovskite precursor ($MAPbI_3$) solution into the inside cavities of HoMSs and followed by annealing. According to BET results from figure 2.13, the TiO_2 HoMSs possess pores in the shells. The precursor

solution can be introduced inside of HoMSs by capillary action.[138] When removing the organic solvent, the $MAPbI_3$ crystal is formed. Results in figure 2.15 illustrate that the $MAPbI_3$ has been well introduced into the Pt/TiO_2 HoMSs. From the TEM results, the $MAPbI_3$ crystal is distributed in cavities between shells.

To confirm the phase of $MAPbI_3/Pt/TiO_2$ HoMSs, The XRD patterns of samples were carried out as shown in figure 2.16. The diffraction peaks match well with the previous literatures.[99, 139-140] The crystal structure of $MAPbI_3$ belongs to the tetragonal and space group of I4/mcm. The diffraction characteristic peaks of (110), (220), (310), and (314) of $MAPbI_3$ are detected in XRD patterns. In addition, the diffraction characteristic peaks of anatase TiO_2 and rutile TiO_2 match well with the PDF standard card. Hence, the $MAPbI_3/Pt/TiO_2$ HoMSs was synthesized successfully.

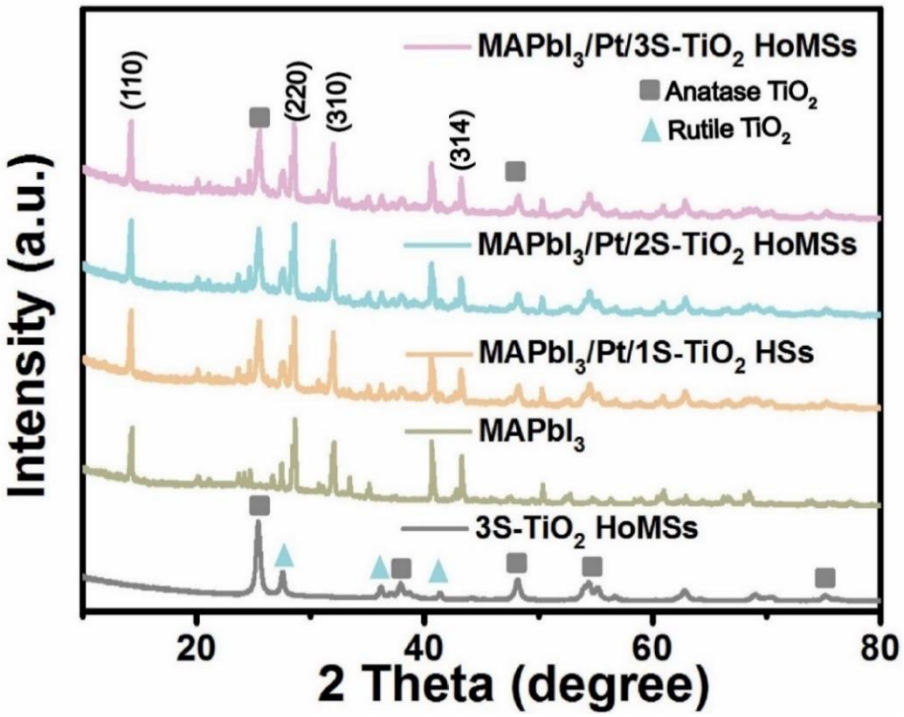

Figure 2.16 XRD patterns of $MAPbI_3/Pt/TiO_2$ HoMSs samples.

To confirm the composited heterostructures and observe the distribution of $MAPbI_3$ in Pt/TiO_2 HoMSs, the high-angle-annular-dark-field scanning transmission electron microscopy (HAADF-STEM) was performed as shown in figure 2.17. Based on the observation of multiple $MAPbI_3/Pt/3S\text{-}TiO_2$ HoMSs in figure 2.17A, the $MAPbI_3$ is almost distributed in cavities between shells. $MAPbI_3$ crystal mainly exists in the outermost cavity because of the largest volume in HoMSs. The EDX spectra of $MAPbI_3/Pt/3S\text{-}TiO_2$ HoMSs indicate elements of Ti, O, Pb, I, N, and Pt have existed in the sample. The single HAADF-STEM image of

$MAPbI_3/Pt/3S\text{-}TiO_2$ HoMSs in figure 2.17C indicates that the Pt element is homogeneously distributed on the $MAPbI_3/Pt/3S\text{-}TiO_2$ HoMSs and the characteristic element Pb of $MAPbI_3$ is mainly dispersed in inside of $MAPbI_3/Pt/TiO_2$ HoMSs.

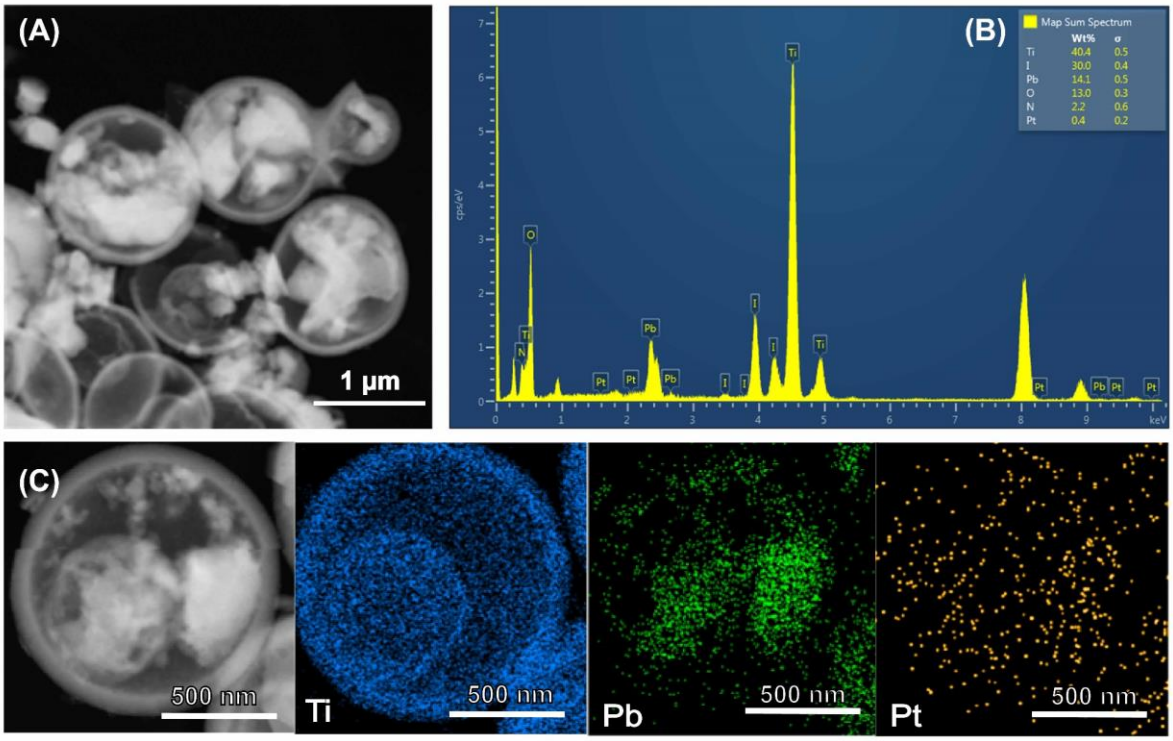

Figure 2.17 (A) HAADF-STEM image of $MAPbI_3/Pt/3S\text{-}TiO_2$ HoMSs; (B) EDX spectra of $MAPbI_3/Pt/3S\text{-}TiO_2$ HoMSs; (C) Elemental mappings of $MAPbI_3/Pt/3S\text{-}TiO_2$ HoMSs show the distribution of Ti (blue), Pb (green), Pt (yellow).

Further, the line scan of $MAPbI_3/Pt/3S\text{-}TiO_2$ HoMSs was also measured as shown in figure 2.18. Because of the different color contrast, it can be observed that there are Pt particles in the $3S\text{-}TiO_2$ HoMSs surface in figure 2.18A. The selection of scan position is shown in figure 2.18B and corresponding line scan spectrums are shown in figure 2.18C. When the scan position is from 0 nm to 350 nm (from left to right in figure 2.18B), the intensity of I and Pb is gradually decreased. This result means that the $MAPbI_3$ crystal is located inside TiO_2 HoMSs. Besides, the intensities of O and Ti gradually increase to a peak and sharply decreased. The result of Ti and O is consistent with hollow structures. In the end, the bright spot on the surface of $3S\text{-}TiO_2$ HoMSs is confirmed as Pt particles by line scan spectrum in figure 2.18C.

To survey the wide range morphology of $MAPbI_3/Pt/TiO_2$ HoMSs, SEM was carried out and images were shown in figure 2.19. There are only a few $MAPbI_3$ crystals around Pt/TiO_2

HoMSs because an additional $MAPbI_3$ precursor solution exists outside of Pt/TiO_2 HoMSs in impregnating process. Compared SEM results of $MAPbI_3/Pt/TiO_2$ HoMSs indicates no apparent difference between different samples. Besides, the SEM mapping results in figure 2.20 show that there are still existing perovskite characteristic elements (Pb and I) although there are no obvious perovskite crystals. The reason for this result is probably caused by $MAPbI_3$ in the surface, pores, or inside HoMSs. The above analysis of XRD, TEM, and SEM proves that the $MAPbI_3/Pt/TiO_2$ HoMSs composited heterostructures are successfully constructed.

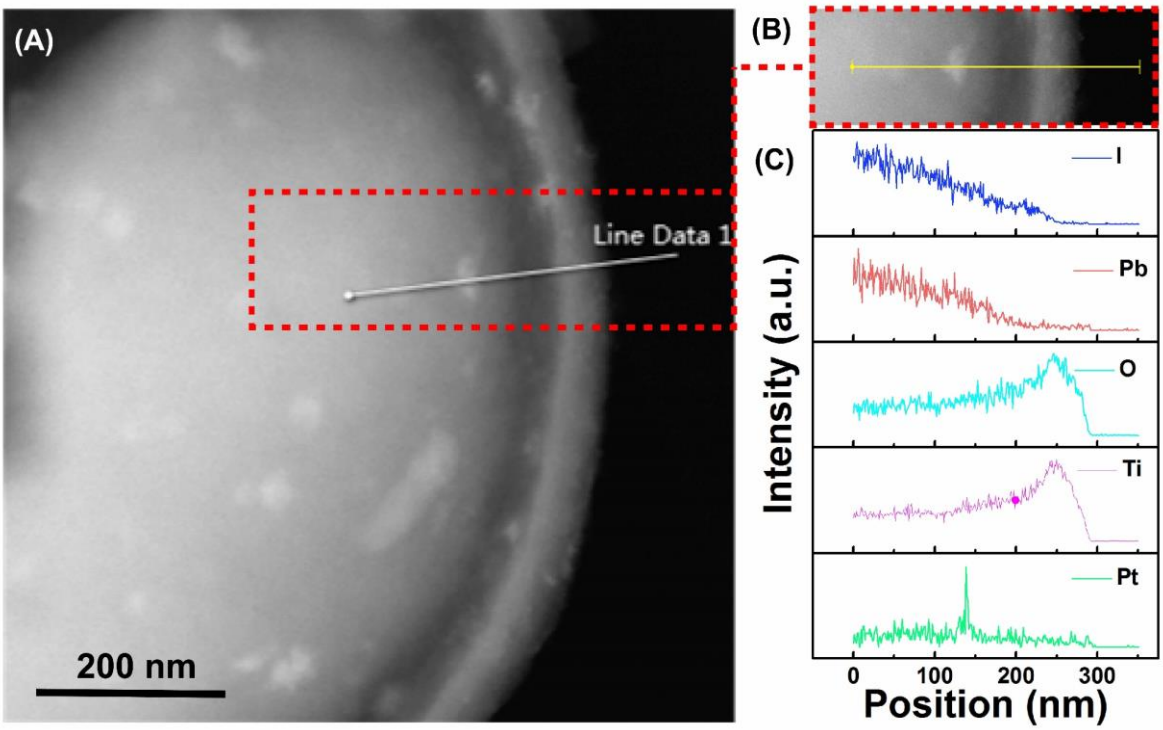

Figure 2.18 (A) TEM image of $MAPbI_3/Pt/3S\text{-}TiO_2$ HoMSs; (B) Line scan of the selection area in figure 3.5A; (C) Line scan spectrum of elements for the selected area.

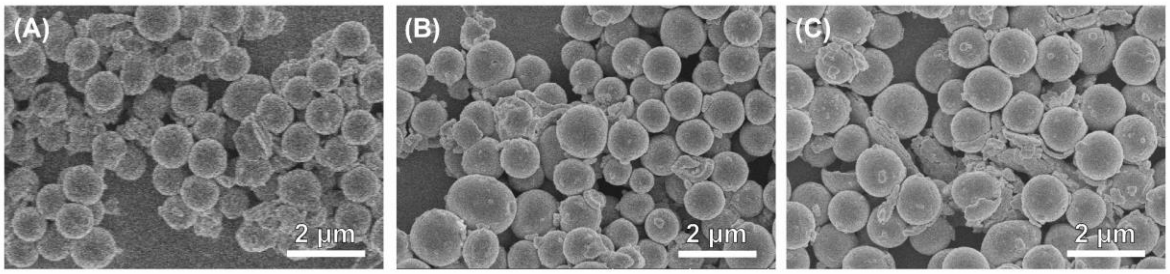

Figure 2.19 SEM images of (A) $MAPbI_3/Pt/1S\text{-}TiO_2$ HSs, (B) $MAPbI_3/Pt/2S\text{-}TiO_2$ HoMSs, and (C) $MAPbI_3/Pt/3S\text{-}TiO_2$ HoMSs

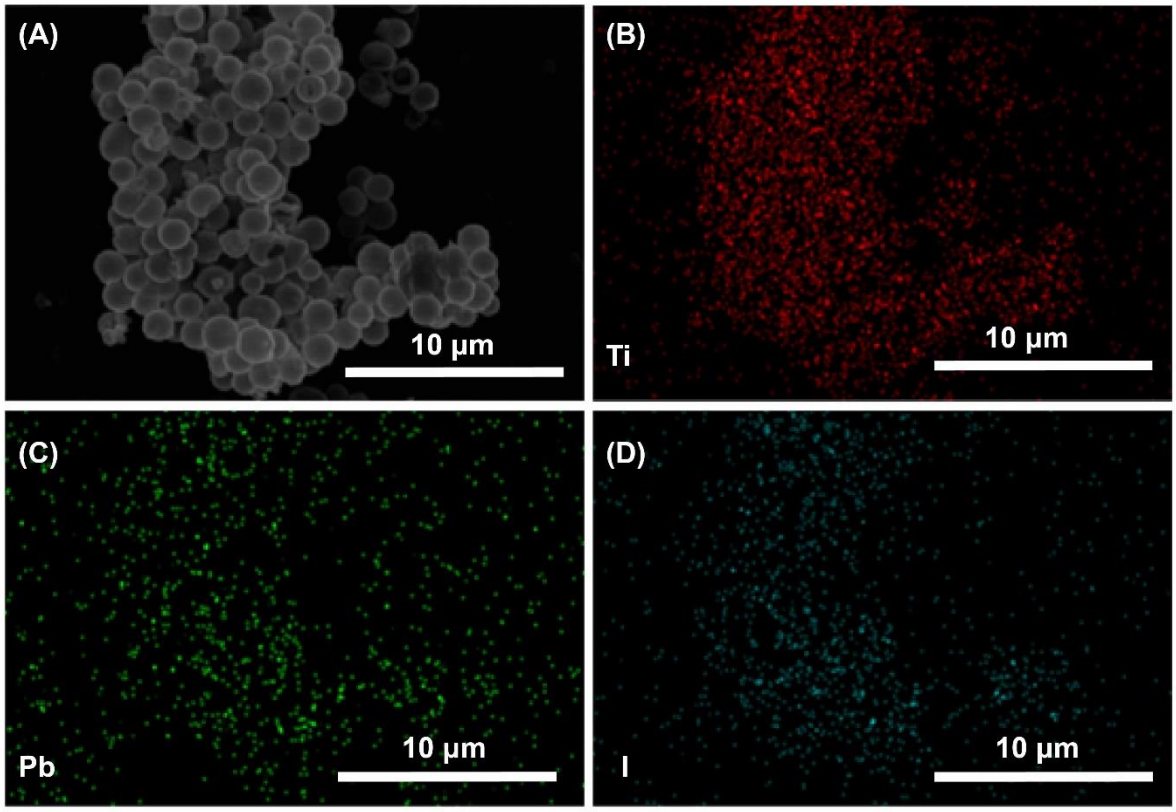

Figure 2.20 SEM mapping images of $MAPbI_3/Pt/3S\text{-}TiO_2$ HoMSs: (A) SEM image, (B) Ti element (red), (C) Pb element (yellow), and (D) I element (blue).

To further verify the surface chemical state of $MAPbI_3/Pt/TiO_2$ HoMSs composites, XPS of samples was measured. Judged from the XPS survey spectra of samples in figure 2.21A, the peaks of orbital of I 3d, O 1s, Ti 2p, Pb 4f, and Pt 4f have existed. The binding energy of XPS was corrected with reference C 1s (284.8 eV) as shown in figure 2.21B. Comparing high-resolution XPS Pb 4f orbital spectra of $MAPbI_3$ and $MAPbI_3/Pt/3S\text{-}TiO_2$ HoMSs in figure 2.21C, the blinding energy peaks of Pb 4f orbital in $MAPbI_3/Pt/3S\text{-}TiO_2$ HoMSs reduce 0.5 eV. which means $MAPbI_3$ in $MAPbI_3/Pt/3S\text{-}TiO_2$ HoMSs is more stable than $MAPbI_3$. Besides, the difference in the Pb 4f XPS between $MAPbI_3$ and $MAPbI_3/Pt/3S\text{-}TiO_2$ HoMSs suggests the contact between the Pt/TiO_2 and $MAPbI_3$. The high-resolution XPS Pt 4f orbital spectra have the differences between $Pt/3S\text{-}TiO_2$ HoMSs and $MAPbI_3/Pt/3S\text{-}TiO_2$ HoMSs. The Pt $4f_{5/2}$ orbital peak of $Pt/3S\text{-}TiO_2$ HoMSs is symmetric. But the asymmetric Pt $4f_{5/2}$ orbital peak of $MAPbI_3/Pt/3S\text{-}TiO_2$ HoMSs indicates the interaction between $MAPbI_3$ and Pt particles. In addition, the peaks of Pt $4f_{5/2}$ (74.7 eV) and Pt $4f_{7/2}$ (71.3 eV) show that the Pt in the surface of TiO_2 is zero-valent state metallic Pt.[141] The high-resolution XPS N 1s orbital spectra in figure 2.21E appears at 402.2 eV correspond to the bond of N-C of perovskite.[142] Meanwhile, there is a new peak at 401.6 eV which possibly stems from the relationship

between N in $MAPbI_3$ and Pt particles.

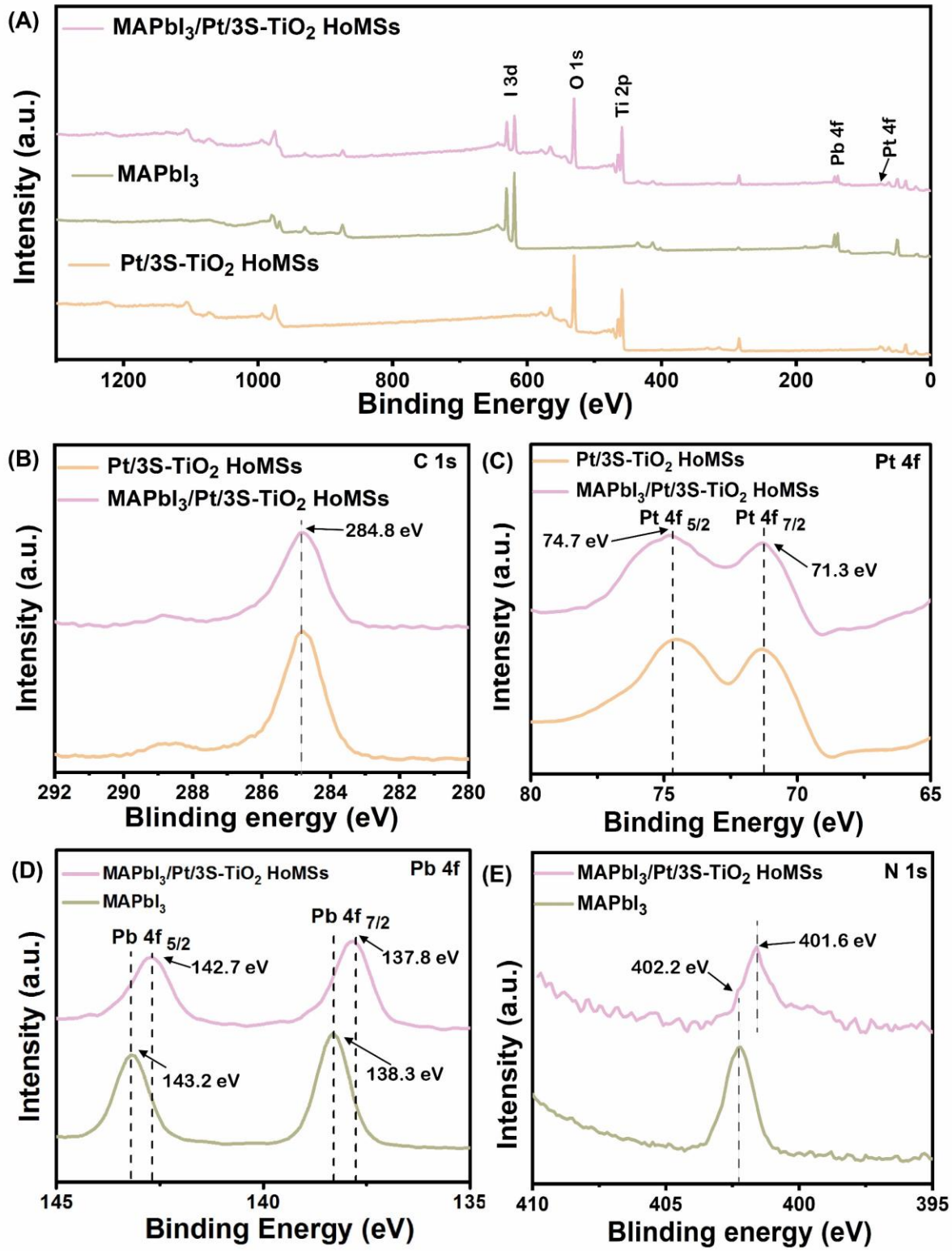

Figure 2.21 (A) XPS survey spectra; (B) High-resolution XPS C 1s orbital spectra of Pt/3S-TiO_2 HoMSs and $MAPbI_3$/Pt/3S-TiO_2 HoMSs; (C)High-resolution XPS Pb 4f orbital spectra of $MAPbI_3$ and $MAPbI_3$/Pt/3S-TiO_2 HoMSs; (D) High-resolution XPS Pt 4f orbital spectra

of Pt/3S-TiO_2 HoMSs and $MAPbI_3$/Pt/3S-TiO_2 HoMSs; (E) High-resolution XPS N 1s orbital spectra of Pt/3S-TiO_2 HoMSs and $MAPbI_3$/Pt/3S-TiO_2 HoMSs.

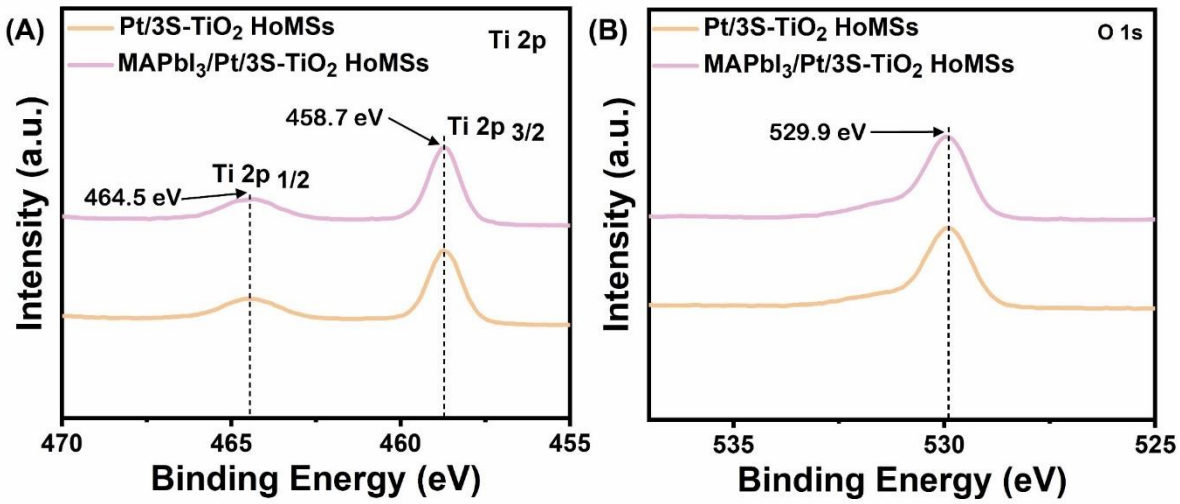

Figure 2.22 High-resolution (A) Ti 2p XPS and (B) O 1s XPS of different catalysts.

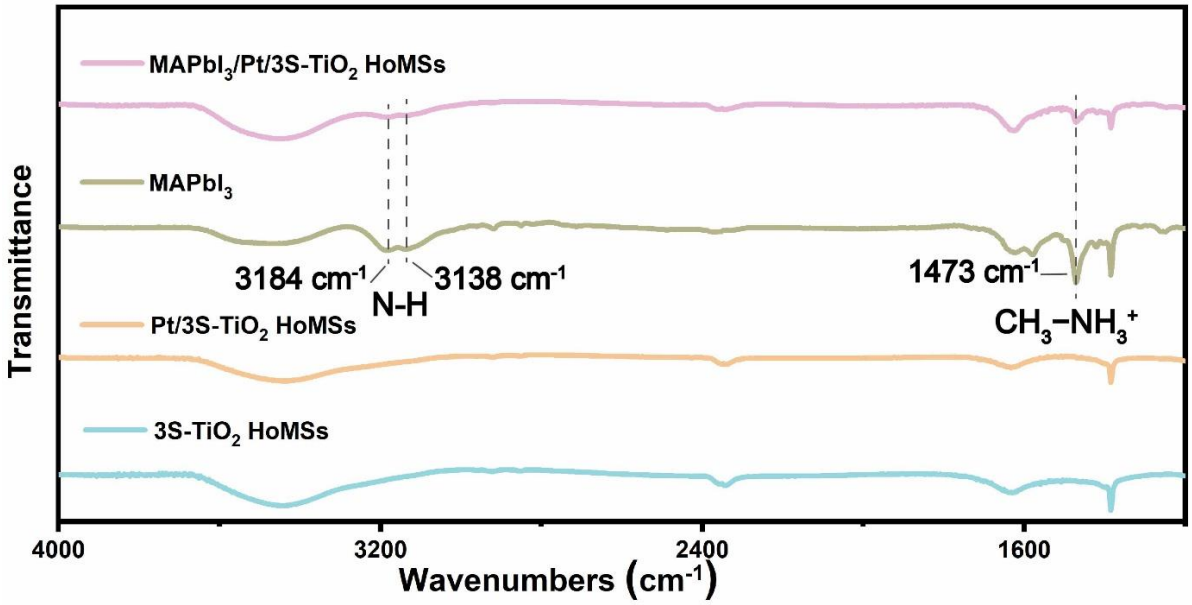

Figure 2.23 FTIR spectra of 3S-TiO_2 HoMSs, $MAPbI_3$, Pt/3S-TiO_2 HoMSs and $MAPbI_3$/Pt/3S-TiO_2 HoMSs.

The high-resolution XPS Ti 2p and O1s orbitals are further investigated as shown in figure 2.22. The peaks at 464.5 eV and 458.7 eV of the Ti 2p XPS spectrum prove that the valence of Ti on the surface of TiO_2 HoMSs is Ti^{4+}.[143] Meanwhile, the peak at 529.9 eV of O 1s XPS in figure 2.22B is assigned to the Ti-O bond without obvious defect on the surface of TiO_2 HoMSs.[143] The FTIR spectra (figure 2.23) show that the asymmetric and symmetric N-H stretching of doublet peaks at 3184 cm^{-1} and 3138 cm^{-1} and CH_3-NH_3^+ at 1473 cm^{-1} are

presented. The N-H and CH_3-NH_3^+ are attributed to methyl formamide in $MAPbI_3/Pt/TiO_2$.[144] The FTIR spectra also suggests that the $MAPbI_3/Pt/TiO_2$ HoMSs composited heterostructures are successfully constructed.

To compare the pore size before and after loading $MAPbI_3$, the pore distribution of $MAPbI_3/TiO_2$ HoMSs was measured as shown in figure 2.24. The range of pore size distribution of $MAPbI_3/TiO_2$ HoMSs is consistent with TiO_2 HoMSs. Compared with pore size distribution curves of TiO_2 HoMSs in figure 2.12B, the pore volume $MAPbI_3/3S$-TiO_2 HoMSs decreases from 0.118 $cm^3 \cdot g^{-1}$ to 0.098 $cm^3 \cdot g^{-1}$. Meanwhile, the pore volumes of $MAPbI_3/1S$-TiO_2 HSs and $MAPbI_3/2S$-TiO_2 HoMSs are 0.042 $cm^3 \cdot g^{-1}$ and 0.074 $cm^3 \cdot g^{-1}$. Decreased pore volume indicates that the $MAPbI_3$ exists in the pores of shells. The pores in shells provide pathways of mass transfer for photocatalytic reaction.

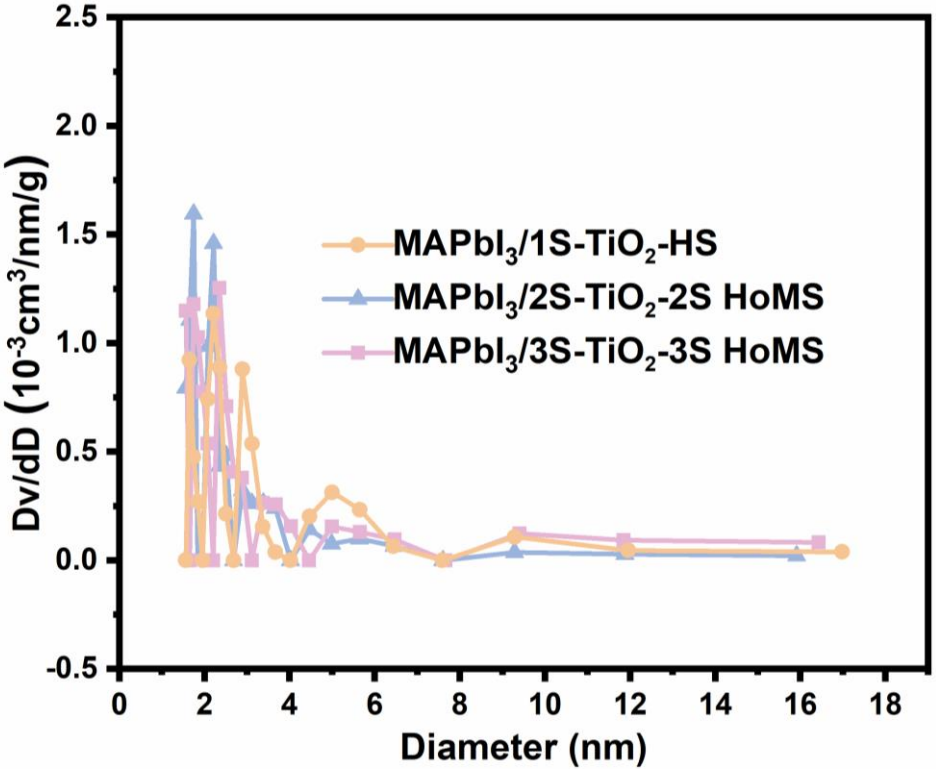

Figure 2.24 The BJH pore size distribution curves of $MAPbI_3/TiO_2$ HoMSs

2.5 Conclusions

In this chapter, 1-3 shells of TiO_2 HoMSs were synthesized using the STA method by the way of adjusting adsorption time, CMSs pretreatment, and temperature heating rate. The longer adsorption time and pretreatment of CMSs contribute to the adsorption of more Ti precursors in the CMSs template. The TiO_2 HoMSs obtained in this chapter is a mixed phase of rutile

and anatase with a ratio of 4:1. In addition, the TiO_2 HoMSs are polycrystalline materials with good crystallinity. By SEM characterization and statistics of 1-3S TiO_2 HoMSs, the average particle sizes of 1S-TiO_2 HSs, 2S-TiO_2 HoMSs, and 3S-TiO_2 HoMSs are close to each other, which are 1.04 μm, 1.01 μm and 1.02 μm, respectively. In addition, the photocatalysts of $MAPbI_3$/Pt/TiO_2 HoMSs were successfully synthesized by the impregnation method and confirmed by XRD, TEM, and STEM-Mapping.

CHAPTER 3.

Application of $MAPbI_3/Pt/TiO_2$ Composites for Visible-Light Photocatalytic Hydrogen Evolution

3.1 Abstract

Charges separation and transfer process has been proved as an important impactor on the photocatalytic activity. In this chapter, the photocatalysts of $MAPbI_3/Pt/TiO_2$ HoMSs composites with the heterogeneous interface between $MAPbI_3$ and TiO_2 HoMSs were applied in photocatalytic hydrogen evolution. The TiO_2 HoMSs provide abundant contact points and reaction active sites. Heterogeneous interfaces efficiently promote the separation of photogenerated electron-hole pairs. The exposed reaction active sites accelerate electrons consumption. In addition, the cocatalyst Pt is proven to speed up electrons transfer and utilization. As a result, samples of $MAPbI_3$/triple-shelled TiO_2 hollow structure displayed an H_2 evolution rate of 6856.2 μmol h^{-1} g^{-1} under visible light irradiation, which is much faster than that of barely $MAPbI_3$ (268.6 μmol h^{-1} g^{-1}). This work provides a new strategy for loading catalysts inside HoMSs for enhancing photocatalytic hydrogen evolution efficiency.

3.2 Introduction

Hydrogen as clean energy has been extensively studied and used in many fields. When hydrogen is burned, only water is produced. Photocatalytic hydrogen reaction evolution (HER) through the splitting of water,[145-146] hydrohalic acid,[147-149] has attracted more attention. The design route of photocatalysts is mainly corresponding to the photocatalytic processes, including light absorption, charges separation and transfer, and surface photocatalytic reaction.[72] For the light absorption process, the narrow bandgap semiconductors, such as sulfides,[150-151] C_3N_4,[152-155] halide perovskites,[148] have been applied to improve the light-sensitive range. For charges separation and transfer, semiconductors such as metal oxides[35, 156-157], and heterojunctions[158] have been widely used as charges transfer carriers. For the surface photocatalytic reaction, the different dimensional catalysts were designed to expose abundant reaction sites.[59, 66, 69]

Organic-inorganic hybrid perovskites have been demonstrated as wonderful light sensitizers in solar cells,[101, 159-160] light-emitting diodes,[161-162] photocatalysis,[163-165] because of the narrow bandgap. Generally, the organic-inorganic hybrid perovskites are not stable in the water. In 2016, methylammonium lead iodide perovskite ($MAPbI_3$) was applied in $MAPbI_3$ saturated solution for photocatalytic HER.[99] The $MAPbI_3$ in its saturated solution is stable because of dynamic equilibrium. After this stable strategy, the perovskite materials have been widely applied in photocatalytic HER[147-149]. But the generated charges have not been utilized efficiently then the recombination happened. Hence, heterogeneous interfaces were constructed to enhance the utilization efficiency of photogenerated charges.[166-167] For example, the heterogeneous interfaces include $MAPbI_3$/reduced graphene oxide (rGO),[168] perovskite/sulfides,[140, 169] perovskite/metal,[170] Z-scheme heterojunction,[171] perovskite/metal oxide,[172-173] perovskite/metal-organic frameworks (MOFs).[174]

Except for the construction of heterogeneous interfaces, the preparation of hierarchical structures of photocatalysts can also improve photocatalytic solar energy conversion efficiency. HoMSs materials with unique layered shell structures exhibit unique characteristics in improving photocatalytic HER efficiency.[69, 83, 97] The enhancement through special structures of HoMSs mainly corresponds to three steps of the photocatalytic process. In detail, the enhancement of light absorption derives from light scattering and reflections between different multi-shells. The thin shells shorten the transfer distance from materials inside to surface reactive sites. Because of thin shells, many reactive sites are exposed to accelerate the surface reaction. The numerous pores in the shells of HoMSs are contributed to mass transfer then further improve the photocatalytic efficiency. Loading the narrow bandgap semiconductors as light adsorber inside of HoMSs is a new strategy for the application of HoMSs in the photocatalytic field. The multi-shells provide many contact points with light adsorber for fast charges separation and suppressing recombination of electron-hole pairs. The behaviors of light scatting and reflections further improve the light absorption of narrow bandgap semiconductors inside HoMSs.

In this chapter, the Pt/TiO_2 HoMSs and the $MAPbI_3/Pt/TiO_2$ HoMSs composite were applied in photocatalytic HER. As the growth of shells numbers from 1 to 3, the photocatalytic performance increases. The photocatalytic activity of photocatalyst based on triple-shelled composite approach 6856.2 μmol h^{-1} g^{-1}, which is almost 25 times than the pure $Pt/MAPbI_3$. The photocatalysts of Pt/TiO_2 HoMSs and the $MAPbI_3/Pt/TiO_2$ HoMSs present good stability for continuous reaction over 15 hours. Through photo-electric characterizations, the

cocatalyst Pt and TiO_2 HoMSs are contributed to charges separation and transfer. The thin multi-shells in TiO_2 HoMSs not only shorten the transfer distance of electrons but also decrease the electron transfer resistance. The contacts of multi-shells inside TiO_2 HoMSs and perovskite crystals generate an abundant heterogeneous interface for fast electron separation and transfer.

3.3 Experiment Section

3.3.1 Chemicals

Dimethyl formamide (DMF) and dimethyl sulfoxide (DMSO) were bought from Sigma-Aldrich. Lead iodide (PbI_2) (99.99%) and methylamine iodide (MAI) (99.99%) were bought from Xi'an Polymer Light Technology Corp. The sucrose, hydroiodic acid (HI, 55 wt.%), hypophosphite acid (H_3PO_2, 50 wt.% in H_2O), tetrabutylammonium hexafluorophosphate ($TBAPF_6$), and absolute methanol (AR) were purchased from Sinopharm chemical reagent Co., Ltd with analytically grade. All reagents were used without further purification.

3.3.2 Experimental Equipment

Precision electronic balance (Beijing Dolly instrument system Co., Ltd. Model: BS224S), magnetic stirring apparatus (Jiangsu Changzhou guohua electronics Co., Ltd. Model: HJ-4A), drying oven (Tianjin Taisite instrument Co., Ltd. Model: 202-1), ultrasonic cleaner (Kunshan ultrasonic instrument Co., Ltd. Model: K-Q250B), Teflon steel reactor (500 mL), refrigerator (Siemens. Model: KG32NV21EC), Aike lab pure water system (Model: AKSW-V-16), Top-illuminated quartz reaction system (Labsolar-6A, Beijing Perfectlight Technology Co., Ltd.), Xe-lamp (300 W, Beijing Perfectlight Technology Co., Ltd.), gas chromatograph (Tianmei Technology, GC-7900).

3.3.3 Methods

3.3.3.1 Synthesis of Pt/$MAPbI_3$/TiO_2 HoMSs

The $MAPbI_3$/TiO_2 HoMSs was synthesized firstly by the impregnation method. First, 35 mg of TiO_2 HoMSs were put into a bottle, and then the gases in the inside TiO_2 HoMSs were drawn out in a vacuum system. Then, 50 μL 1.2 mlo/L perovskite precursor solution was dropped rapidly, and the bottle was kept quiescence at room temperature for 24 hours. Next, the 20 μL mixed solvent of DMF and DMSO (4:1 by volume) was placed around the above mixture. Finally, the bottle was heated to 70 °C and held for 5 hours.

Then, a 50 mg was dispersed into 20 mL $MAPbI_3$ saturated solution which contains 75 uL $H_2PtCl_6 \cdot 6H_2O$. The reaction system was vacuumed and filled with Ar gas three times. The temperature of the reaction system was kept at a constant (15 °C). Then, the reaction system was illuminated under a 300 W Xe lamp (Ushio-CERMAXLX 300). After reaction for 3 hours, the products of $Pt/MAPbI_3/TiO_2$ HoMSs were centrifuged, washed with a saturated solution, and finally dried at 50 °C for 6 hours in a vacuum oven.

3.3.3.2 Mixture of $MAPbI_3$ and $Pt/3S\text{-}TiO_2$ HoMSs

The $MAPbI_3$ materials and $Pt/3S\text{-}TiO_2$ HoMSs are obtained from chapter 2. The mixture is composed of 17.5 mg $MAPbI_3$ and 17.5 mg $Pt/3S\text{-}TiO_2$ HoMSs. The mass fraction of $MAPbI_3$ in the mixture was around 50 %. The mixture was well ground by using the agate mortar under a nitrogen atmosphere.

3.3.3.3 Preparation of $MAPbI_3$ Saturated Solution

First, the HI solution and H_3PO_2 solution are mixed in a volume ratio of 4 to 1. After the mixed solution turning to colorless, 1.027 g MAI and 2.97 g PbI_2 were put into 10 ml of the mixed solution. The mixed solution was removed from the air and filled with Ar gas three times to avoid oxidization of the HI solution. Then, the suspension was placed at 90 °C water bath with continuous stirring under dark and Ar atmosphere. After three hours, the suspension was placed at 15 °C water bath over 3 hours. Separating liquid from solids, the $MAPbI_3$ saturated solution was obtained.

3.3.3.4 Photocatalytic H_2 Evolution in Deionized Water

The evaluation of photocatalytic HER performance was carried out through two parts, continuous gas collection system, and a sample analysis system. A certain amount of photocatalyst Pt/TiO_2 was placed on 20 mL mixed solution of deionized water and absolute methanol (volume ratio equals 3:1). Then the suspension was dispersed under ultrasonic equipment. Next, the suspension was put into Labsolar-6A gas collection system and kept the temperature in a constant at 8 °C. The gas collection system was vacuumed. The Xe-lamp was used as a sunlight simulator with a full spectrum (light intensity, 0.15 $W \cdot cm^{-2}$). The obtained gas was analyzed by a gas chromatograph.

3.3.3.5 Photocatalytic H_2 evolution in HI solution

Before the photocatalytic test, the photocatalysts were stored in 15 °C environment. Then, a certain amount of photocatalyst was put in 10 mL $MAPbI_3$ saturated solution under

continuous stirring. The reaction temperature was maintained at 15 °C by a circulation cooling water. The reaction system was pumping vacuum and refilling the Ar gas three times to eliminate oxygen before the test. The Xe-lamp was used as a sunlight simulator with a 420 nm cut-off filter (light intensity, 0.15 $W \cdot cm^{-2}$). The volume of evolved hydrogen was measured by a gas chromatograph (Tianmei Technology, GC-7900).

3.3.4 Characterizations

The electrochemical impedance spectroscopy (EIS), Mott-Schottky curves, and transient photocurrent response curves were performed on the electrochemical workstation (CH Instruments Ins.) in a three-electrode configuration with the assembled photoelectrodes (photocatalysts on FTO glass) as the working electrode, the Ag/AgCl as the reference electrode and the Pt slice as the counter electrode, and 0.1M Na_2SO_4 solution was used as electrolyte. When testing the photo-electric properties of photocatalysts containing $MAPbI_3$, the methylene dichloride containing 0.1 M tetrabutylammonium hexafluorophosphate ($TBAPF_6$) was used as an electrolyte. For time-resolved photo-current behaviors, a 300 W Xe lamp (FX-300, Beijing Perfect light Technology Co. Ltd.). Photoluminescence (PL) spectra were scanned on a photoluminescence spectrometer (NanoLOG-TCSPC, HORIBA JOBIN YVON). The PL decay spectra were fitted by $\tau_{ave}=B_1e^{(-t/\tau1)}+B_2e^{(-t/\tau2)}+B_3e^{(-t/\tau3)}$.

3.4 Results and Discussions

3.4.1 HER Performance of Pt/TiO_2 HoMSs

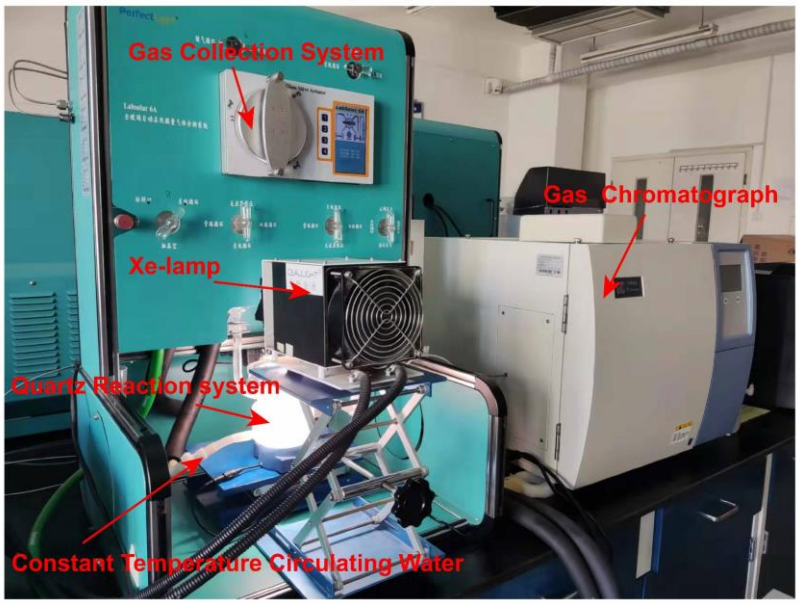

Figure 3.1 The top-illuminated quartz photocatalytic HER system and gas chromatograph.

The HER performance was measured by the top-illuminated quartz photocatalytic HER system (Labsolar-6A, Beijing Perfectlight Technology Co., Ltd.) and gas chromatograph (Tianmei Technology, GC-7900) as shown in figure 3.1. The photocatalysts were put in the quartz reaction system and illuminated under Xe-lamp. The reaction system was kept at a constant temperature by circulating water. Generated H_2 was collected by a gas collection system and then measured by a gas chromatograph. The collected H_2 was tested at an interval of 30 minutes.

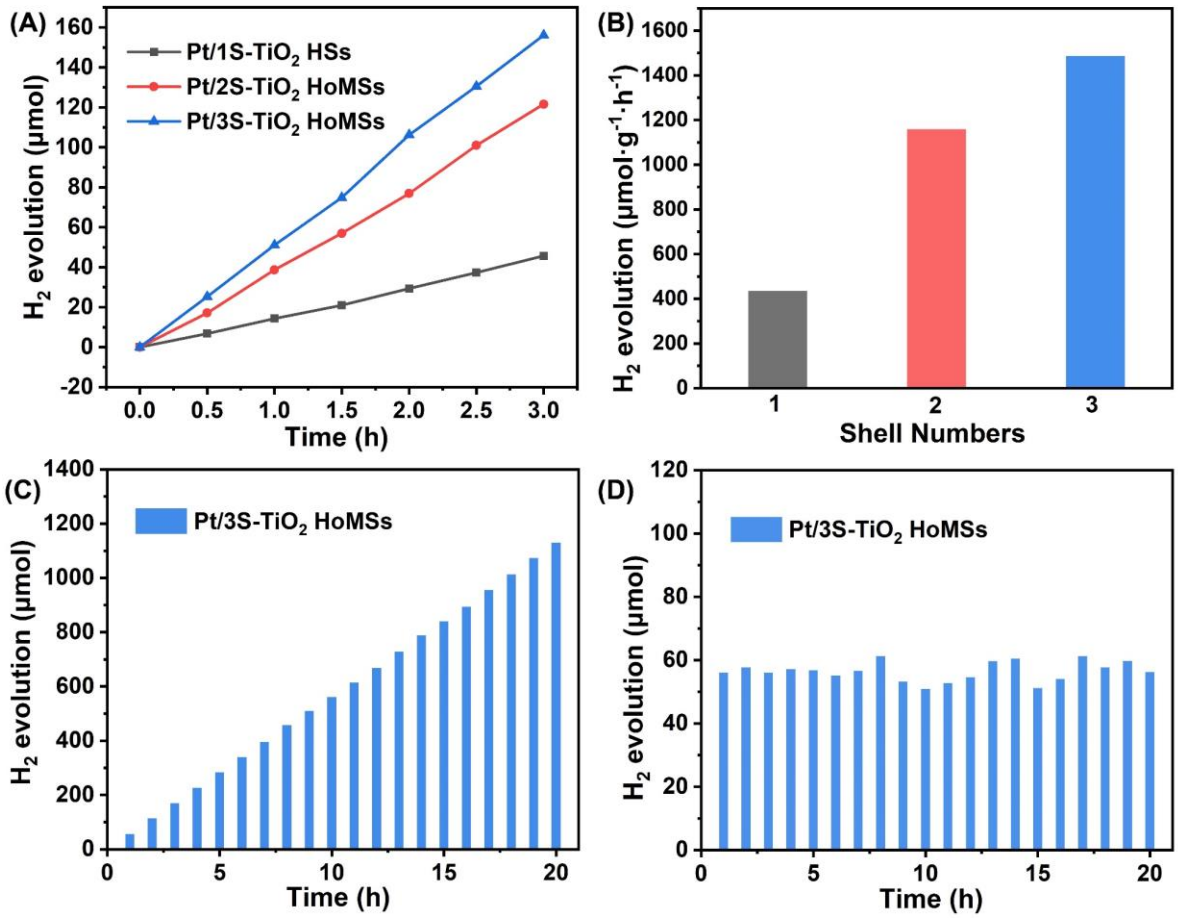

Figure 3.2 Photocatalytic HER performance of Pt/TiO_2 HoMSs under full spectrum: (A) HER performance of Pt/TiO_2 HoMSs with different shells; (B) Normalized HER performance; (C) Long-term stability of Pt/3S-TiO_2 HoMSs; (D) H_2 evolution of Pt/3S-TiO_2 HoMSs in an individual hour.

The photocatalytic HER performance of Pt/TiO_2 HoMSs was tested under full spectrum as shown in figure 3.2. The HER performance of Pt/TiO_2 HoMSs with different shells in figure 3.2A shows the performance order: Pt/1S-TiO_2 HSs (45.7 μmol) < Pt/2S-TiO_2 HoMSs (121.6 μmol) < Pt/3S-TiO_2 HoMSs (156.1 μmol). And the corresponding unit mass HER

performances in figure 3.2B are Pt/1S-TiO_2 HSs (435.3 μmol·g^{-1}·h^{-1}), Pt/2S-TiO_2 HoMSs (1158.4 μmol·g^{-1}·h^{-1}) and Pt/3S-TiO_2 HoMSs (1486.9 μmol·g^{-1}·h^{-1}), respectively. To verify the long-term stability, HER measurement of Pt/3S-TiO_2 HoMSs was continuously carried out for 20 hours under full spectrum illumination as shown in figure 3.2C and figure 3.2D. It displayed that 1129.2 μmol of H_2 is continuously produced by Pt/3S-TiO_2 HoMSs in 20 hours. The H_2 evolution of Pt/3S-TiO_2 HoMSs in an individual hour in figure 3.2D is around 55 μmol. The H_2 production of the whole process was remaining growth in an approximate increment. This result proves that Pt/3S-TiO_2 HoMSs presents wonderful stability in HER.

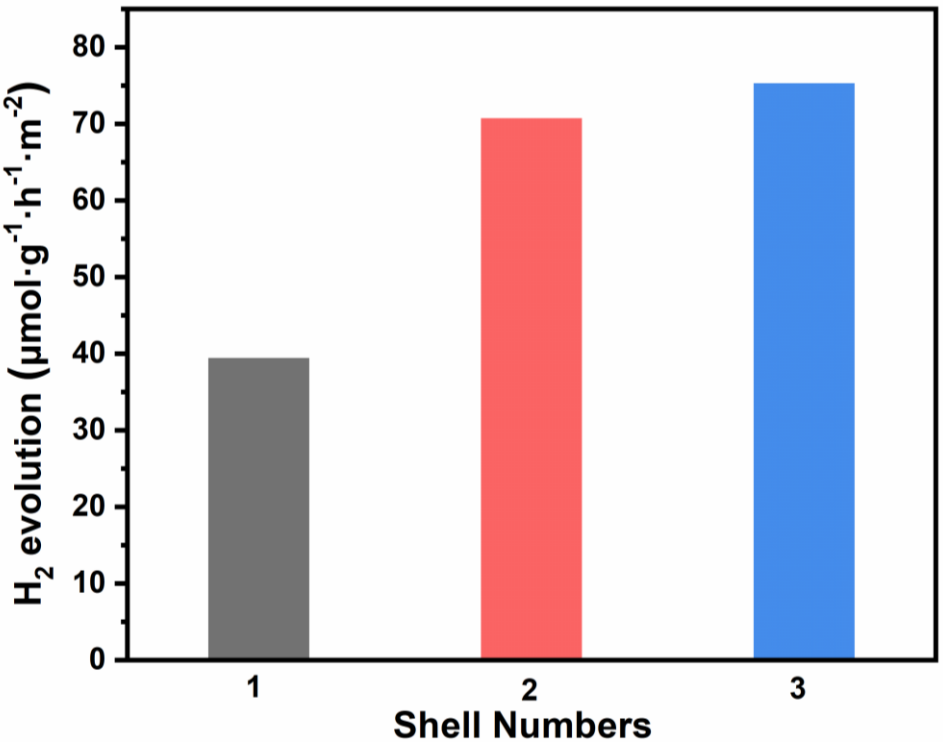

Figure 3.3 Photocatalytic HER performance of Pt/TiO_2 HoMSs under full spectrum in the unit area.

To survey whether specific surface area affects performance, the photocatalytic HER performance of Pt/TiO_2 HoMSs in the unit area was calculated (performance = H_2 evolution per hour / specific surface area) as shown in figure 3.3. The Normalized HER performance of Pt/3S-TiO_2 HoMSs is 75.3 μmol·g^{-1}·h^{-1}·m^{-2} which is higher than Pt/2S-TiO_2 HoMSs (70.7 μmol·g^{-1}·h^{-1}·m^{-2}) and Pt/1S-TiO_2 HSs (39.4 μmol·g^{-1}·h^{-1}·m^{-2}). Generally, the higher specific surface with more reaction activity sites presents higher photocatalytic activity. After calculated HER performance, the photocatalytic performance of Pt/TiO_2 HoMSs shows different. The difference between different shells is possibly derived from the advantages of

HoMSs, such as the light absorption and electron transfer resistance.

3.4.2 HER Performance of $MAPbI_3/Pt/TiO_2$ HoMSs

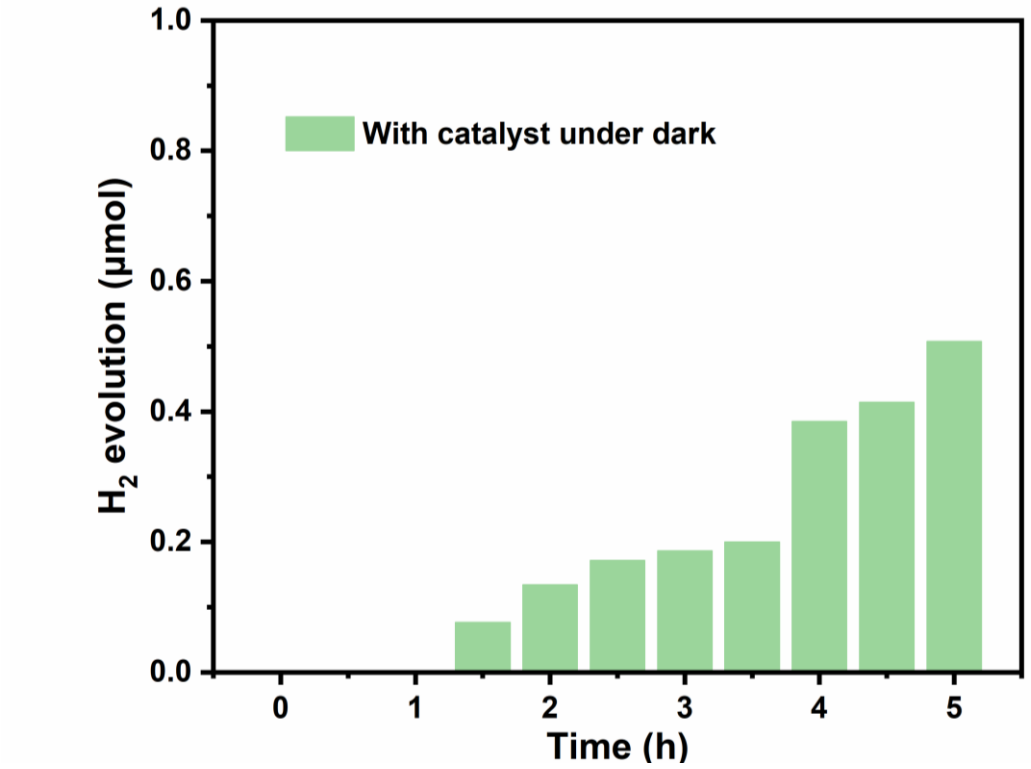

Figure 3.4 The HER performance of $MAPbI_3/Pt/3S\text{-}TiO_2$ HoMSs under dark condition.

Organic-inorganic halide perovskite materials are not stable in the aqueous solution system. In this chapter, the saturated $MAPbI_3$ in the mixed solution (8 mL HI and 2 mL H_3PO_2 were mixed at a 4:1 volume ratio) is used. In the $MAPbI_3$ saturated solution, dynamic equilibrium is realized between $MAPbI_3$ crystals and ions. The persistent dissolution and deposition of $MAPbI_3$ phase is dynamic stable at certain I^- and H^+ concentrations.[99] Hence, the $MAPbI_3$ can be used as a photocatalyst to evolve hydrogen in the saturated $MAPbI_3$ solution. To investigate the HER performance of photocatalyst under dark, the mix saturated solution with $MAPbI_3/Pt/3S\text{-}TiO_2$ HoMSs was measured as shown in figure 3.4. In the first hour, there is no signal of hydrogen because of too low the concentration of H_2 to detect possibly. In the next few hours, the yield is not stable, and only 0.5 μmol H_2 is generated after 5 hours. The $MAPbI_3$ crystal with a non-centrosymmetric polarized structure is contributed to the piezoelectric effect.[175] In the external mechanical force, a built-in electric field of perovskite improve the effective separation of charges. Hence, the mechanical stretch from stirring is possibly contributed to trace H_2 generation.

The photocatalytic performance of photocatalysts containing $MAPbI_3$ was performed under

visible light ($\lambda \geq 420$ nm). Before data collection, the photocatalytic HER system was continuously stirred until homogeneous dispersion of photocatalyst. To find an appropriate proportion of $MAPbI_3$ and 3S-TiO_2 HoMSs, the different mass fractions of $MAPbI_3$ in composites were synthesized by turning the concentration of $MAPbI_3$ precursor. And accurate mass fractions were confirmed by ICP results as shown in table 3.1. The photocatalytic HER performance is shown in figure 3.5. After reaction 3 hours, the H_2 evolution for $MAPbI_3$/Pt/3S-TiO_2 HoMSs with 50.03 wt.% $MAPbI_3$ is 719.9 μmol, which is the highest production among mass fractions in 33.03 wt.% (280.4 μmol), 42.57 wt.% (448.8 μmol), and 54.89 wt.% (489.5 μmol). Because the performance of 50.03 wt.% $MAPbI_3$ in $MAPbI_3$/Pt/3S-TiO_2 HoMSs is the highest, the following composite photocatalysts are kept at this mass fraction.

Table 3.1 The mass fraction of $MAPbI_3$ measured by ICP.

Sample	Dissolving mass (mg)	Dilution ratio	C (Pb^{2+})	Mass fraction of $MAPbI_3$ (wt. %)
Pt/3S-TiO_2 HoMSs with 0.6 M precursor	24.4	×1000	0.22675	33.20
Pt/3S-TiO_2 HoMSs with 0.9 M precursor	24.2	×1000	0.3125	43.02
Pt/3S-TiO_2 HoMSs with 1.2 M precursor	24.9	×1000	0.39175	50.39
Pt/3S-TiO_2 HoMSs with 1.5 M precursor	24.2	×1000	0.42575	55.64
Pt/1S-TiO_2 HSs with 1.2 M precursor	23.9	×1000	0.36175	49.17
Pt/2S-TiO_2 HoMSs with 1.2 M precursor	24.1	×1000	0.363	48.85
Pt/P25 with 1.2 M precursor	24.6	×1000	0.384	50.17

To study the effects of the photocatalyst's structure on photocatalytic performance, the photocatalysts with single shell, double shells, and triple shells were measured under the same conditions as shown in figure 3.6. As the shell numbers increase from 1 to 3, the photocatalytic activities of $MAPbI_3$/Pt/TiO_2 HoMSs increase from 2696.2 μmol $h^{-1}g^{-1}$ ($MAPbI_3$/Pt/1S-TiO_2 HSs) to 6856.2 μmol h^{-1} g^{-1} ($MAPbI_3$/Pt/3S-TiO_2 HoMSs). But the performance of the mixture of $MAPbI_3$ and Pt/3S-TiO_2 HoMSs is only 1830.7 μmol h^{-1} g^{-1} which is lower than synthesized composites. Photocatalysts with multiple shells improve incident light reflections and scattering. The multi-shelled structures enhance the probability of light absorption and improve the light-harvesting capability. More shells will provide a larger available surface for building heterogeneous interfaces and reactive sites to promote the surface photocatalytic reaction.[35, 69, 72, 97] Besides, the photocatalytic performance of

Pt/$MAPbI_3$ is a quite lower photocatalytic activity in 268.6 μmol h^{-1} g^{-1} when compared with $MAPbI_3$/Pt/TiO_2 HoMSs. According to the above results, a conjecture is put forward. The $MAPbI_3$/TiO_2 heterogeneous interface contributes to improving the charges extraction from $MAPbI_3$.

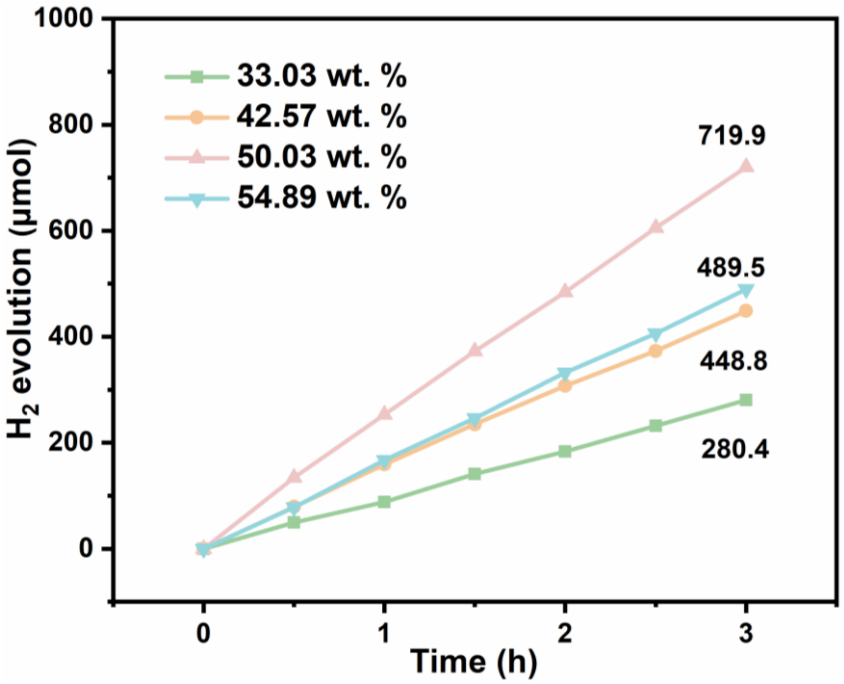

Figure 3.5 Photocatalytic HER performance of $MAPbI_3$/Pt/3S-TiO_2 HoMSs in different mass fractions of $MAPbI_3$ in $MAPbI_3$/Pt/3S-TiO_2 HoMSs under visible-light ($\lambda \geq 420$ nm). The mass of catalysts used in the test is 35 mg.

In contrast, the H_2 evolution of Pt/3S-TiO_2 HoMSs is no single after three hours under visible-light irradiation. The phenomenon is reasonable because the bandgap of without doped TiO_2 materials generally focuses on 3.0~3.2 eV. The corresponding absorption range of wavelength is below 420 nm which is in the ultraviolet part of the full spectrum. Compared with $MAPbI_3$/Pt/3S-TiO_2 HoMSs, the $MAPbI_3$/3S-TiO_2 HoMSs composite generates only 3.7 μmol h^{-1} g^{-1} at the consistent test conditions. Without Pt cocatalysts, the utilization of photogenerated electrons is extremely limited. The Pt cocatalyst plays an important role in reaction centers of H_2 reduction.

The HI splitting efficiency is an evaluation indicator of the photocatalytic activity of photocatalysts. The visible-light driven HI splitting efficiency was obtained from the following formula:[168, 176]

$$\text{Solar HI splitting efficiency} = \frac{2\text{N}_{\text{H}_2} \times E \times 1.6 \times 10^{-19}}{P_{\text{sol}}(\text{W}\cdot\text{cm}^{-2}) \times A(\text{cm}^2) \times t(\text{s})} \times 100\% \quad 3.1$$

$$= \frac{2 \times \text{Evolved } H_2(\text{mol}) \times N_A \times E(\text{HI solution splitting}) \times 1.6 \times 10^{-19}}{P_{\text{sol}}(\text{W}\cdot\text{cm}^{-2}) \times A(\text{cm}^2) \times t(\text{s})} \times 100\%$$

where N_A presents the Avogadro constant (6.02×10^{23}), P_{sol} presents the light intensity (0.15 $\text{W}\cdot\text{cm}^{-2}$), A is the area of the light source (28.26 cm^2), and t is the reaction time. The total potential solar HI splitting efficiency is adopted as the reported literature.[99] The total potential of HI splitting E (HI solution splitting) = $E(3I^- \rightarrow 2e^- + I_3^-)$-$E(2H^+ + 2e^- \rightarrow H_2)$ = 0.333 V. The solar HI splitting efficiencies of different catalysts under visible illumination was calculated as shown in table 3.2. The solar HI splitting efficiency of photocatalysts obeys following order: $MAPbI_3$/Pt/3S-TiO_2 HoMSs (2.88 %) > $MAPbI_3$/Pt/2S-TiO_2 HoMSs (1.53 %) > $MAPbI_3$/Pt/1S-TiO_2 HSs (0.72) > $MAPbI_3$/Pt (0.07 %). This order of the result is consistent with HER performance results. The multi-shelled structures indeed improve the activity of the photocatalyst.

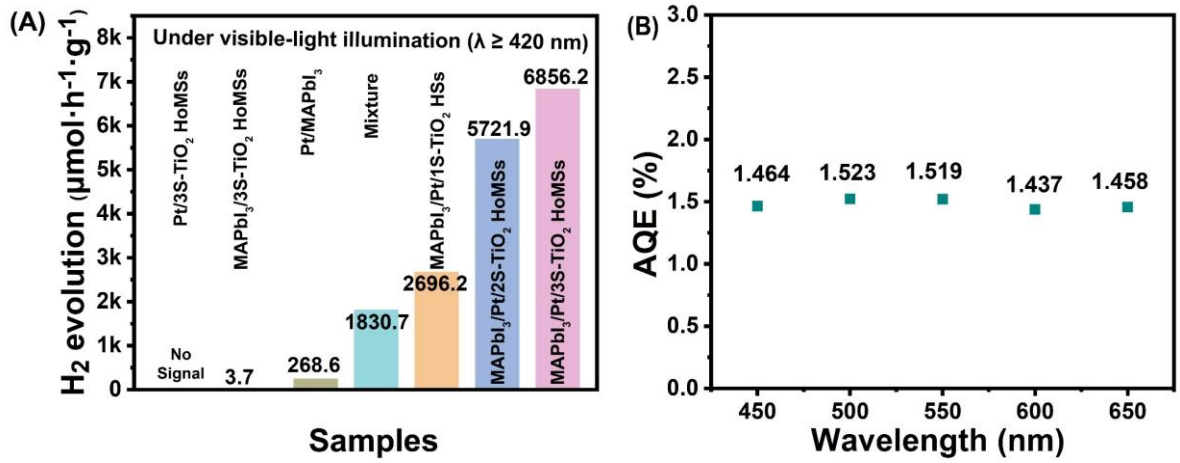

Figure 3.6 (A) Photocatalytic HER performance of different catalysts under visible-light ($\lambda \geq 420$ nm). The mixture is mixed of $MAPbI_3$ and Pt/3S-TiO_2 HoMSs The mass of catalysts used in the test is 35 mg; (B) AQE of $MAPbI_3$/Pt/3S-TiO_2 HoMSs measured at light filters with different wavelengths.

To study the visible light response under different light wavelengths, the apparent quantum efficiency (AQE) was carried out on a Xe lamp (300 W) with different filters of monochromatic light, including 450 nm, 500 nm, 550 nm, 600 nm, and 650 nm. In this chapter, the AQE is calculated by the ratio of the electron consumption number ($N_{electron}$) in the photocatalytic process to the photons flux per hour (N_{photon}) under a specialized wavelength range, which is illustrated in the followed equations:[7]

$$AQE\ (\%) = \frac{N_{electron}}{N_{photon}} \times 100\% = \frac{2N(H_2)}{N_{photon}} \times 100\% \quad 3.2$$

$$N_{photon} = \frac{Light\ intensity \times Illumination\ area \times time}{E_{photon}} \quad 3.3$$

The calculation of $N_{electron}$ comes from a rule that producing one molecule of hydrogen needs two electrons, according to the equations mentioned in chapter 1. The N_{photon} is calculated by using the formula, where the illumination area is 3.61 cm^2, and E_{photon} is the average single photon energy. E_{photon} can be calculated by the following equation:

$$E_{photon} = \frac{hc}{\lambda} \quad 3.4$$

where h presents the Planck constant, λ presents the light wavelength, and c is the speed of light. Meanwhile, the AQE of $MAPbI_3$/Pt/3S-TiO_2 HoMSs was plotted as shown in figure 3.6B. The AQE of $MAPbI_3$/Pt/3S-TiO_2 HoMSs under from 450 nm to 650 nm is around 1.437 % to 1.523 %, which indicates the $MAPbI_3$ introduced in Pt/3S-TiO_2 HoMSs broaden the response scope of light wavelength.

Table 3.2 The solar HI splitting efficiency of different catalysts under visible illumination.

Sample	Solar HI splitting efficiency (%)
$MAPbI_3$/Pt	0.07
$MAPbI_3$/Pt/1S-TiO_2 HSs	0.72
$MAPbI_3$/Pt/2S-TiO_2 HoMSs	1.53
$MAPbI_3$/Pt/3S-TiO_2 HoMSs	2.88

Long-term stability is one of the evaluation indicators of photocatalysts. To investigate the long-term stability of $MAPbI_3$/Pt/3S-TiO_2 HoMSs, the experiment was performed under visible-light illumination with a light filter $\lambda \geq 420$ nm. The result of long-term stability is shown in figure 3.7. After 30 hours of continuous light irradiation, 10652.4 μmol of H_2 is produced by the $MAPbI_3$/Pt/3S-TiO_2 HoMSs. The H_2 production of the whole process is remaining growing in different increments. In the first 15 hours, the H_2 evolution rate almost keeps a constant. After 15 hours, the H_2 evolution increment per hour is slightly decreased. To study changes in increments, the increment per hour was calculated as shown in figure 3.7B. In the first 15 hours, the H_2 evolution increment is around 400 μmol. The individual high points and low points may be caused by unevenly mixing of gas in the reaction system

before tests. In the range from 16 hours to 25 hours, the H_2 evolution increment was around 340 μmol. In the last five hours, the H_2 evolution increment was around 250 μmol. Even if the increment decreases gradually, the $MAPbI_3$/Pt/3S-TiO_2 HoMSs still have good catalytic activity.

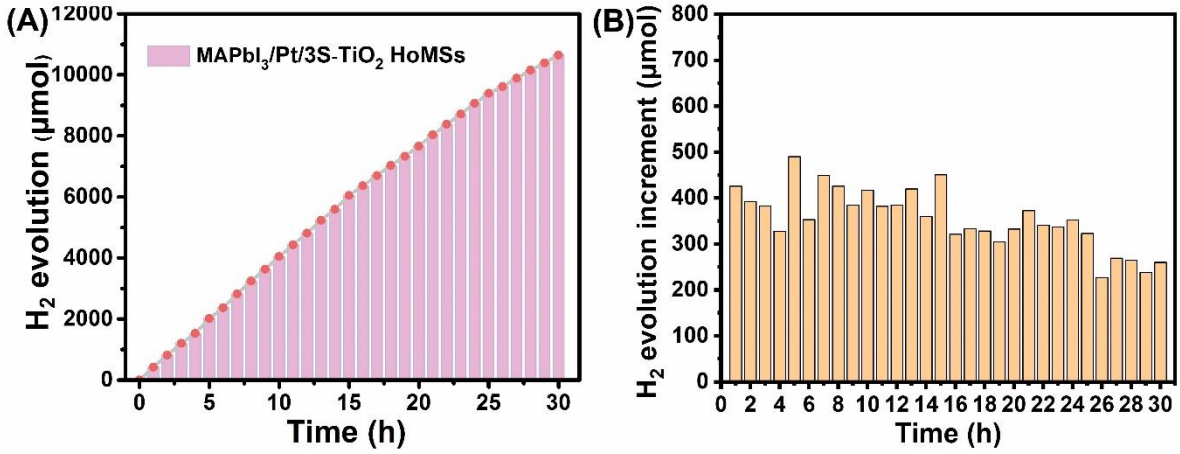

Figure 3.7 (A) Long-term stability test of the $MAPbI_3$/Pt/3S-TiO_2 HoMSs; (B) The corresponding H_2 evolution per hour; The mass of catalysts used in the test is 55 mg.

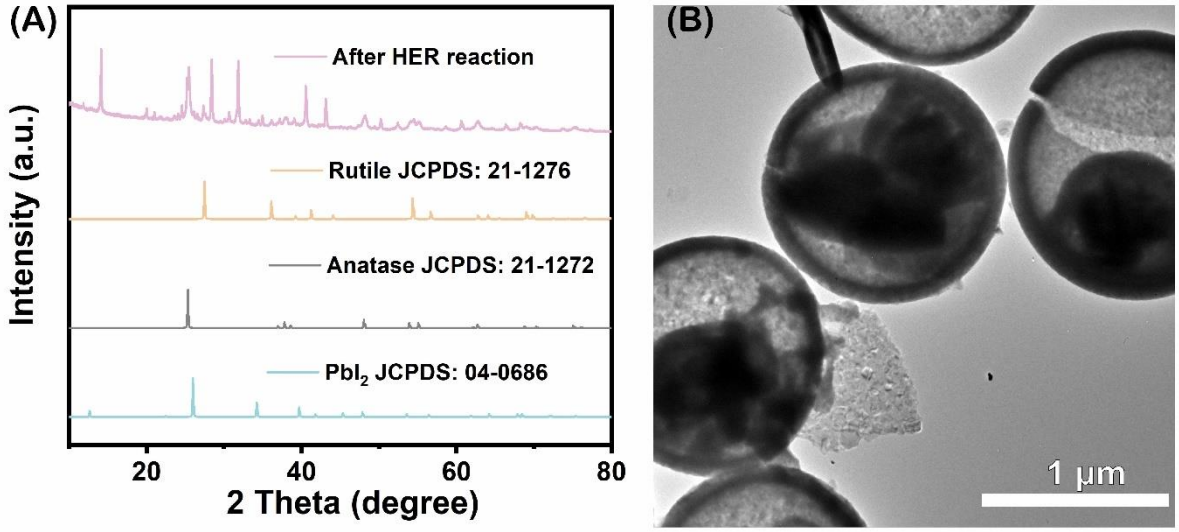

Figure 3.8 (A) XRD patterns of $MAPbI_3$/Pt/3S-TiO_2 HoMSs after HER test; (B) TEM image of $MAPbI_3$/Pt/3S-TiO_2 HoMSs after HER test.

After HER test, the sample was fast centrifugated and the sample was drying at 15 °C for 48 hours. The composition and morphology of $MAPbI_3$/Pt/3S-TiO_2 HoMSs after HER test were investigated by using XRD and TEM as shown in figure 3.8. After HER test, The XRD result reveals that $MAPbI_3$/Pt/3S-TiO_2 HoMSs maintain the phase structure when compared with XRD patterns of $MAPbI_3$ in figure 3.3. The diffraction characteristic peaks of $MAPbI_3$ and

TiO_2 have no difference except for the diffraction peak intensity of $MAPbI_3$. The TEM results in figure 3.8B indicate that the $MAPbI_3$ still exists inside 3S-TiO_2 HoMSs. Hence, the XRD and TEM results reveal that $MAPbI_3$/Pt/3S-TiO_2 HoMSs maintain the phase structure and morphology structure after the long-term test. Besides, the $MAPbI_3$ materials were put into $MAPbI_3$ saturated solution (HI:H_3PO_2=4:1 in volume) as shown in figure 3.9. Comparing the pictures taken at 0 hours to 96 hours, the $MAPbI_3$ exists stably in a saturated solution.

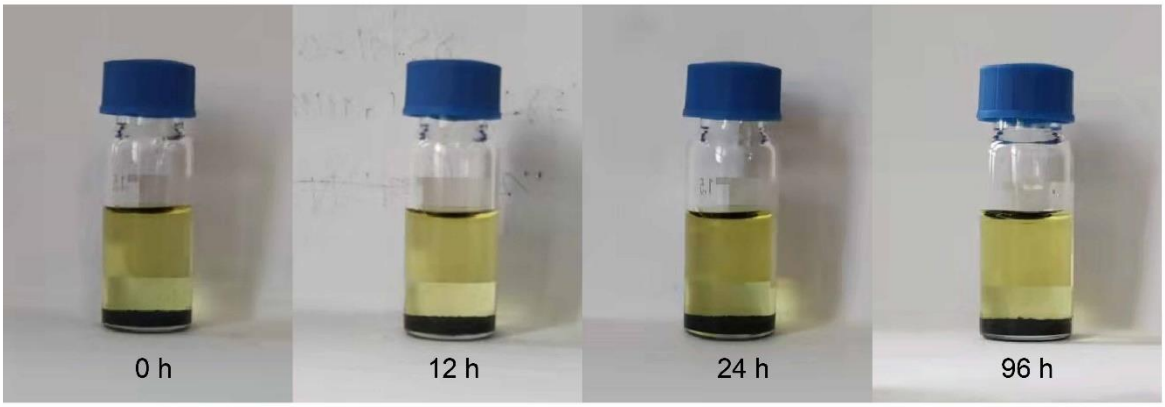

Figure 3.9 $MAPbI_3$ materials stored in saturated solution (HI:H_3PO_2=4:1 in volume) for different times.

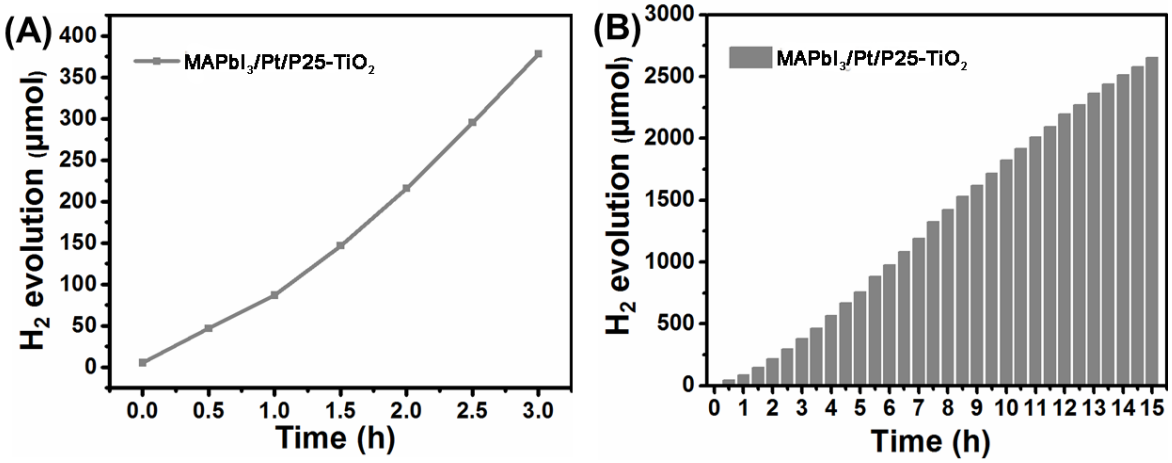

Figure 3.10 Photocatalytic HER performance of $MAPbI_3$/Pt/P25-TiO_2 under visible-light illumination ($\lambda \geq 420$ nm). (A) HER activity for $MAPbI_3$/Pt/P25-TiO_2 is 3602.8 μmol/h/g; (B) The Long-term stability test of $MAPbI_3$/Pt/P25-TiO_2. The mass of catalysts used in the test is 35 mg.

To compare other morphologies of titanium oxide, nano-particles P25-TiO_2 were applied to synthesize $MAPbI_3$/Pt/P25-TiO_2 for photocatalytic HER. The HER activity and the long-term stability are shown in figure 3.10. The HER activity of $MAPbI_3$/Pt/P25-TiO_2 is 378.2 μmol after three hours (3602.8 μmol h^{-1} g^{-1}) which is much lower than the performance of

$MAPbI_3$/Pt/3S-TiO_2 HoMSs. The great enhancement in HER activity of $MAPbI_3$/Pt/3S-TiO_2 HoMSs is attributed to the unique structural features of HoMSs. The long-term stability of $MAPbI_3$/Pt/P25-TiO_2 is lower than $MAPbI_3$/Pt/3S-TiO_2 HoMSs in the first 15 hours. The perovskite inside HoMSs may form a local high concentration which is contributed to the dynamic equilibrium of $MAPbI_3$. But in this reaction, the $MAPbI_3$/Pt/P25-TiO_2 are possibly decomposed to $MAPbI_3$ and Pt/P25-TiO_2, suggesting the hydrogen evolution rate may not stable.

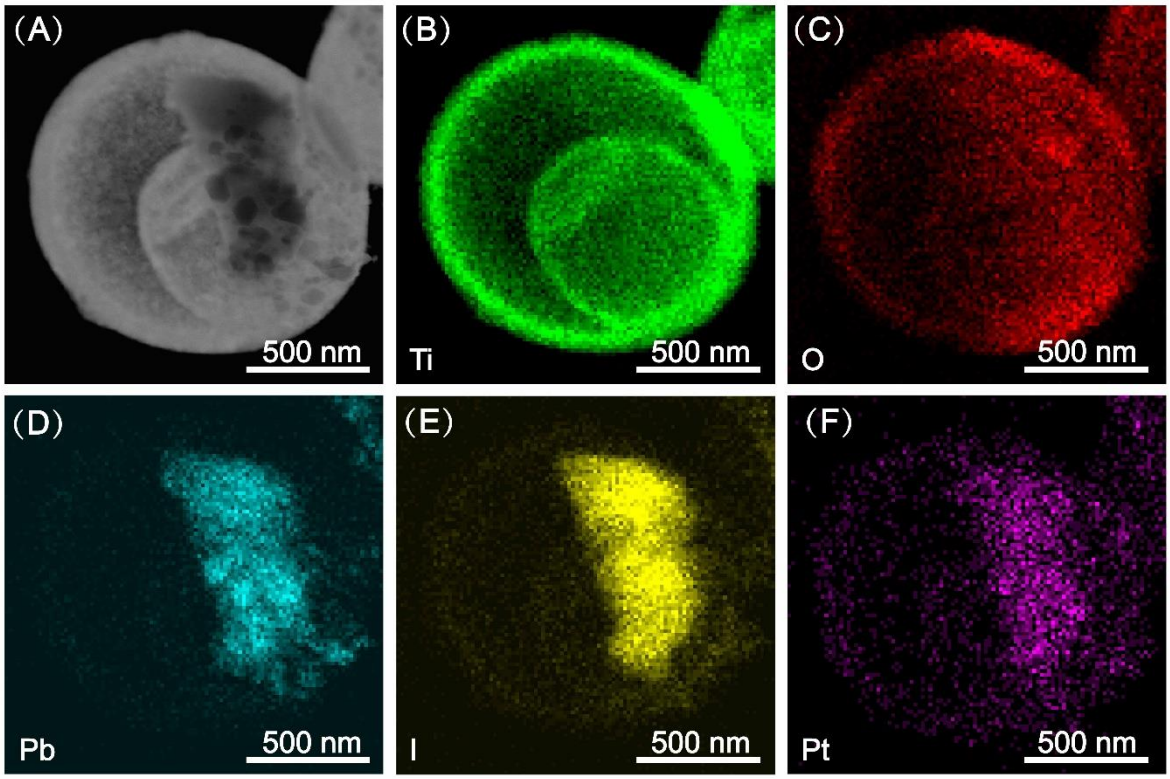

Figure 3.11 (A) HAADF-STEM image of Pt/$MAPbI_3$/3S-TiO_2 HoMSs; The Elemental mappings images of $MAPbI_3$/Pt/3S-TiO_2 HoMSs: (B) Ti (green), (C) O (red), (D) Pb (blue), (E) I (yellow), (F) Pt (purple).

To compare the effect of Pt on electron transfer process, Pt cocatalyst was mainly loaded on $MAPbI_3$ crystal. The location of Pt cocatalyst on $MAPbI_3$ is designed to let photogenerated electrons transfer to Pt and TiO_2 HoMSs. The photocatalyst of Pt on $MAPbI_3$ and TiO_2 was synthesized by the following steps. $MAPbI_3$ was firstly filled into 3S-TiO_2 HoMSs to form $MAPbI_3$/3S-TiO_2 HoMSs and then they were loaded with Pt in the perovskite saturated mix solution of HI and H_3PO_2 (named as Pt/$MAPbI_3$/3S-TiO_2 HoMSs to distinguish with $MAPbI_3$/Pt/3S-TiO_2 HoMSs). To load Pt cocatalyst on $MAPbI_3$/3S-TiO_2 HoMSs successfully, all the synthetic conditions were consistent with before except for the different experimental

sequence and reaction medium. The obtained sample was characterized by HAADF-STEM as shown in figure 3.11. The Ti and O are corresponding to TiO_2 characteristic element. The Pb and I in inside of HoMSs are corresponding to $MAPbI_3$ characteristic element. By comparing with Ti position and Pb position, the Pt is distributed on both $MAPbI_3$ and TiO_2. But the Pt is mainly loaded on $MAPbI_3$ because of the brighter color.

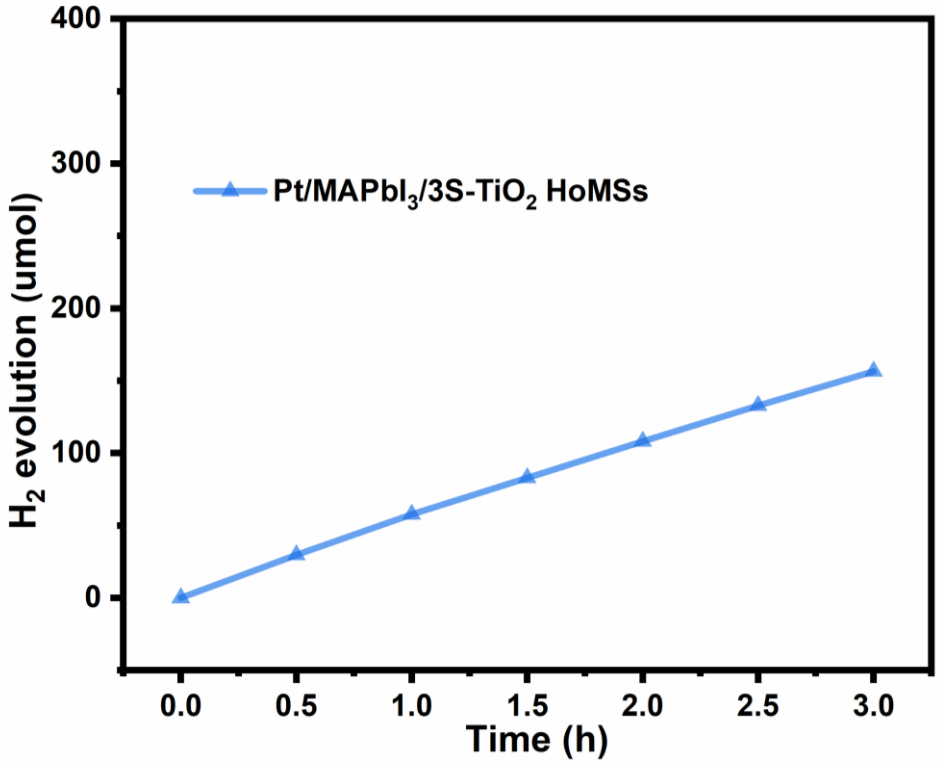

Figure 3.12 Photocatalytic HER performance of $Pt/MAPbI_3/3S\text{-}TiO_2$ HoMSs under visible-light illumination ($\lambda \geq 420$ nm) with H_2 production rate of 1490.5 μmol/h/g. The mass of catalysts used in the test is 35 mg.

The corresponding HER test was carried out on the same condition as before as shown in figure 3.12. The photocatalytic activity of $Pt/MAPbI_3/3S\text{-}TiO_2$ HoMSs is 1490.5 μmol h^{-1} g^{-1}, which is below the photocatalytic activity of $MAPbI_3/Pt/3S\text{-}TiO_2$ HoMSs (6856.2 μmol h^{-1} g^{-1}). This result is possibly caused by different transfer pathways of electrons. When Pt is loaded on TiO_2 HoMSs, the electrons generated from $MAPbI_3$ are transferred into TiO_2 HoMSs and then transfer into Pt clusters for hydrogen reduction. But when Pt is mainly loaded on $MAPbI_3$, the electrons are firstly transferred into Pt on the surface of $MAPbI_3$. The photocatalytic activities of Pt loaded on different positions indicate that the photogenerated electrons in $MAPbI_3$ are preferred to be extracted by TiO_2 and then utilized for photocatalytic HER on Pt co-catalyst surface.

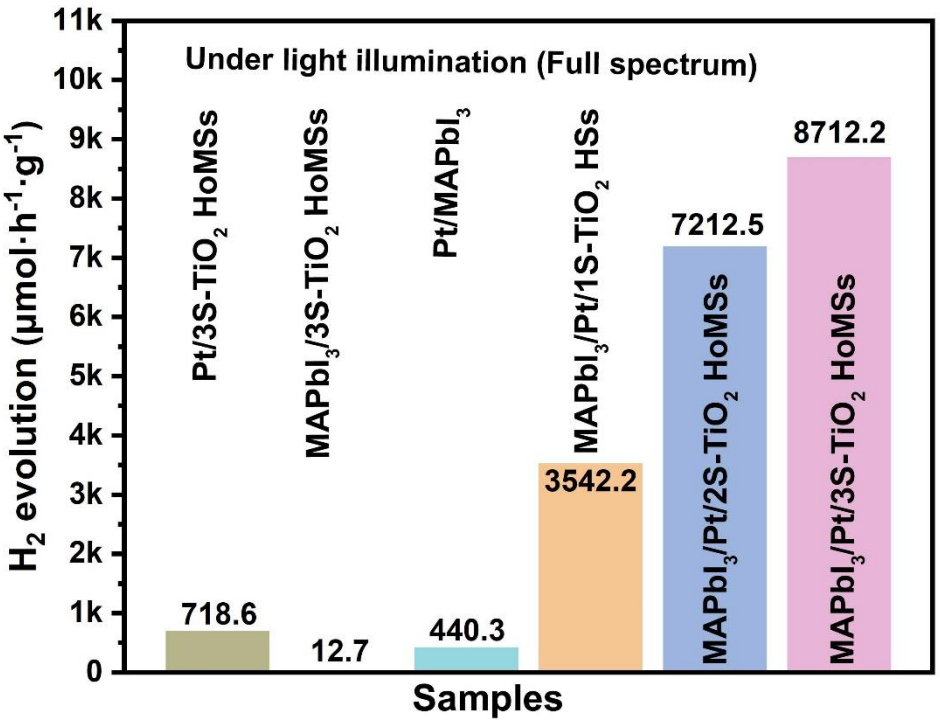

Figure 3.13 Photocatalytic HER performance under full spectrum illumination of different catalysts, Pt/3S-TiO_2 HoMSs, Pt/$MAPbI_3$, and $MAPbI_3$/Pt/1S-TiO_2 HSs, $MAPbI_3$/Pt/ 2S-TiO_2 HoMSs, $MAPbI_3$/Pt/3S-TiO_2 HoMSs. The mass of catalysts used in the test is around 35 mg and HER performance is the average value of reacting in 3 hours.

Table 3.3 the ICP results of Pt for Pt/TiO_2 HoMSs.

Sample	Dissolving mass of catalysts (mg)	Dilution ratio (1:50 in volume)	Concentration of Pt (mg/L)	Mass fraction of Pt (%)
Pt/1S-TiO_2 HSs	9.8	50	2.11	1.076
Pt/2S-TiO_2 HoMSs	9.6	50	1.88	0.979
Pt/3S-TiO_2 HoMSs	10.1	50	2.06	1.020
Pt/P25 TiO_2	9.6	50	1.91	0.995

To investigate the photocatalytic activity in ultraviolet, the photocatalytic HER test under full spectrum illumination for different catalysts was also carried out as shown in figure 3.13. Compared with HER activity in visible light, the H_2 evolution of Pt/TiO_2 HoMSs is 718.6 μmol h^{-1} g^{-1} in full spectrum illumination. The HER activity of Pt/$MAPbI_3$ is also promoted in the full spectrum illumination. The photocatalysts of $MAPbI_3$/Pt/TiO_2 HoMSs present better HER activity in full spectrum illumination when comparing with activity in visible light illumination. Owing to the sensitivity ability of $MAPbI_3$ and TiO_2 HoMSs in the

ultraviolet, the $MAPbI_3$/Pt/3S-TiO_2 HoMSs show the best HER activity (8712.2 μmol h^{-1} g^{-1}) among all samples. To exclude the influence of the amount of Pt cocatalyst on performance, the ICP tests were carried out. The Pt/TiO_2 HoMSs materials were dissolved in the 1 mL mix solution of hydrofluoric acid and nitrohydrochloric acid in 80 °C water bath with continuous stirring. The results of ICP tests are shown in table 3.3. The mass fraction of Pt cocatalyst is around one percent. Hence, approximate amount of Pt suggests the multi-shells may work in improving photocatalytic performance.

3.4.3 Photoelectric Properties and HER Mechanism

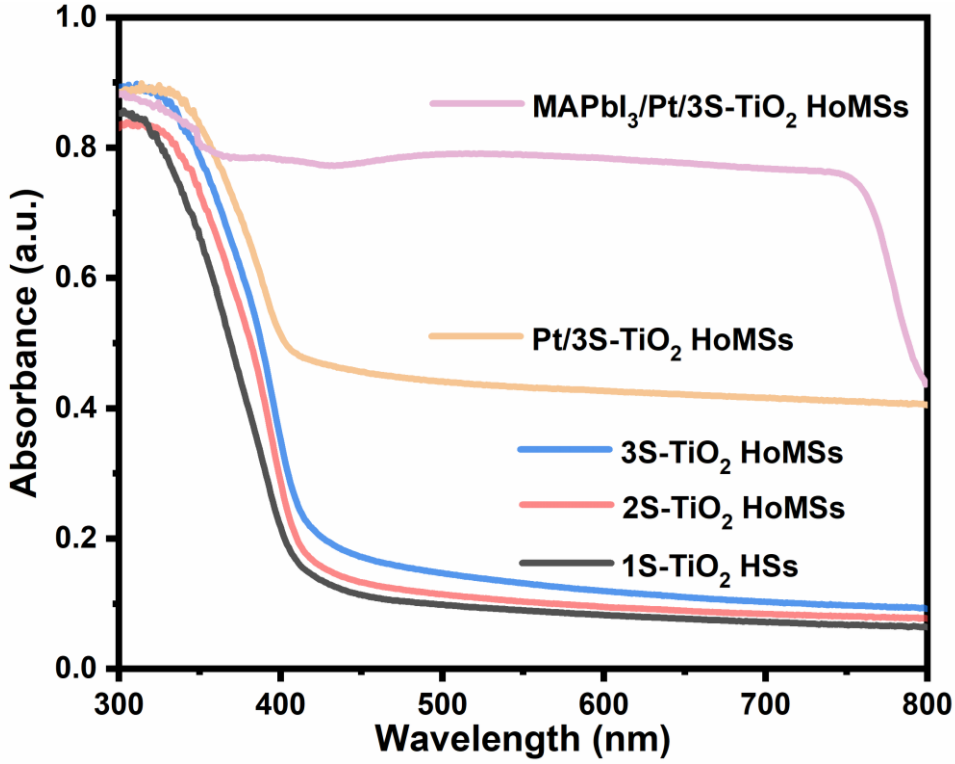

Figure 3.14 UV-vis absorption spectra of TiO_2 HoMSs, Pt/3S-TiO_2 HoMSs and $MAPbI_3$/Pt/3S-TiO_2 HoMSs.

To survey the effect of structure and composition on light absorption, the UV-vis absorption spectrums of different semiconductors were performed as shown in figure 3.14. To survey the effect of structure on light absorption by comparing the light absorption of TiO_2 HoMSs, the 3S-TiO_2 HoMSs presents higher absorbance than 2S-TiO_2 HoMSs and 1S-TiO_2 HSs. The Multi-shelled structures improve light absorption because of the light reflection and light scattering.[88] Increasing light absorption by HoMSs is possibly one of the reasons for performance improvement. On the other hand, the effect of composition on light absorption through comparing the light absorbance between 3S-TiO_2 HoMSs, Pt/3S-TiO_2 HoMSs, and

$MAPbI_3$/Pt/3S-TiO_2 HoMSs. When Pt loaded on the 3S-TiO_2 HoMSs, the Pt/3S-TiO_2 HoMSs is sensitive in visible light as shown in figure 3.14. When $MAPbI_3$ is loaded on Pt/3S-TiO_2 HoMSs, the light absorption in the range of visible light is improved greatly. The photographs of catalysts in figure 3.15 show that the color is changed gradually from white to dark grey. This result also illustrates the macroscopic enhancement of light absorption in the range of visible light wavelength.

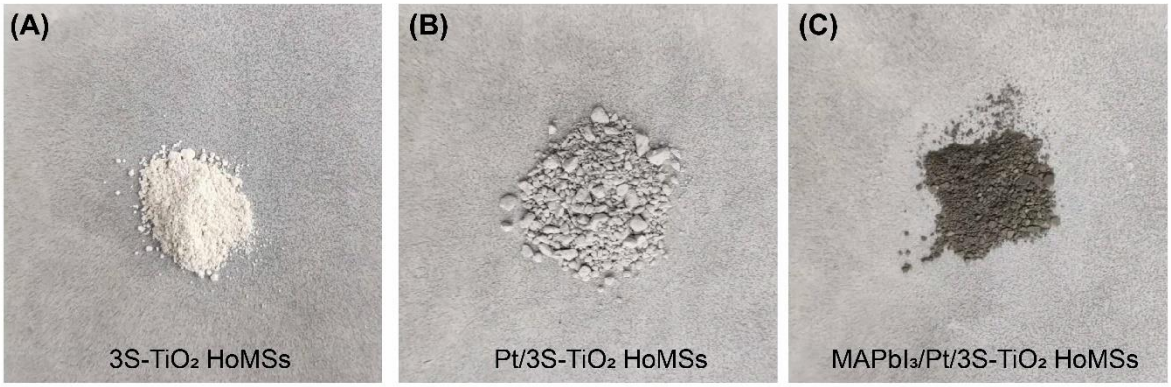

Figure 3.15 The photographs of catalysts: (A) 3S-TiO_2 HoMSs, (B) Pt/3S-TiO_2 HoMSs, and (C) $MAPbI_3$/Pt/3S-TiO_2 HoMSs.

To verify the advantages of multi-shelled structures in charges separation and transport, steady-state PL spectra were carried out as shown in figure 3.16. The photoluminescence intensities of different semiconductors are varied in a wide range. Compared with barely $MAPbI_3$ with the highest intensity, the introduction of TiO_2 HoMSs or Pt decreases the photoluminescence intensity. The reason for photoluminescence quenching is because photoelectrons transfer process.[139, 149, 167] Compared with barely $MAPbI_3$, the sharply decrement of the PL intensity of $MAPbI_3$/Pt/TiO_2 HoMSs reveals that photogenerated electrons within $MAPbI_3$ are effectively extracted, which is attributed to the effective available heterogenous interface of $MAPbI_3$/Pt/TiO_2. The more shells provide more heterogeneous contact interfaces.[177-178] The PL intensity of $MAPbI_3$/Pt/TiO_2 HoMSs decreases as the increase of number of shells. Besides, the PL intensity of the mixture of $MAPbI_3$ and Pt/TiO_2 HoMSs is stronger than $MAPbI_3$/Pt/TiO_2 HoMSs because of the weak contact of interfaces. In addition, the higher PL intensity of $MAPbI_3$/TiO_2 HoMSs comparing with $MAPbI_3$/Pt/TiO_2 HoMSs indicates that the introduced Pt further improves electrons transfer.

Meanwhile, time-resolved transient PL decay spectrum was measured and fitted as shown in

figure 3.17. The resulted parameters are listed in **Table 3.4**. The order of calculated average carrier lifetime of catalysts is $MAPbI_3$ (630.49 ns) > $MAPbI_3$/Pt/1S-TiO_2 HS (15.57 ns) > $MAPbI_3$/Pt/2S-TiO_2 HoMSs (9.18 ns) > $MAPbI_3$/Pt/3S-TiO_2 HoMSs (6.95 ns). The shorter carrier lifetime suggests faster electrons transfer. The PL quenching effect in the PL decay spectra confirms the efficient transportation of photogenerated carriers in $MAPbI_3$/Pt/TiO_2 HoMSs.[168]

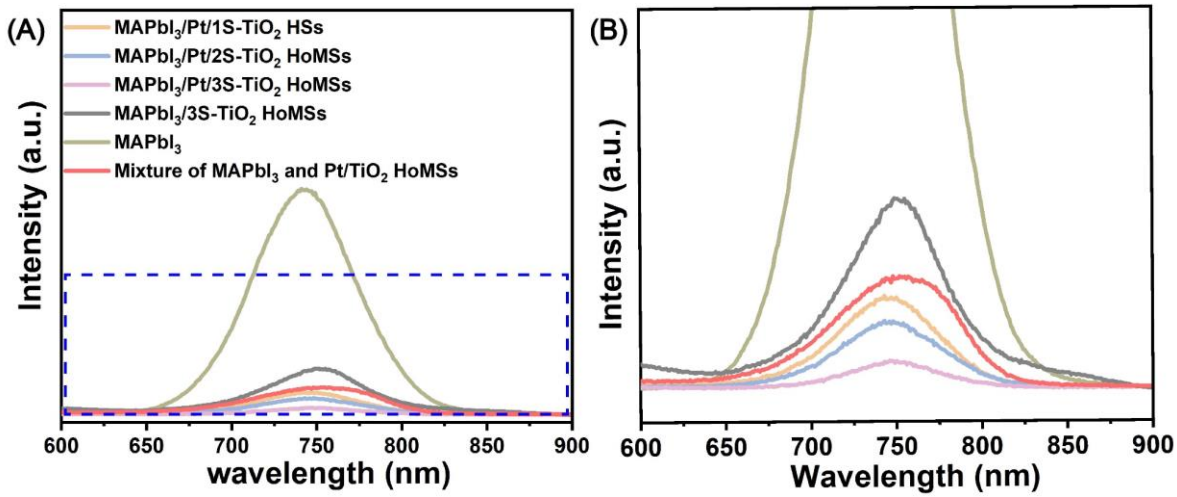

Figure 3.16 (A) Steady-state PL spectra of $MAPbI_3$, $MAPbI_3$/3S-TiO_2 HoMSs, $MAPbI_3$/Pt/TiO_2 HoMSs; (B) Corresponding magnify field of (A) selected area.

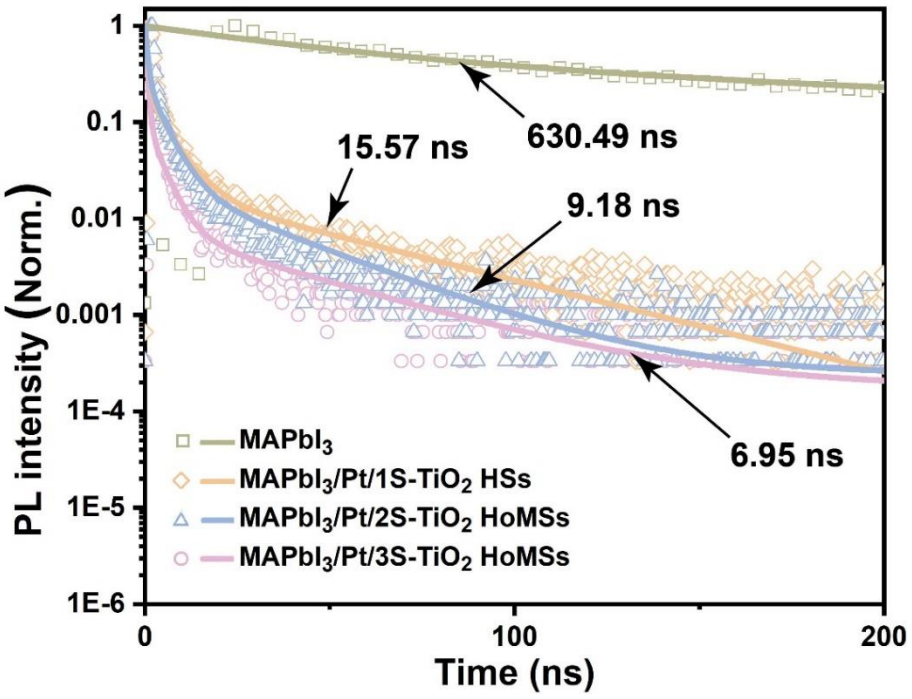

Figure 3.17 Time-resolved transient PL decay spectra of $MAPbI_3$ and $MAPbI_3$/Pt/TiO_2 HoMSs.

Table 3.4 The τ_{ave} of different catalysts fitted from time-resolved transient PL decay spectra.

Sample	τ_1 (ns)	τ_2 (ns)	τ_3 (ns)	B_1	B_2	B_3	τ_{ave} (ns)
$MAPbI_3$	55.6310	302.9098	1257.7075	810.6563	365.9066	78.8893	630.49
$MAPbI_3$/Pt/1S-TiO_2 HSs	0.7269	5.8348	45.7708	3700.8040	509.7860	49.8183	15.57
$MAPbI_3$/Pt/2S-TiO_2 HoMSs	0.6756	4.5766	29.1119	2503.1763	484.4699	42.3545	9.18
$MAPbI_3$/Pt/3S-TiO_2 HoMSs	0.5385	3.9808	37.3044	5116.0332	269.0036	18.4095	6.95

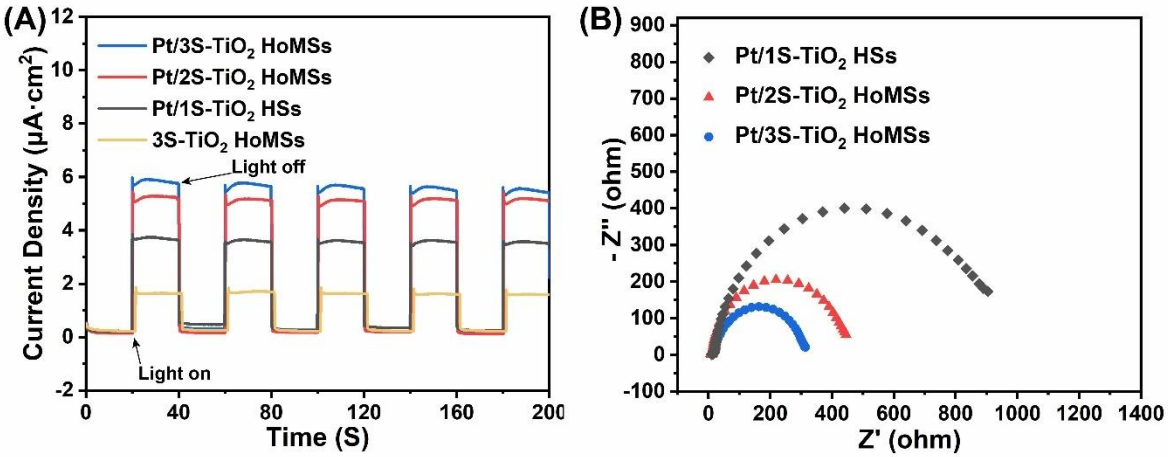

Figure 3.18 (A) The transient photocurrent response curves of Pt/ TiO_2 HoMSs and TiO_2 HoMSs, (B) EIS curves of Pt/ TiO_2 HoMSs measured at 0.1 M Na_2SO_4 with Ag/AgCl electrode.

To study the effect of morphology on photoelectricity properties, the transient photocurrent response curves and EIS curves of Pt/ TiO_2 HoMSs were measured firstly. In figure 3.18A, the current density is a positive value which indicates that TiO_2 HoMSs is an n-type semiconductor. The current density of Pt/ TiO_2 HoMSs is apparently bigger than 3S-TiO_2 HoMSs. This result means that deposited Pt on TiO_2 HoMSs is beneficial to electrons transfer. On the other hand, the current density is gradually increasing as the number of shells increases. When the photocatalysts are illuminated under the full spectrum of light, the current curves sharply increase and decrease because of charges recombination. The trend of photocurrent increment is consistent with the trend of photocatalytic performance. The photocurrent increment may partially be caused by multi-shelled structures. On the other hand, the shells form parallel resistance which decreases electron transfer resistance as shown in figure 3.18B. More shells are contributed to smaller electrons transfer resistance.

Next, the transient photocurrent response curves of $MAPbI_3$/Pt/TiO_2 HoMSs in figure 3.19 display that the larger photocurrents of composites comparing with the pure $MAPbI_3$,

indicating higher photocatalytic HER activities of $MAPbI_3/Pt/TiO_2$ HoMSs. Besides, the larger photocurrent of $MAPbI_3/Pt/TiO_2$ HoMSs suggests that more photogenerated carriers can be efficiently used in photocatalytic reactions. The trend of photocurrent value is opposite of the PL intensity of photocatalysts. And both results indicate Pt/TiO_2 HoMSs improve charges separation and transport from $MAPbI_3$. The transient photocurrent response curves of the mixture of $MAPbI_3$ and $Pt/3S\text{-}TiO_2$ HoMSs were also measured as shown in figure 3.19B. Compared with $MAPbI_3/Pt/3S\text{-}TiO_2$ HoMSs, the mixture shows a lower photocurrent value, which suggests that the photogenerated charges cannot be timely extracted outside.

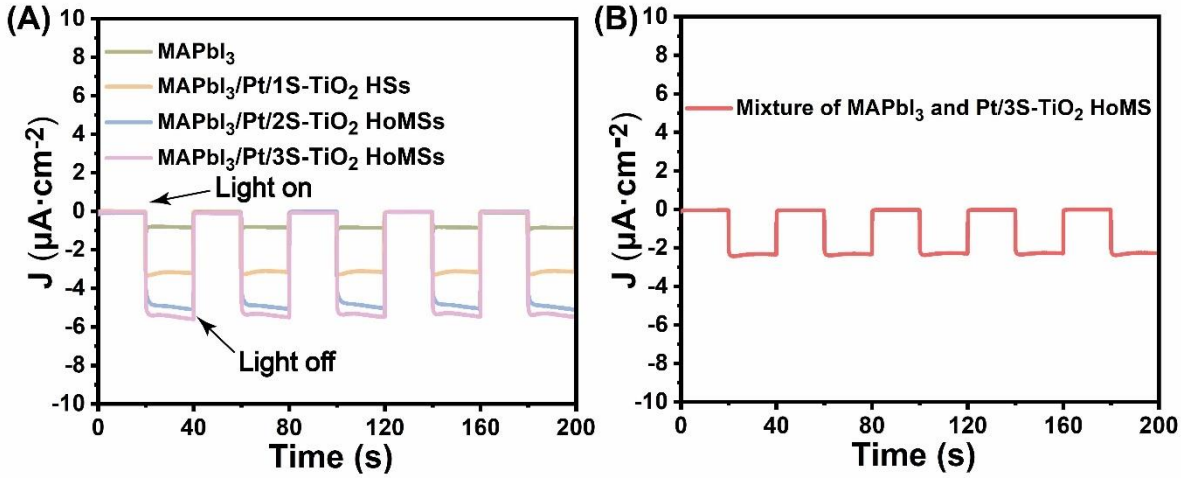

Figure 3.19 The transient photocurrent response curves: (A) the $MAPbI_3$ and $MAPbI_3/Pt/TiO_2$ HoMSs; (B) Mixture of $MAPbI_3$ and Pt/TiO_2 HoMSs. The transient photocurrent response curves of the mixture of the $MAPbI_3$ and $Pt/3S\text{-}TiO_2$ HoMSs measured in dichlormethane solution containing 0.1 M tetrabutylammonium hexafluorophosphate ($TBAPF_6$) as electrolyte solution.

To compare the electron transfer ability of photocatalysts, the EIS curves were measured by an electrochemical workstation as shown in figure 3.20. The first small arc is the electron conduction impedance of materials and the second arc is the charge transfer resistance of ion transfer behavior of photocatalyst.[139] In the magnified area of the first arc, $MAPbI_3$ shows the smallest electron conduction impedance, which suggesting the bulk transfer of electrons in $MAPbI_3$ is better than TiO_2 HoMSs. In the second arc, $MAPbI_3/Pt/TiO_2$ HoMSs presents smaller charge transfer resistance. And the curve of $MAPbI_3/Pt/3S\text{-}TiO_2$ HoMSs is the smallest arc which means the smallest charge transfer resistance among those photocatalysts. Because of multi-shells inside HoMSs, the parallel electron transport pathways are generated and more shells obtain smaller charge transfer resistance.[69, 83] The more shells with abundant

heterogeneous interfaces within HoMSs usefully enhance contact area which is contributed to charges separation and transport, charge utilization in HER.

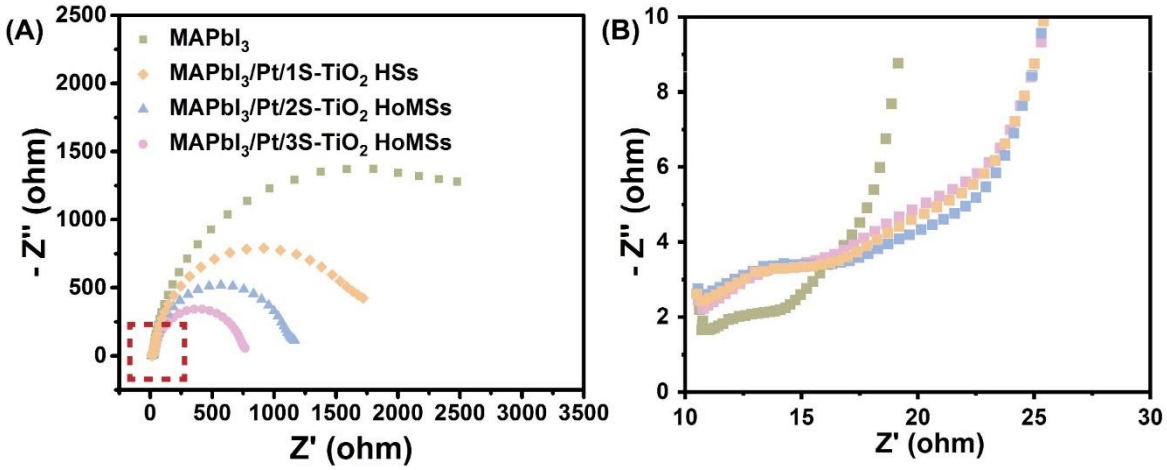

Figure 3.20 (A) EIS curves of $MAPbI_3$ and $MAPbI_3/Pt/TiO_2$ HoMSs at open-circuit voltage versus Ag/AgCl electrode under light illumination; (B) Corresponding magnify field of (A) selected area.

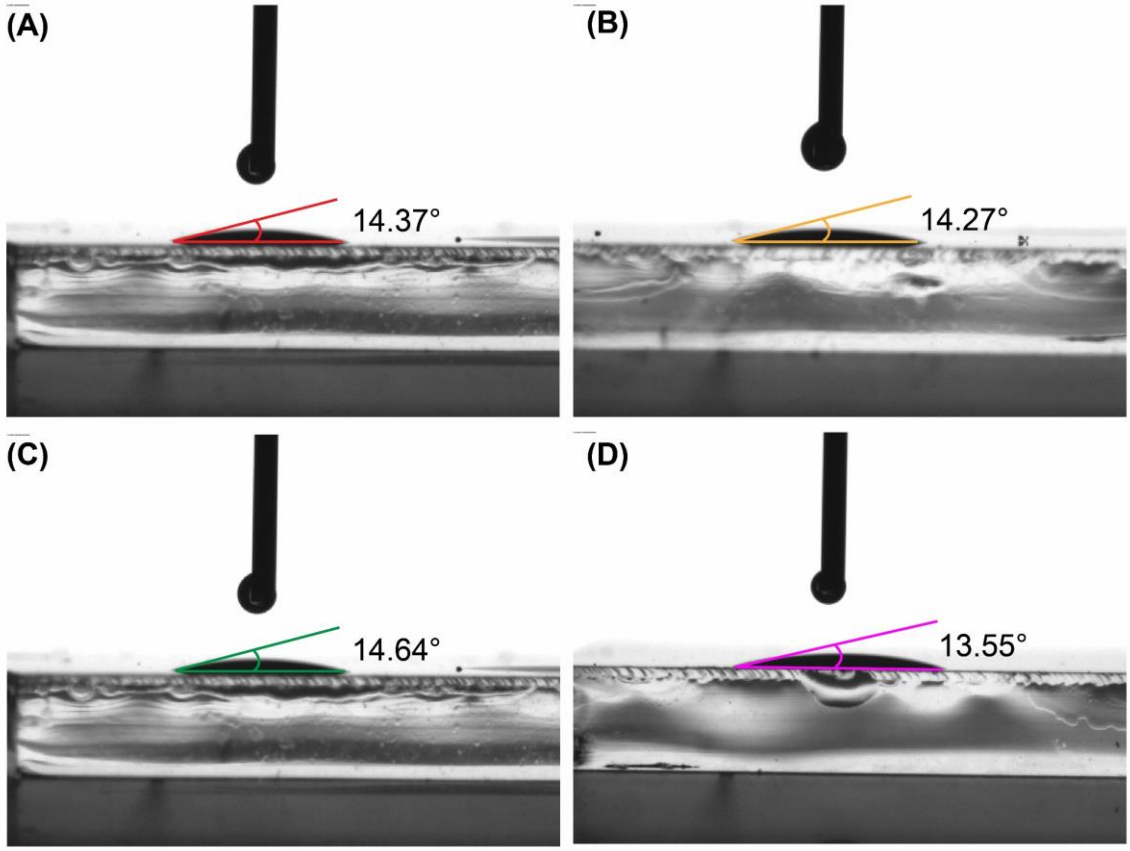

Figure 3.21 Contact angle of different photocatalysts: (A) $MAPbI_3/Pt/1S\text{-}TiO_2$ HS, (B) $MAPbI_3/Pt/2S\text{-}TiO_2$ HoMSs, (C) $MAPbI_3/Pt/3S\text{-}TiO_2$ HoMSs, and (D) $MAPbI_3/Pt/P25\text{-}TiO_2$.

To exclude the effect of wettability on performance, the contact angle was characterized as shown in figure 3.21. The liquid drop used in the test is $MAPbI_3$ saturated solution ($HI:H_3PO_2$). The contact angles of $MAPbI_3/Pt/TiO_2$ HoMSs are 14.37°, 14.27°, and 14.64° for 1 to 3 shells. And the contact angles of $MAPbI_3/Pt/P25\text{-}TiO_2$ is 13.55°. Those approximate contact angles prove photocatalysts possess the same wettability.

To survey the transfer pathways of charges, the conduction band (CB) and valence band (VB) (versus the normal hydrogen electrode, NHE) of the $MAPbI_3/Pt/TiO_2$ HoMSs photocatalysts were determined by the Tauc-plots, ultraviolet photoelectron spectroscopy (UPS) and Mott-Schottky curves. The bandgap of $3S\text{-}TiO_2$ HoMSs and $MAPbI_3$ was confirmed by the Tauc method in the first as shown in figure 3.22. The Tauc method is expressed as the following equation[179]:

$$ahv^{1/r} = B\left(hv - E_g\right) \qquad 3.5$$

Where a, h, and v present absorption coefficient, Planck constant, and frequency, respectively. E_g and B are bandgap energy and constant, respectively. The r factor is decided by the nature of semiconductors. When the semiconductors belong to a direct bandgap, the r factor is equal to 1/2. When the semiconductors belong to an indirect bandgap, the r factor is equal to 2. In this step, the $3S\text{-}TiO_2$ HoMSs is recognized as the indirect bandgap because anatase phase is main part of TiO_2. The Tauc-plots were calculated from the data of UV-vis absorption spectra data. The tangent of Tauc-plots indicate that the bandgaps (E_g) of $3S\text{-}TiO_2$ HoMSs and $MAPbI_3$ are 3.1 eV and 1.57 eV respectively.

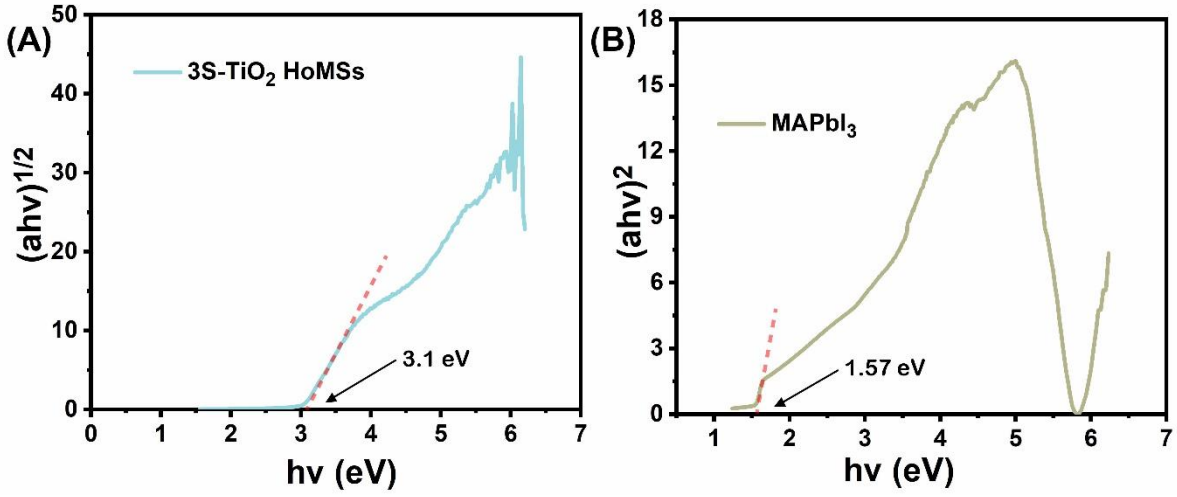

Figure 3. 22 Tauc-plots curves of (A) $3S\text{-}TiO_2$ HoMSs and (B) $MAPbI_3$.

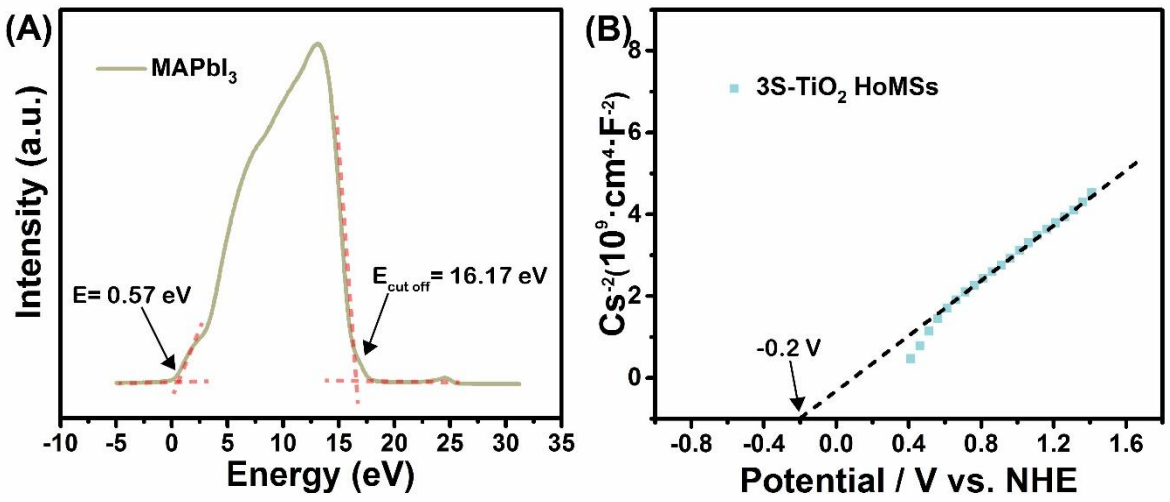

Figure 3.23 (A) Ultraviolet photoelectron spectroscopy (UPS) of the $MAPbI_3$ powder; (B) The Mott-Schottky curve of 3S-TiO_2 HoMSs was measured at 1000 Hz.

To confirm the conduction band energy (E_{CB}) and valence band energy (E_{VB}), the UPS of $MAPbI_3$ and Mott-Schottky curve of 3S-TiO_2 HoMSs were measured as shown in the figure 3.23. The Fermi level of the $MAPbI_3$ is -5.04 eV, which is calculated from the following formula:

$$\mathrm{E_{fermi}} = -\left(\mathrm{E_{excitation\ energy}} - \mathrm{E_{cut\ off}}\right) = -(21.21\ \mathrm{eV} - 16.17\ \mathrm{eV}) = -5.04\ \mathrm{eV} \qquad 3.6$$

Further, the difference value between the E_{VB} to E_{fermi} is equal to 0.57 eV as shown in figure 3.23A. because the E_{VB} is lower than E_{fermi}, the E_{VB} is equal -5.61 eV. According to the bandgap of $MAPbI_3$ obtained, the E_{CB} is obtained from the following formula:

$$E_{CB} = E_g + E_{VB} = 1.57\ \mathrm{eV} + (-5.61\ \mathrm{eV}) = -4.04\ \mathrm{eV} \qquad 3.7$$

When using the NHE as a reference,[180] the conduction band potential is -0.46 V (vs. NHE), and the valence band potential is 1.11 *V* (vs. NHE) for $MAPbI_3$. Similarly, the conduction band potential is -0.2 *V* (vs. NHE) as shown in figure 3.23B, and the valence band potential is 2.90 V (vs. NHE) for 3S-TiO_2 HoMSs.

According to the E_{CB} and E_{VB} mentioned above, the transfer pathways are clear between TiO_2 and $MAPbI_3$. And the photogenerated charges transfer pathways are shown in figure 3.24. The potential difference between TiO_2 and $MAPbI_3$ provides a force to drive the photogenerated electrons injected into the CB of TiO_2 from the CB of $MAPbI_3$. Further, the co-catalysts Pt on the surface of TiO_2 obtained electrons from TiO_2 and then converts hydrogen ions to hydrogen. The generated holes in the VB of $MAPbI_3$ participate in a reaction of I^- to I_3^-. In this chapter, the H_3PO_2 is used as a stabilizer to prevent oxidation of I^- in the air.

At the same time, the H_3PO_2 is also used to convert photocatalytic generated I_3^- into I^-. In the other words, the H_3PO_2 enhances the consumption of holes for depressing recombination.

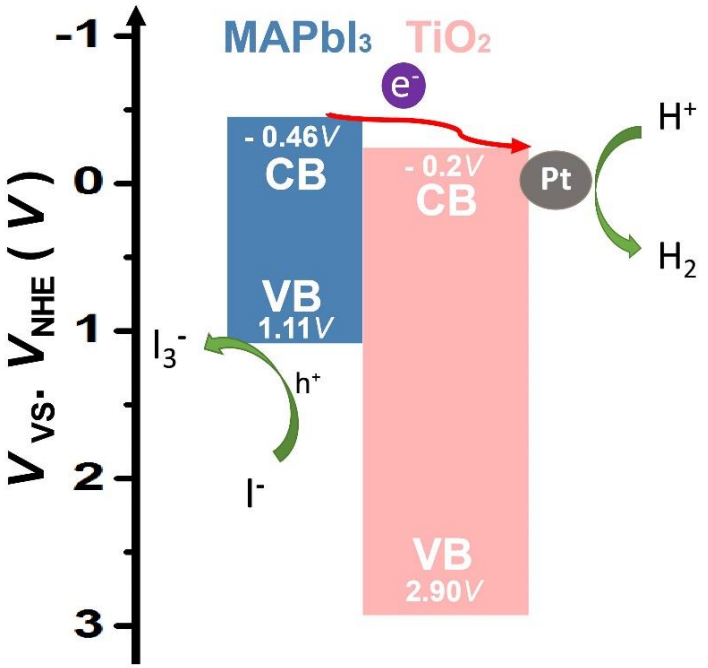

Figure 3.24 Schematic energy band diagram of the $MAPbI_3$, Pt/TiO_2, and charge transfer process under visible-light illumination.

3.5 Conclusions

In summary, the $MAPbI_3/Pt/TiO_2$ HoMSs composites were successfully applied in photocatalytic hydrogen evolution from HI splitting. The introduced $MAPbI_3$ in Pt/TiO_2 HoMSs improves photocatalytic activity. The H_2 evolution rate of samples of $MAPbI_3/Pt/3S$-TiO_2 HoMSs is 6856.2 μmol h^{-1} g^{-1} under visible light irradiation, which is far faster than barely $Pt/MAPbI_3$ (268.6 μmol h^{-1} g^{-1}). As the shells increase, the photocatalytic performances of composites increase. The characterizations, such as PL spectra, transient photocurrent response curves, and EIS curves, indicate that the multi-shells improve charges separation and transport effectively. The cocatalyst enhances the utilization of the photogenerated charges and splitting efficiency. This chapter verifies the advantages of HoMSs in the photocatalytic HER field. Loading narrow bandgap semiconductors inside HoMSs is a new strategy to broaden the light response range.

CHAPTER 4.

Effects of Anatase/Rutile Phase of $MAPbI_3/Pt/TiO_2$ Composite on Photocatalytic HER Performance

4.1 Abstract

Optimizing electrons transfer is contributed to improving photocatalytic performance in HER performance. The electrons transfer pathways of $MAPbI_3/Pt/TiO_2$ HoMSs include $MAPbI_3$ bulk, interfaces of $MAPbI_3$ and TiO_2 HoMSs, TiO_2 bulk, interfaces of TiO_2 and cocatalyst. Rutile TiO_2 and anatase TiO_2 show differences in interface transfer and TiO_2 bulk transfer. To investigate the influence of rutile TiO_2 and anatase TiO_2 on electrons transfer, the different anatase ratios of TiO_2 were synthesized by calcined at different temperatures. The comparations of electrons transport between anatase and rutile was characterized by EIS, transient photocurrent response, and linear sweep voltammetry method. The experimental results prove that electrons transfer in $MAPbI_3$/anatase is faster than $MAPbI_3$/rutile. $MAPbI_3$/anatase possesses smaller transfer resistance and higher transient photocurrent value. Comparing with electrons transfer in the $MAPbI_3$/rutile, the faster bulk transport in anatase is beneficial to improving performance.

4.2 Introduction

Charges separation and transfer process play a quite important role in photocatalytic HER performance. The common effective charges separation strategy is to construct heterojunctions.[181-182] In the charges transfer process, the charges recombination easily happens in traps such as defects or doping.[183] Optimizing electrons transfer affects whether the photogenerated electron can take part in surface photocatalytic chemical reactions and then be utilized effectively. Impactors of electrons transfer include work function,[184] defects,[185] electric field,[186] transfer distance,[69, 187] electron mobility.[100]

The TiO_2 materials have three kinds of crystal structure, including rutile, anatase, and brookite. The rutile and anatase are usually applied in the photocatalytic field.[185-189] In chapters 2 and

3, the heterogeneous interface of $MAPbI_3$ and mixed-phase of TiO_2 HoMSs has been successfully constructed and applied in photocatalytic HER. When $MAPbI_3$ is irradiated under light, the electrons are generated and separated into TiO_2 HoMSs. The electrons transfer pathways include $MAPbI_3$ bulk, interfaces of $MAPbI_3$ and TiO_2 HoMSs, TiO_2 bulk, and interfaces of TiO_2 and cocatalyst. The main electron transfer pathways are concerned with TiO_2 materials. Electrons transfer in the interfaces of $MAPbI_3$ and TiO_2 HoMSs has been widely studied in perovskite solar cells.[189-190] Compared with $MAPbI_3$/anatase, some devices based on $MAPbI_3$/rutile present higher power conversion efficiency and external quantum efficiency.[101, 189] The transient absorption spectra of interfaces of $MAPbI_3/TiO_2$ show that the extraction ability of rutile from $MAPbI_3$ film is better than anatase.[101]

In the TiO_2 HoMSs bulk transfer process, rutile and anatase show different properties. The rutile is a direct bandgap semiconductor and its bandgap is around 3.0 eV. The anatase is an indirect bandgap semiconductor and its bandgap is around 3.2 eV. The anatase TiO_2 presents a longer lifetime of carriers than rutile TiO_2. On the other hand, the electron mobility of anatase (10 $cm^2 \cdot V^{-1} \cdot s^{-1}$) is larger than rutile (1 $cm^2 \cdot V^{-1} \cdot s^{-1}$).[100] The electron transfer in anatase bulk is faster than rutile. Hence, the rutile TiO_2 is beneficial to the extraction of electrons from $MAPbI_3$ to TiO_2. In contrast, the anatase TiO_2 is beneficial to electrons transfer of TiO_2 bulk.

Turning crystal structure anatase/rutile is irreversible. Normally, the transformation of crystal structure is from anatase into rutile phase because the rutile phase is more stable. According to reported literatures,[102-103, 191] the phase transformation can be realized by impurities or high temperature. In general, the phase transformation requires a temperature of at least over 400 °C which is decided by raw materials, methods, pressure, or synthesis process.[131]

In this chapter, to investigate the influence of rutile TiO_2 and anatase TiO_2 on electrons transfer, the different anatase ratios of TiO_2 were synthesized by calcined at different temperatures. The different anatase ratio of TiO_2 was confirmed by XRD. The $MAPbI_3/Pt/TiO_2$ HoMSs materials with different anatase ratios were synthesized by the same method used in chapter 2. And then it was applied in the photocatalytic HER process. The applied photocatalytic conditions keep consistent with test conditions in chapter 3. The contrast of electrons transport between anatase and rutile was characterized by EIS, transient photocurrent response, and linear sweep voltammetry method. The experimental results prove that electrons transfer in $MAPbI_3$/anatase is faster than $MAPbI_3$/rutile. $MAPbI_3$/anatase possesses smaller transfer resistance and higher transient photocurrent value.

4.3 Experiment Section

4.3.1 Chemicals

The chemicals used in this chapter is consistent with chapter 2.

4.3.2 Experimental Equipment

The experimental equipment used in this chapter is consistent with chapter 2.

4.3.3 Methods

4.3.3.1 Synthesis of Different Anatase Ratio in Mix Phase of 3S-TiO_2 HoMSs

The above-prepared CMSs were firstly washed with ethanol at room temperature for 4 hours and dried at 60 °C for 12 hours. The as-pretreated CMSs were firstly ground by agate mortar. Then, dispersing 1.2 g obtained CMSs powers into 3 mol L^{-1} $TiCl_4$ aqueous solution (60 mL) was carried out in an ultrasonicator for 10 min. The above suspending solution was kept stirring for 7 hours at 40 °C. After the stirring process, the suspending solution was filtrated and washed by a Buchner funnel with deionized water two times followed by drying at 60 °C for 6 hours. In the end, the obtained sample was put into a muffle furnace. The sample was heated to 500 °C-700 °C in the air from room temperature with the heating of 9 °C min^{-1} and kept for 2 hours. The white power of 3S-TiO_2 HoMSs is obtained.

4.3.3.2 Synthesis of 2S-TiO_2 HoMSs

The above-prepared CMSs were firstly washed with ethanol at room temperature for 4 hours and dried at 60 °C for 12 hours. The as-pretreated CMSs were firstly ground by agate mortar. Then, dispersing 1.2 g obtained CMSs powers into 3 mol L^{-1} $TiCl_4$ aqueous solution (60 mL) was carried out in an ultrasonicator for 10 min. The above suspending solution was kept stirring for 5 hours at 40 °C. After the stirring process, the suspending solution was filtrated and washed by a Buchner funnel with deionized water two times followed by drying at 60 °C for 6 hours. In the end, the obtained sample was put into a muffle furnace. The sample was heated to 500 °C in the air from room temperature with the heating of 7 °C min^{-1} and kept for 2 hours. The white power of 2S-TiO_2 HoMSs is obtained.

4.3.3.3 Synthesis of 1S-TiO_2 HSs

The above-prepared CMSs were directly used without pretreatment. The as-prepared CMSs were firstly ground by agate mortar. Then, dispersing 1.2 g obtained CMSs powers into 3 mol

L^{-1} $TiCl_4$ aqueous solution (60 mL) was carried out in an ultrasonicator for 10 min. The above suspending solution was kept stirring for 6 hours at room temperature. After the stirring process, the suspending solution was filtrated and washed by a Buchner funnel with deionized water two times followed by drying at 60 °C for 6 hours. In the end, the obtained sample was put into a muffle furnace. The sample was heated to 500 °C in the air from room temperature with the heating of 5 °C min^{-1} and kept for 2 hours. The white power of 1S-TiO_2 HSs is obtained.

4.3.3.4 Synthesis of Pt/TiO_2 HoMSs and $MAPbI_3/Pt/TiO_2$ HoMSs.

The synthesis conditions and processes of Pt/TiO_2 HoMSs and $MAPbI_3/Pt/TiO_2$ HoMSs are consistent with chapter 2.

4.3.3.5 Photocatalytic H_2 Evolution.

The experimental equipment used in this chapter is consistent with chapter 3.

4.3.4 Characterizations

The experimental equipment and methods used in this chapter are consistent with chapter 3.

4.4 Results and Discussions

4.4.1 Synthesis and Characterizations of TiO_2 HoMSs and $MAPbI_3/Pt/TiO_2$ HoMSs

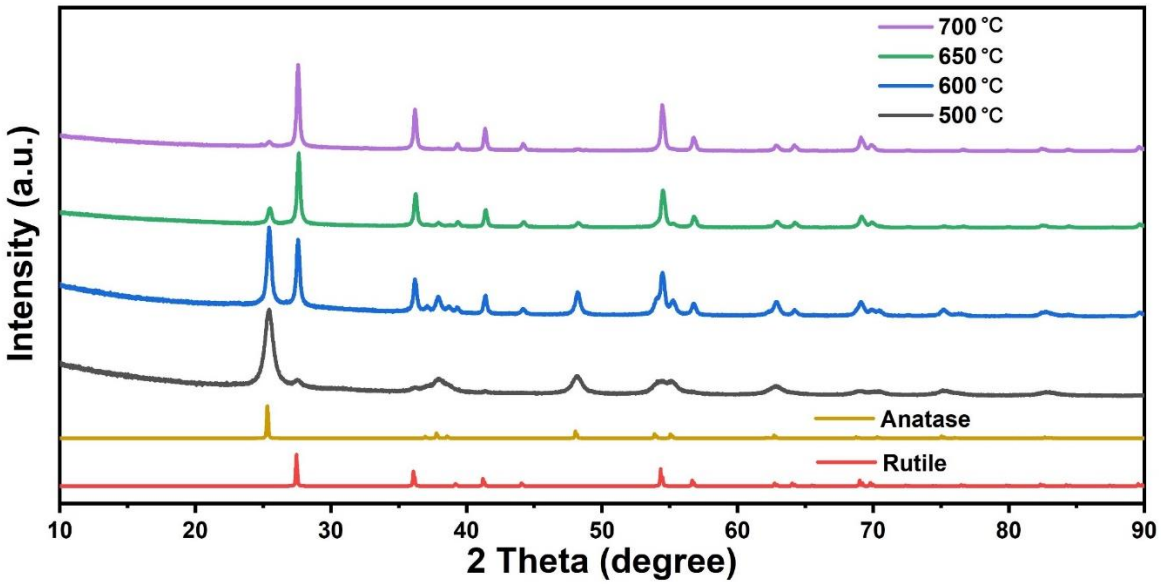

Figure 4.1 The XRD patterns of 3S-TiO_2 HoMSs synthesized in different calcination temperatures.

The anatase and rutile are two kinds of crystal structures of TiO_2. To obtain the anatase TiO_2 and rutile in this chapter, the experiments of the calcined process at different temperatures were carried out. And the XRD results are shown in figure 4.1. The diffraction peaks correspond to diffraction characteristic peaks of anatase (JCPDF: 21-1272) and rutile (JCPDF: 21-1276). As the calcined temperatures increase, the diffraction intensity of rutile TiO_2 is gradually increasing. After being deducted from the baseline, the weight fraction of rutile (W_R) is calculated by equation 2.1 as shown in table 4.1. When the calcination temperature is at 500 °C, the mass fraction of the anatase is 92.1 % and the sample calcined at 500 °C is regarded as anatase TiO_2. When the calcination temperature is at 700 °C, the mass fraction of the rutile is 95.52 % and the sample calcined at 700 °C is regarded as rutile TiO_2.

Table 4.1 The mass fraction of rutile TiO_2 calcined at different temperatures.

Calcination temperature (°C)	Mass fraction of anatase (%)	Mass fraction of rutile (%)
500	92.10	7.90
600	51.05	48.95
650	15.98	84.02
700	4.48	95.52

To observe the morphology of Pt/3S-TiO_2 HoMSs calcined at different temperatures, the TEM was carried out as shown in figure 4.2. The Pt was deposited on the surface of TiO_2 by the photoreduction method which is consistent with chapter 2. There is no obvious agglomerating Pt cluster. Compared with different samples, the thickness of the outermost shell is around 100 nm. In this chapter, we suppose that electron transfer distance is no difference between samples calcined at different temperatures because of the same thickness of shells.

To compare the electron transfer between $MAPbI_3$/Pt/anatase and $MAPbI_3$/Pt/rutile, the samples calcined at 500 °C and 700 °C were chosen. To avoid the $MAPbI_3$ perovskite effect on the HER performance, the synthesis method and processes of $MAPbI_3$/Pt/3S-TiO_2 HoMSs were consistent with chapter 2. The TEM results in figure 4.3 show that $MAPbI_3$ was successfully introduced inside of Pt/3S-TiO_2 HoMSs. The $MAPbI_3$ crystals similarly exist in the inner cavity and middle cavity.

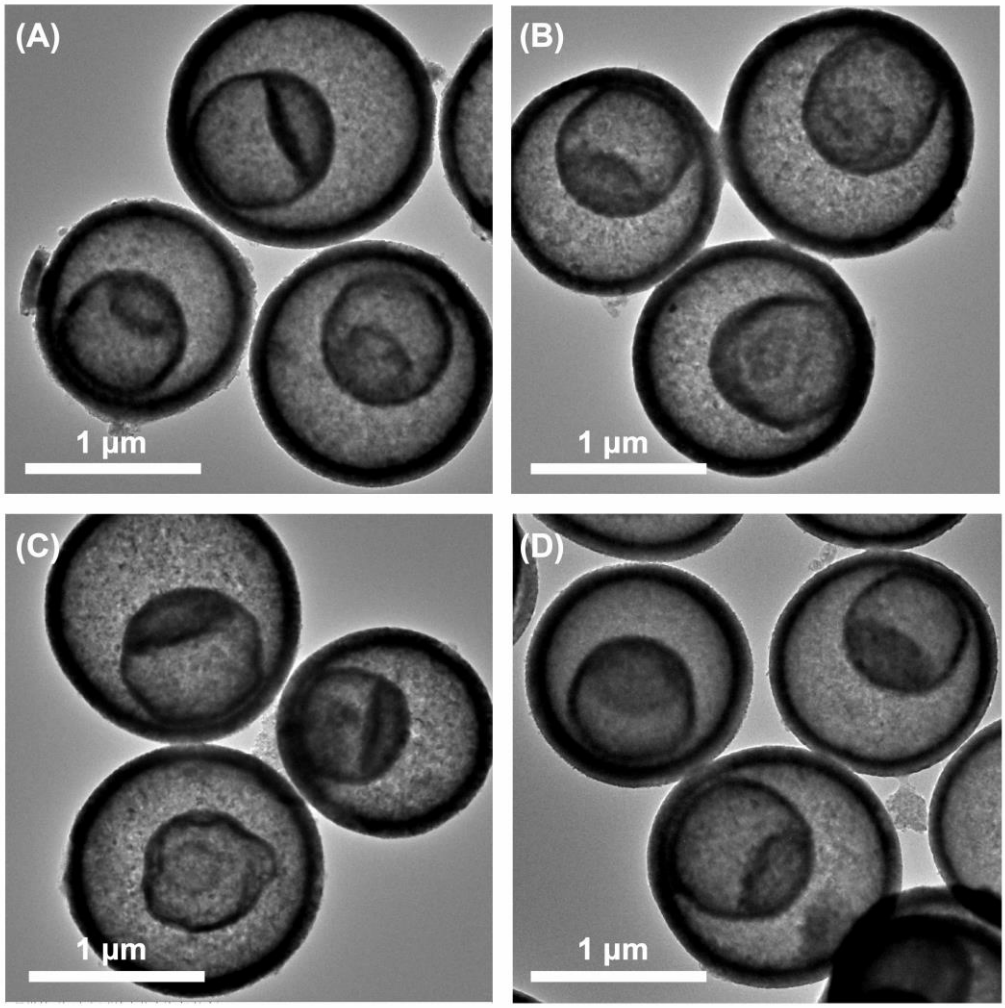

Figure 4.2 The TEM images of Pt/3S-TiO_2 HoMSs synthesized in different calcination temperatures: (A) 500 °C, (B) 600 °C, (C) 650 °C, and (D) 700 °C.

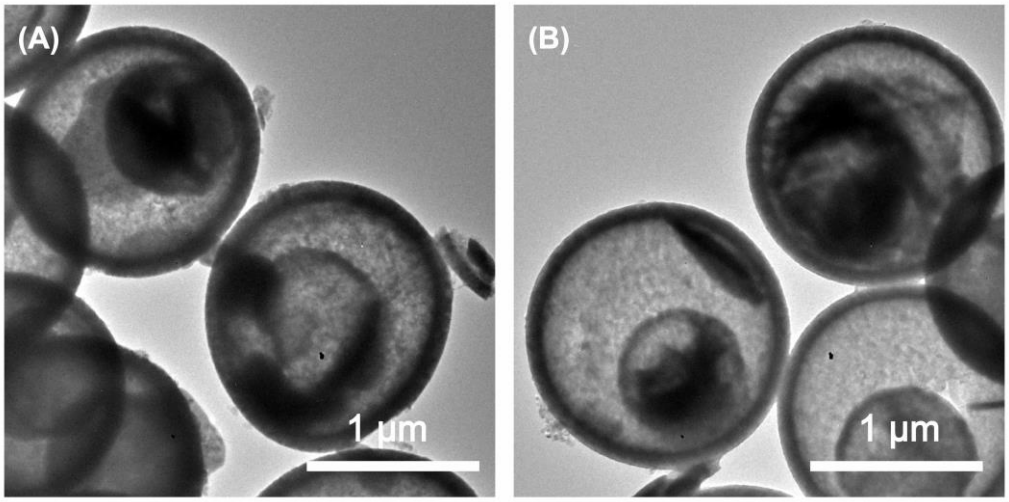

Figure 4.3 The TEM images of $MAPbI_3$/Pt/3S-TiO_2 HoMSs with different 3S-TiO_2 HoMSs synthesized in varied calcination temperatures: (A) 500 °C, (B) 700 °C.

4.4.2 HER Performance of $MAPbI_3$/Pt/3S-TiO_2 HoMSs with Different Phase Ratios

The photocatalytic HER performance of $MAPbI_3$/Pt/3S-TiO_2 HoMSs was measured under the same conditions in chapter 3. To avoid the effect of ultraviolet light on TiO_2, the HER test was irradiated under visible light by a light filter (λ>420 nm). The H_2 evolution results are shown in figure 4.4. The performance of the sample of $MAPbI_3$/Pt/3S-TiO_2 HoMSs-500 °C (819.43 μmol) is higher than the sample of $MAPbI_3$/Pt/3S-TiO_2 HoMSs-700 °C (510.03 μmol). The H_2 increment per half-hour in figure 4.4 shows that the sample of $MAPbI_3$/Pt/3S-TiO_2 HoMSs-500 °C is more H_2 increment around 40 μmol than the sample of $MAPbI_3$/Pt/3S-TiO_2 HoMSs-700 °C. In addition, in the $MAPbI_3$/Pt/TiO_2 photocatalyst, the performance of higher weight fraction of anatase in TiO_2 HoMSs (500 °C) is better than the photocatalyst of $MAPbI_3$/Pt/3S-TiO_2 HoMSs calcined at 550 °C in chapter 3 (719.9 μmol). Those results mean that the photocatalyst composed with anatase (92.10 wt.%) obtains better photocatalytic efficiency.

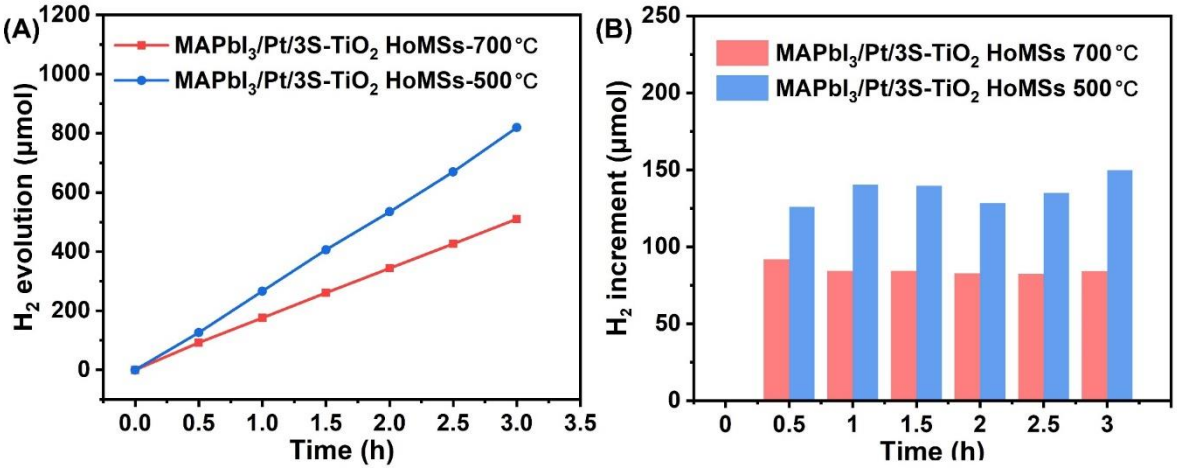

Figure 4.4 (A) The HER performance of $MAPbI_3$/Pt/3S-TiO_2 HoMSs. (B) The increment of H_2 evolution per hour.

4.4.3 Photoelectric Properties

To compare the charge transfer ability of samples, the EIS curves were measured at methylene dichloride solution containing 0.1 mol/L $TBAPF_6$ electrolyte. The EIS curves in figure 4.5 show the circle of $MAPbI_3$/Pt/3S-TiO_2 HoMSs-500 °C is a smaller semicircle, which indicates the effective separation of photogenerated electron-hole pairs and fast charge transfer.[192] The radius of the semicircle implies the photocatalytic HER rate happening at the surface. The photocatalyst of $MAPbI_3$/Pt/ 3S-TiO_2 HoMSs-500 °C with a smaller arc means smaller charges transfer resistance (*Rct*) when compared with $MAPbI_3$/Pt/3S-TiO_2 HoMSs-

700 °C. The photocatalyst with a higher anatase ratio contributes to efficient electrons transfer which enhances photocatalytic HER efficiency.

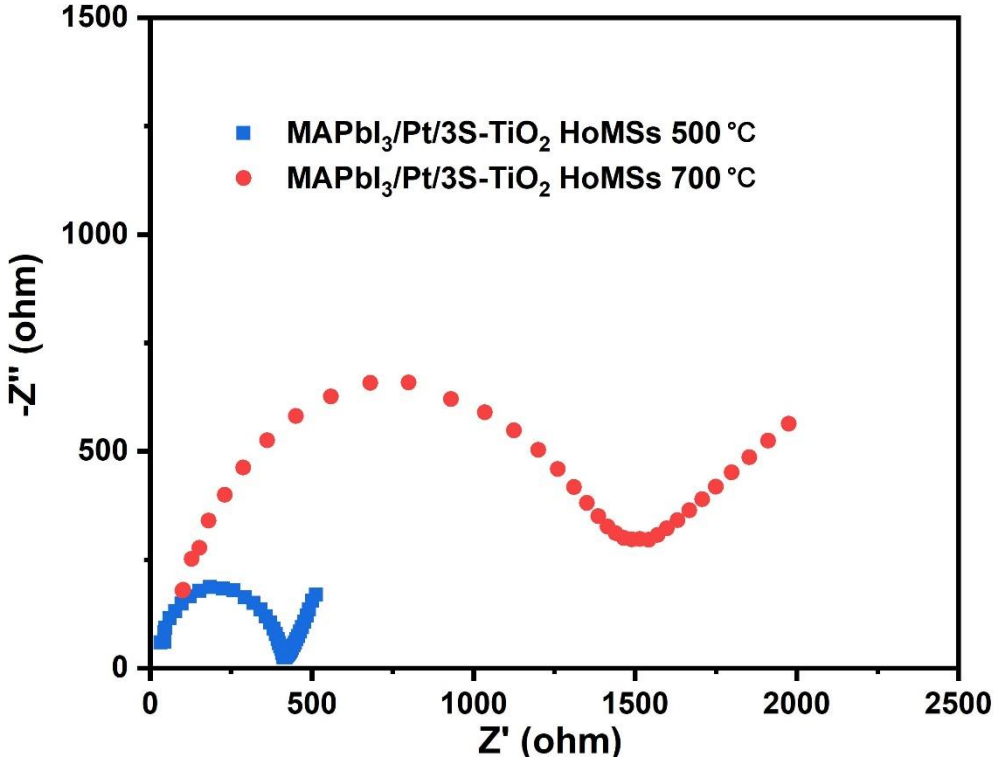

Figure 4.5 EIS curves of $MAPbI_3/Pt/TiO_2$ HoMSs at open-circuit voltage versus Ag/AgCl electrode under light illumination.

To investigate electron transfer between $MAPbI_3/Pt/3S\text{-}TiO_2$ HoMSs-500 °C and $MAPbI_3/Pt/3S\text{-}TiO_2$ HoMSs-700 °C, the transient photocurrent response curves were tested in different light intensities as shown in figure 4.6. Under the light density of 100 $mW \cdot cm^{-2}$ in figure 4.6A, the photocurrent curves increase sharply into a platform and decrease sharply. The higher current intensity stems from effective charges separation.[193-195] When the light intensity turns to 150 $mW \cdot cm^{-2}$, the photocurrent curve of $MAPbI_3/Pt/3S\text{-}TiO_2$ HoMSs-500 °C also increases sharply into a platform. But the photocurrent curve of $MAPbI_3/Pt/3S\text{-}TiO_2$ HoMSs-500 °C increases to the highest point and then decreases slightly. The decrement indicates that charges recombination happened when light intensity increases. While under 200 $mW \cdot cm^{-2}$, The slope of the platform is greater. Both photocurrent curves are gradually decreasing because electrons are not exported in time. After light is off, the photocurrent curves decay phenomenon occurs because of the recombination of electron-hole pairs on photocatalysts surface.[193] As the light intensity increases, the slope of the platform turns steeper, especially under 250 $mW \cdot cm^{-2}$ in figure 4.6D. When the light intensity increases,

more and more electrons are generated. The sample of $MAPbI_3$/Pt/3S-TiO_2 HoMSs-500 °C presents better electron transfer ability.

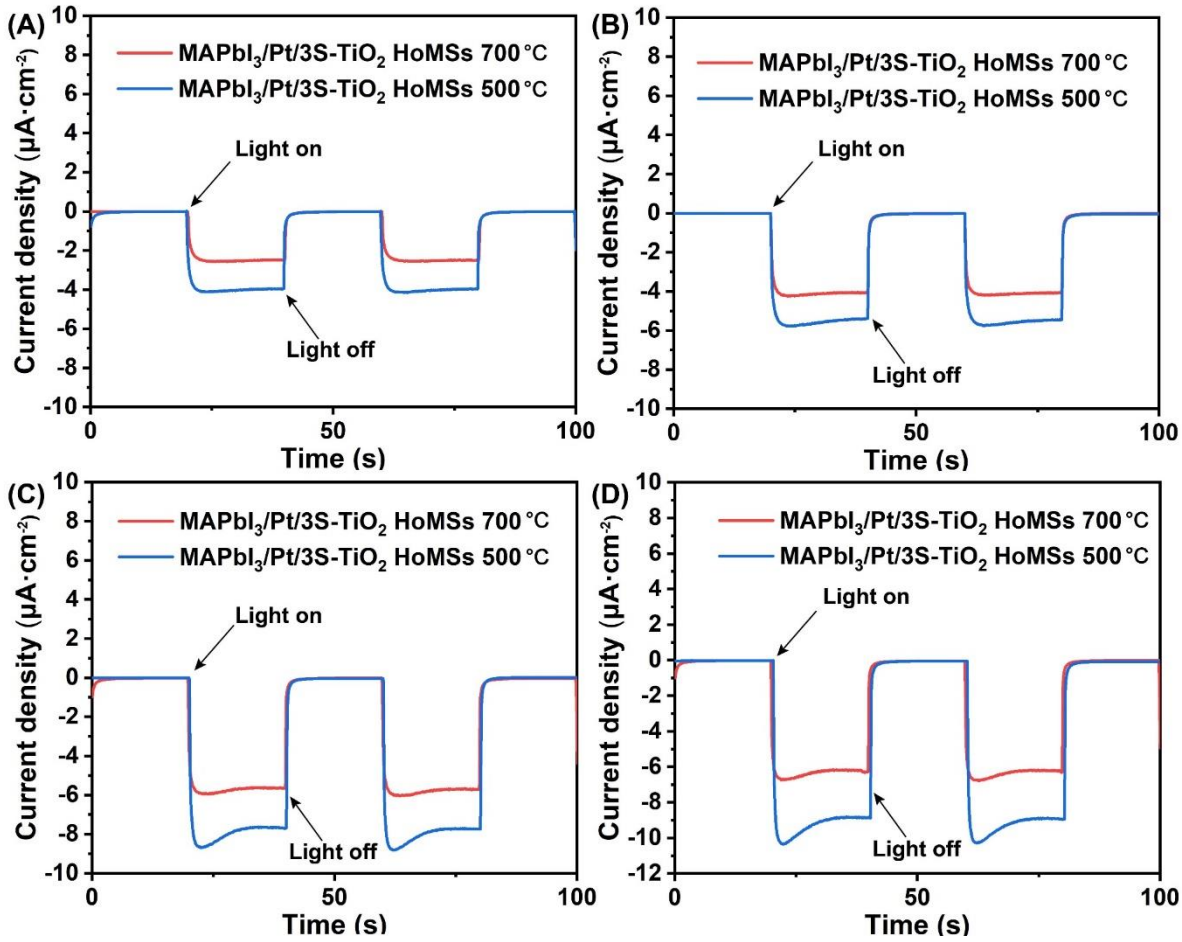

Figure 4.6 Transient photocurrent response curves of $MAPbI_3$/Pt/3S-TiO_2 HoMSs measured under different light power density (λ > 420 nm): (A) 100 mW·cm^{-2}, (B) 150 mW·cm^{-2}, (C) 200 mW·cm^{-2}, (D) 250 mW·cm^{-2}.

To exclude the effects of Pt on electrons transfer, transient photocurrent response curves of $MAPbI_3$/3S-TiO_2 HoMSs were carried out as shown in figure 4.7. When the test is under 100 mW·cm^{-2}, the peak photocurrent is approximate between the two samples. But the current curve of $MAPbI_3$/3S-TiO_2 HoMSs-700 °C is gradually decreasing. When the light intensity increases to 150 mW·cm^{-2} or even bigger, the sample of $MAPbI_3$/3S-TiO_2 HoMSs-500 °C presents a higher current density which means effective charges utilization. The photocurrent response behavior of $MAPbI_3$/3S-TiO_2 HoMSs-500 °C is faster than $MAPbI_3$/3S-TiO_2 HoMSs-700 °C. The faster response behavior indicates quick charges separation and transferability. Without Pt cocatalysts, the electrons transfer pathways include $MAPbI_3$ bulk transfer, interface transfer between $MAPbI_3$ and TiO_2, and TiO_2 bulk transfer. The main

differences in electron transfer pathways are interface transfer and TiO_2 bulk transfer because of the same $MAPbI_3$ materials. Anatase TiO_2 HoMSs-500 °C with faster electron mobility may be the main reason for quick charges separation and transferability.

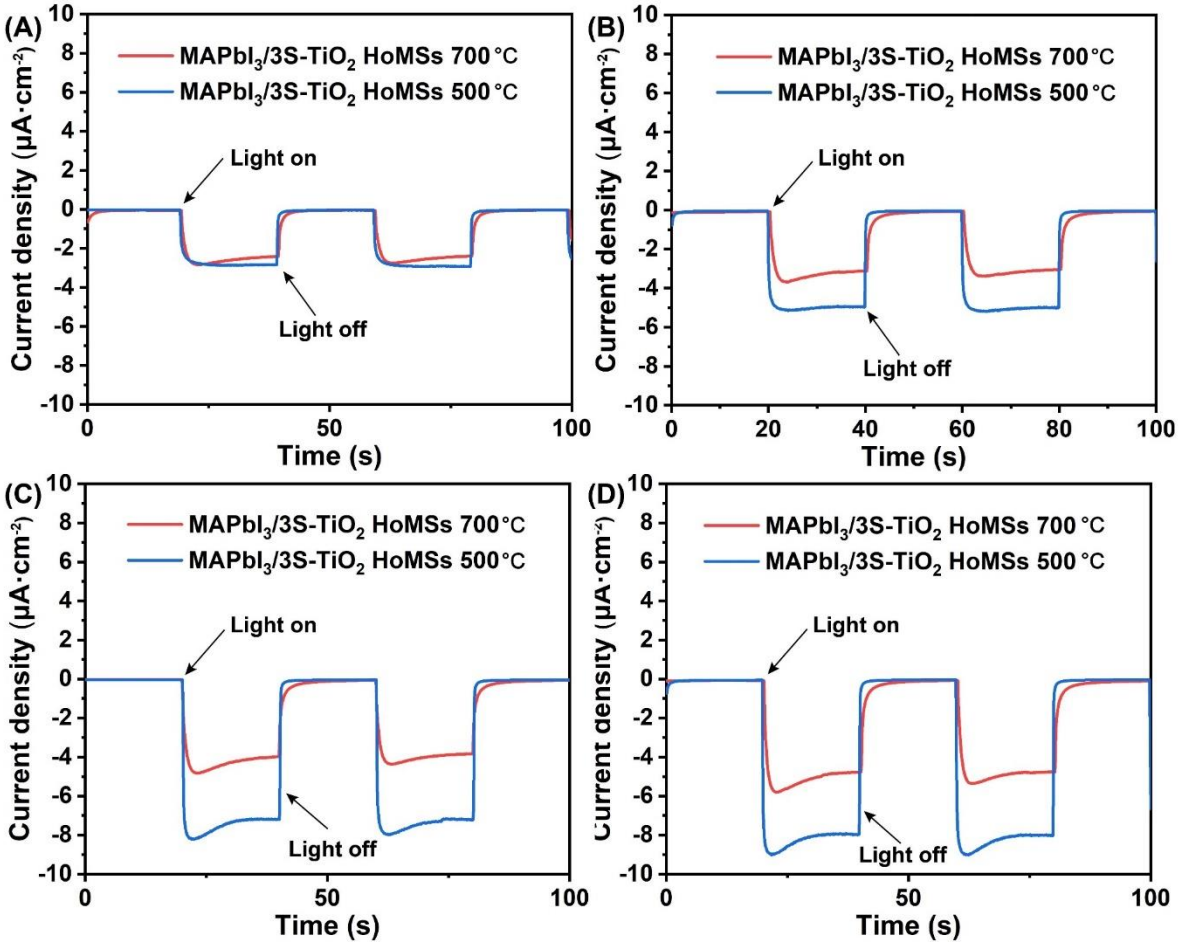

Figure 4.7 Transient photocurrent response curves of $MAPbI_3$/3S-TiO_2 HoMSs measured under different light power density (λ > 420 nm): (A) 100 mW·cm^{-2}, (B) 150 mW·cm^{-2}, (C) 200 mW·cm^{-2}, and (D) 250 mW·cm^{-2}.

For better comparison of the electron transferability, the transient photocurrent response curves were tested in different illumination times as shown in figure 4.8. In figure 4.8A, the photocurrent curve of $MAPbI_3$/Pt/3S-TiO_2 HoMSs-500 °C increases to the highest value in the first illumination time of 2 seconds. When illumination time changed at 5 seconds, the response curves approximate square which further proves the better electron transferability.[196] In contrast, the photocurrent curve of $MAPbI_3$/Pt/3S-TiO_2 HoMSs-700 °C is unable to increase to the highest value in the first illumination time of 2 seconds in figure 4.7B. Compared with figure 4.8B, the response curves quickly fall back to zero point in figure 4.7A. This phenomenon also indicates that $MAPbI_3$/Pt/3S-TiO_2 HoMSs-500 °C with better

electrons transfer ability after power off of simulation light.[197]

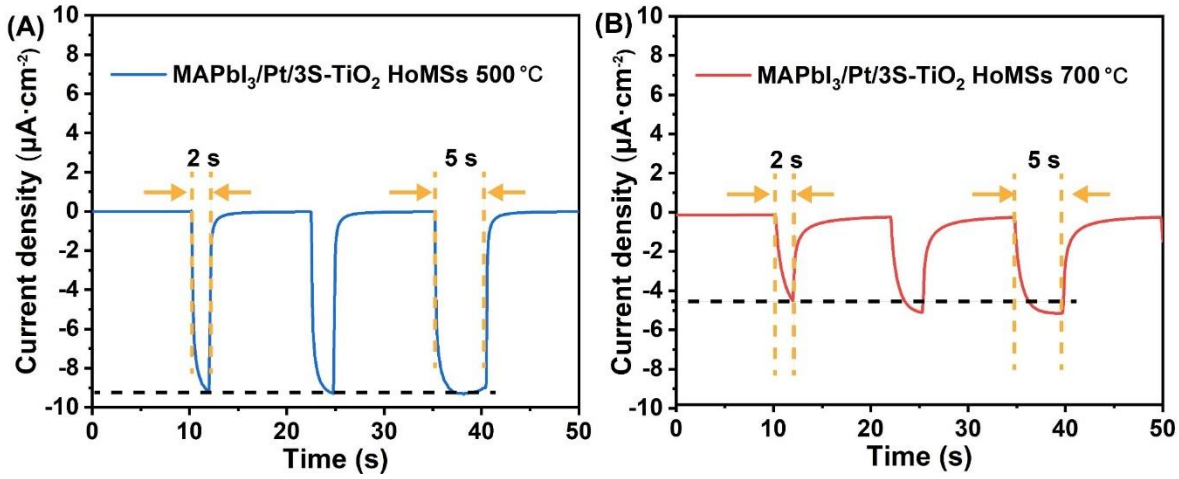

Figure 4.8 Transient photocurrent response curves measured under different illumination times: (A) $MAPbI_3$/Pt/3S-TiO_2 HoMSs-500 °C, and (B) $MAPbI_3$/Pt/3S-TiO_2 HoMSs- 700 °C.

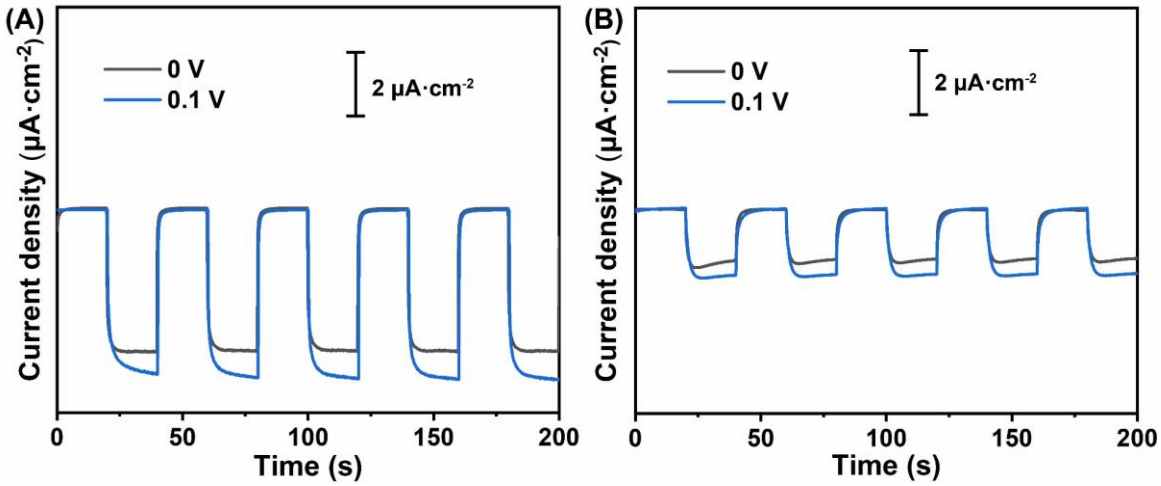

Figure 4.9 Transient photocurrent response curves measured under different voltage biases: (A) $MAPbI_3$/Pt/3S-TiO_2 HoMSs-500 °C, and (B) $MAPbI_3$/Pt/3S-TiO_2 HoMSs-700 °C.

The additional electric field can enhance charges separation and transfer of photocatalysts. To compare the electron transferability, the transient photocurrent response curves were measured under different additional voltage biases as shown in figure 4.9. The photocurrent density under light illumination increases as the additional voltage bias increases. However, the increment of $MAPbI_3$/Pt/3S-TiO_2 HoMSs-500 °C from 0 V to 0.1 V is larger than the increment of $MAPbI_3$/Pt/3S-TiO_2 HoMSs-700 °C. The almost photocurrent increment (1 $\mu A \cdot cm^{-2}$) of $MAPbI_3$/Pt/3S-TiO_2 HoMSs-500 °C indicates higher charges separation efficiency.[196, 198] Hence, the larger increment proves better electrons transferability of $MAPbI_3$/Pt/anatase.

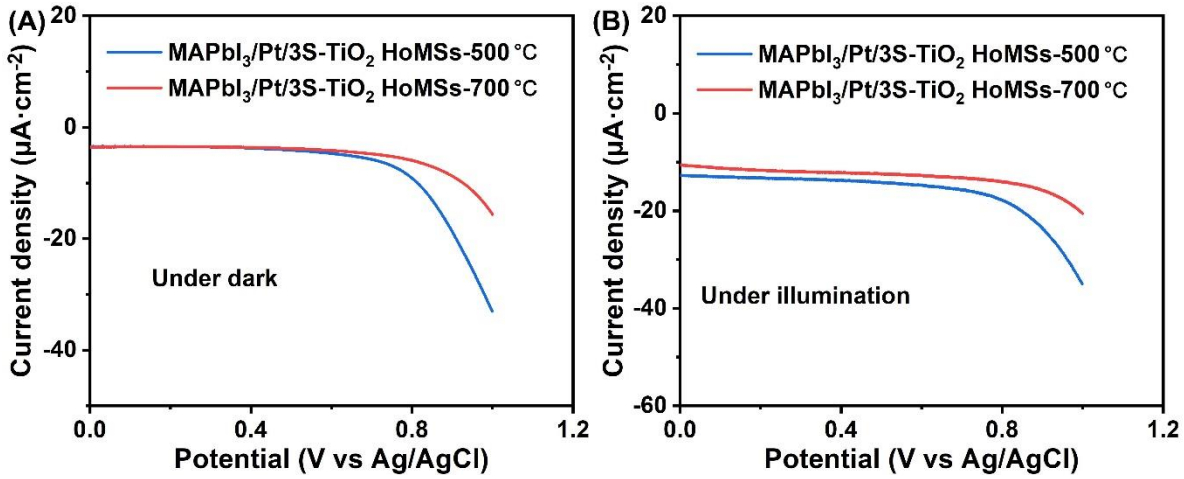

Figure 4.10 Linear sweep voltammetry curves of $MAPbI_3$/Pt/3S-TiO_2 HoMSs: (A) under dark condition, and (B) under illumination condition.

To compare the onset potential of samples, linear sweep voltammetry curves were carried out in figure 4.10. As the applied potential bias increases, the photocurrent also increases. When tested in the dark as shown in figure 4.10A, the onset potential of $MAPbI_3$/Pt/3S-TiO_2 HoMSs-500 °C is smaller than $MAPbI_3$/Pt/3S-TiO_2 HoMSs-700 °C. Smaller onset potential indicates better catalyzing photocatalytic HER kinetics.[149, 169, 199] When tested under illumination as shown in figure 4.10B, the sample of $MAPbI_3$/Pt/3S-TiO_2 HoMSs-500 °C presents higher photocurrent density than $MAPbI_3$/Pt/3S-TiO_2 HoMSs-700 °C. Higher photocurrent density means better effective electrons transfer and separation.[194, 200-202] Hence, the anatase bulk transfer with a fast electron migration rate shows better electrons transportability when electrons transfer from $MAPbI_3$ bulk to reaction sites.

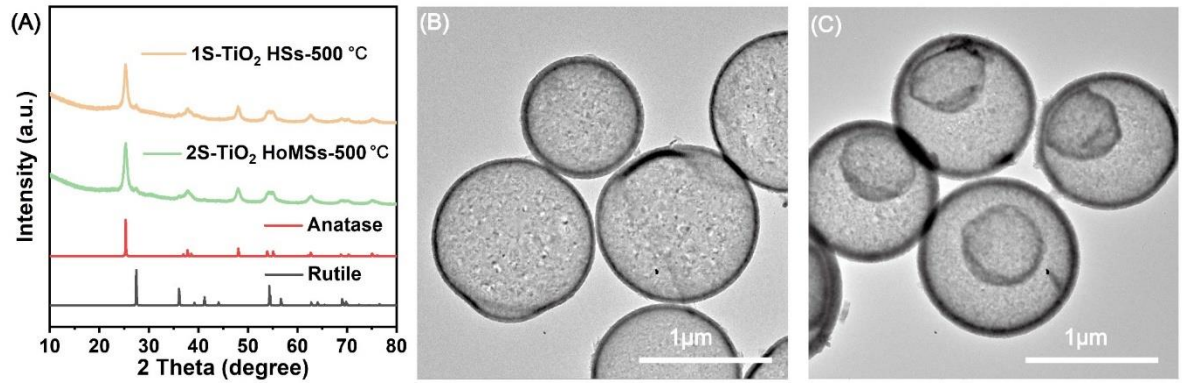

Figure 4.11 (A) XRD patterns of 1S-TiO_2 HSs and 2S-TiO_2 HoMSs, The TEM images of (B) 1S-TiO_2 HSs, and (C) 2S-TiO_2 HoMSs.

To confirm anatase with a positive role in photocatalytic, the 1S-TiO_2 HSs and 2S-TiO_2 HoMSs calcined at 500 °C were synthesized. The corresponding XRD and TEM results are

shown in figure 4.11. According to the calculation formula 2.1, the weight fraction of rutile, the weight fractions of anatase are 90.5 % and 90.2 % for 1S-TiO_2 HSs and 2S-TiO_2 HoMSs respectively. The TEM images show similar morphology compared with TiO_2 HoMSs calcined at 550 °C in chapter 2. The synthesis method of $MAPbI_3$/Pt/TiO_2 composite was consistent with chapter 2. And the corresponding TEM results of $MAPbI_3$/Pt/TiO_2 composite in figure 4.12 is no obvious difference in morphology.

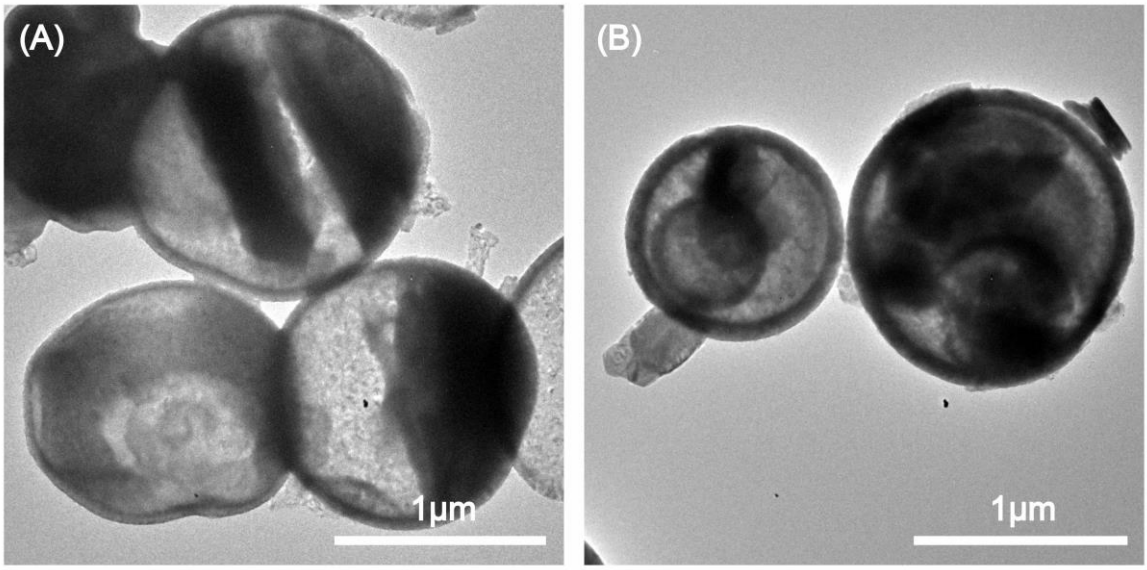

Figure 4.12 TEM images of (A) $MAPbI_3$/Pt/1S-TiO_2 HSs-500 °C and (B) $MAPbI_3$/Pt/2S-TiO_2 HoMSs-500 °C.

To compare the photocatalytic performance of $MAPbI_3$/Pt/TiO_2 HoMSs-500 °C with different shells, the conditions of all tests were the same as before. The photocatalytic performances of $MAPbI_3$/Pt/1S-TiO_2 HSs-500 °C and $MAPbI_3$/Pt/2S-TiO_2 HoMSs-500 °C are 424.47 μmol and 706.54 μmol after reacting 3 hours as shown in figure 4.13. These photocatalytic performances are higher than $MAPbI_3$/Pt/TiO_2 HoMSs with TiO_2 calcined at 550 °C in chapter 3. Photocatalysts with a higher ratio of anatase have better catalytic performance. On the other hand, the sample of $MAPbI_3$/Pt/2S-TiO_2 HoMSs-500 °C is around 30 μmol more than $MAPbI_3$/Pt/1S-TiO_2 HSs-500 °C per half hour. And the increment for both catalysts is relatively a constant which indicates good photocatalytic stability. The performances of $MAPbI_3$/Pt/TiO_2 HoMSs with TiO_2 HoMSs calcined at 500 °C and 550 °C were calculated as shown in figure 4.13B. The performance of photocatalysts with TiO_2 HoMSs calcined at 500 °C shows a higher photocatalytic performance, suggesting anatase TiO_2 enhances photocatalytic performance.

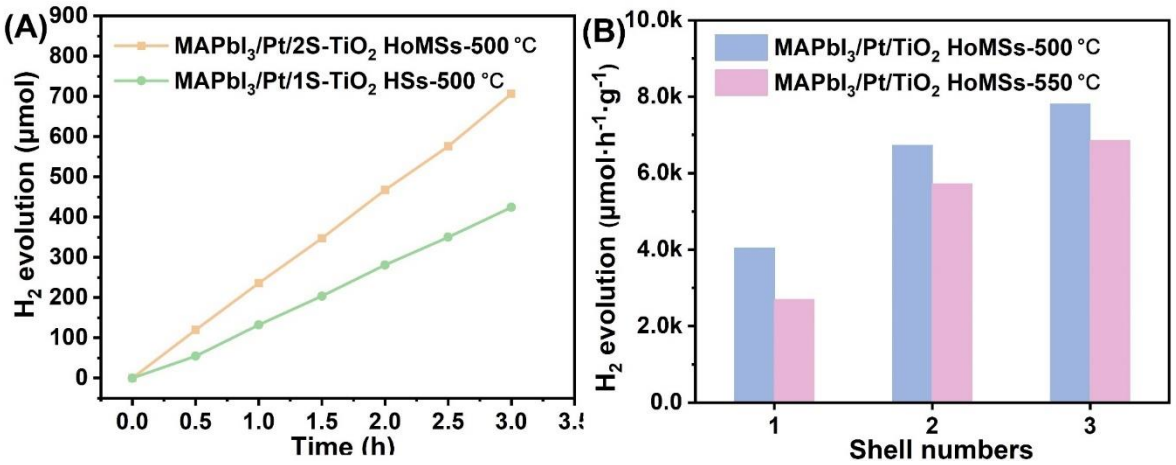

Figure 4.13 (A) The photocatalytic performance of $MAPbI_3/Pt/TiO_2$ HoMSs-500 °C; (B) The performance of $MAPbI_3/Pt/TiO_2$ HoMSs with TiO_2 HoMSs calcined at 500 °C and 550 °C.

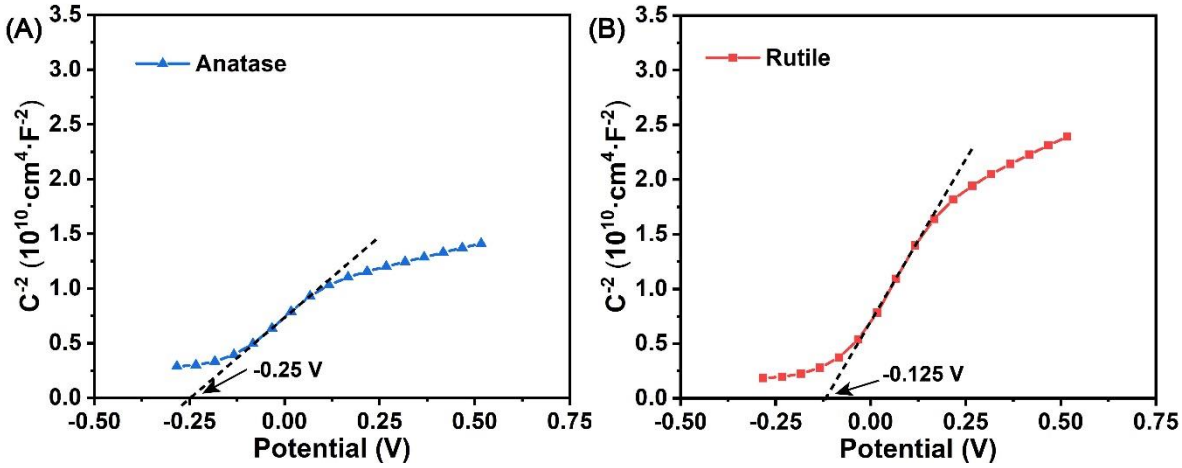

Figure 4.14 Mott-Schottky curves of 3S-TiO_2 HoMSs measured at 1000 Hz: (A) 500 °C, (B) 700 °C.

To confirm the band diagram affected by anatase and rutile, the Mott-Schottky curves of 3S-TiO_2 HoMSs were measured as shown in figure 4.14. The potential of the conduction band of 3S-TiO_2 HoMSs-500 °C is 0.25 V (vs. NHE) and the potential of the conduction band of 3S-TiO_2 HoMSs-700 °C is 0.125 V (vs. NHE). Both potentials are approximate with reported literatures of anatase and rutile respectively. According to the UPS date of $MAPbI_3$ in chapter 3, the schematic energy band diagram was constructed in figure 4.15. The photocatalysts with a more negative CB potential present stronger hydrogen reduction ability. Comparing both TiO_2 HoMSs calcined at 500 °C and 700 °C, the CB potential (vs. NHE) of anatase is closer to the CB potential (vs. NHE) of $MAPbI_3$.

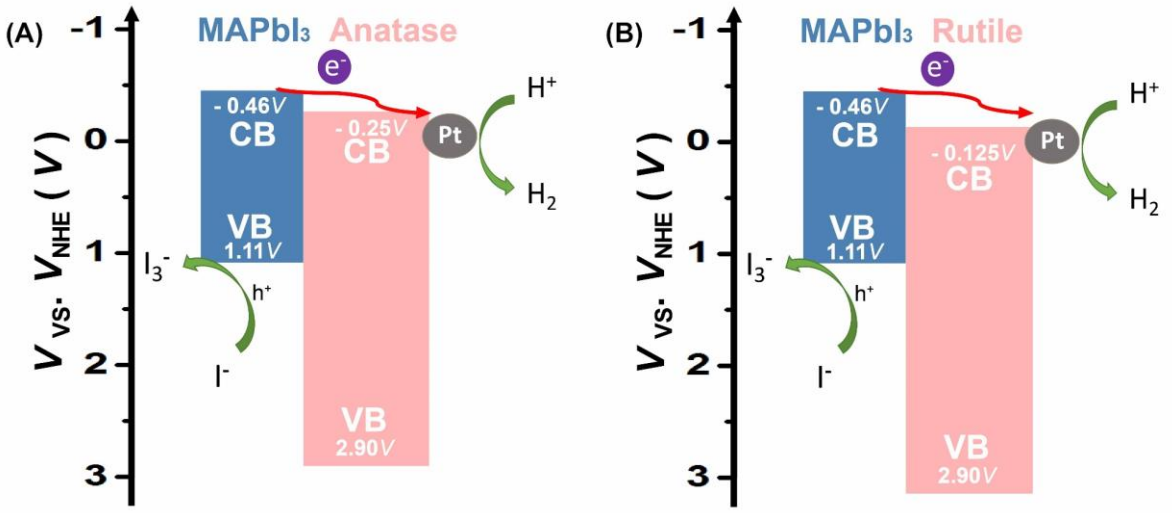

Figure 4.15 Schematic energy band diagram of the $MAPbI_3/Pt/TiO_2$ photocatalysts with (A) TiO_2 in anatase phase and (B) TiO_2 in rutile phase.

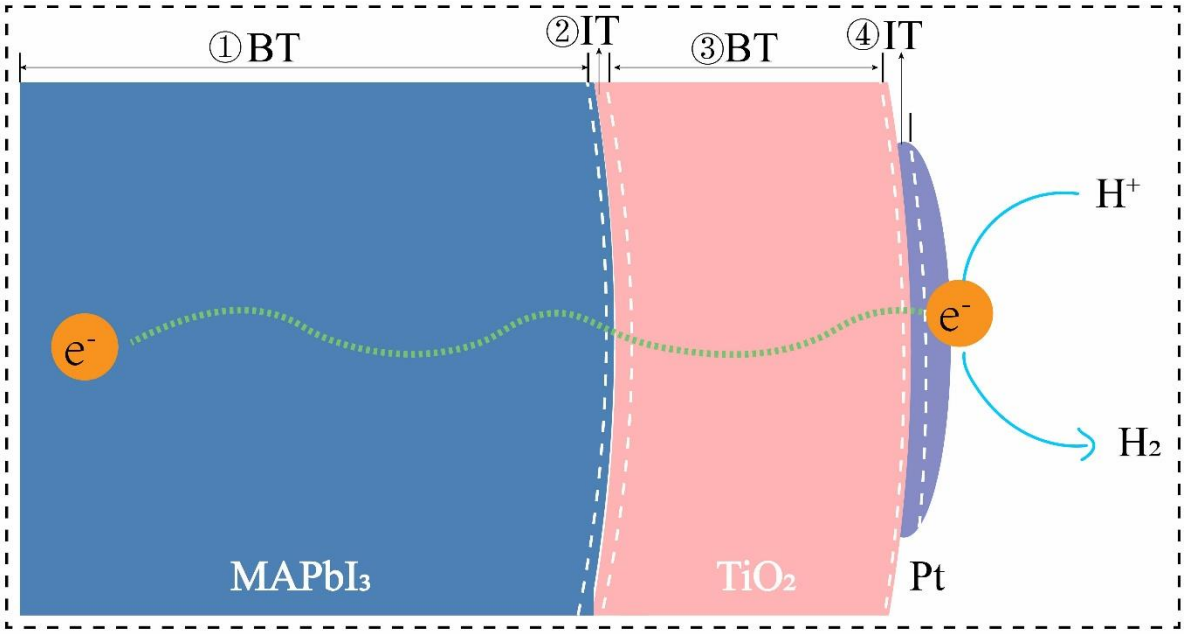

Figure 4.16 Schematic electrons transfer pathways from $MAPbI_3$ to reaction sites, including bulk transfer (BT) and interface transfer (IT).

The photogenerated electrons transport pathways of photocatalyst are supposed as shown in figure 4.16. In the first, the photogenerated electrons are transferred from the bulk inside to the crystal surface after light irradiation. Second, the electrons are extracted through heterogeneous interfaces between $MAPbI_3$ and TiO_2. Then, the electrons through TiO_2 bulk transfer from the inner side to the outside. In the end, the electrons are transferred into the cocatalyst surface and then taking HER process. In this chapter, the first step of bulk transfer

is assumed as no difference between photocatalysts because of the same perovskite materials. Besides, the photocurrent response curves of $MAPbI_3/TiO_2$ HoMSs-500 °C with stronger electrons transfer ability indicate the transport of electrons in $MAPbI_3$/anatase TiO_2 is faster than $MAPbI_3$/rutile TiO_2. According to the above results of the photoelectric test, the interfacial electrons transfer of $MAPbI_3$ and rutile TiO_2 HoMSs is not a determinant. Although the interfaces of $MAPbI_3$/rutile TiO_2 in perovskite solar cells exhibit the good extraction ability of electrons, $MAPbI_3$/anatase interfaces show a better photocatalytic reactivity. Hence, electrons transfer in TiO_2 bulk transfer with faster electron mobility affects largely photocatalytic efficiency more obviously.

4.5 Conclusions

The different anatase/rutile ratio of TiO_2 HoMSs was successfully synthesized through turning calcination temperature. As the calcined temperatures increase, the phase ratio of rutile TiO_2 is gradually increasing. The photocatalytic HER performance results show that the $MAPbI_3/Pt/TiO_2$ HoMSs with a higher proportion of anatase presents better performance instead of the photocatalysts with traditional anatase/rutile phase ratio 4:1. The electrons separation and transferability were characterized by EIS and transient photocurrent response. Compared with $MAPbI_3$/Pt/rutile, $MAPbI_3$/Pt/anatase has smaller electrons transfer resistance and better electrons transfer capability. The electrons transfer in TiO_2 bulk transfer with faster electron mobility may affect photocatalytic efficiency more obviously.

CHAPTER 5.

Conclusions and Future Prospects

5.1 Conclusions

In the context of energy shortages, preparation of hydrogen clean energy by photocatalysis was researched in this thesis. The $MAPbI_3/Pt/TiO_2$ HoMSs composites were synthesized in chapter 2 and applied in photocatalytic HER in chapter 3. The heterogeneous interface between $MAPbI_3$ and TiO_2 HoMSs was proved to be an efficient method for enhancing charges separation and utilization. The application of hollow multi-shelled structures in the photocatalytic field possesses outstanding advantages, such as light absorption, charges separation and transfer. In chapter 4, the different phase ratios of anatase TiO_2 and rutile TiO_2 were synthesized through different calcination temperatures. The specific research content is as follows:

Chapter 2 focuses on the synthesis and control of TiO_2 HoMSs. The CMSs pretreated by ethanol with different washing times were chosen as templates to adsorb titanium precursor solution. The TEM results indicate that the pretreated CMSs as the template can obtain more shells of TiO_2 HoMSs when extending the pretreatment time. The SEM results indicate the size of pores increases gradually when extending the pretreatment time. In addition, the FT-IR and Zeta potential results show functional groups of CMSs remain unchanged when extending pretreatment time. The experiments on the duration time of adsorption and heating rate are carried out in this chapter. In the end, obtained TiO_2 HoMSs samples are characterized by XRD, SEM, TEM, Raman, SAED, HRTEM, and XPS. The results show that TiO_2 HoMSs is the mixed-phase (W_{Ana}:W_{Rut} =4:1) with good crystallinity. The synthesis of $MAPbI_3/Pt/TiO_2$ HoMSs materials by impregnation method. Samples characterized by XRD, TEM, elemental mappings, and line scan proves that $MAPbI_3/Pt/TiO_2$ HoMSs has been successfully synthesized.

Chapter 3 focuses on the application of $MAPbI_3/Pt/TiO_2$ HoMSs in photocatalytic HER. The bandgap and conduction band of $MAPbI_3$ and 3S-TiO_2 HoMSs were confirmed by UPS and Tauc-plots. The PL and PL decay results indicate that the heterogenous interface of

$MAPbI_3/TiO_2$ HoMSs can efficiently promote the separation of photogenerated carriers. Thanks to the thin shell structure, it can also reduce the transmission distance of the carriers to repress the charge recombination and improve the charge utilization. Additionally, HoMSs assembled with multiple shells can support abundant available surfaces for building heterogeneous interfaces and photocatalytic reactions. As a result, samples of $MAPbI_3$/triple-shelled TiO_2 hollow structure displayed an H_2 evolution rate of 6856.2 μmol h^{-1} g^{-1} under visible light irradiation, which is much faster than that of barely $MAPbI_3$ (268.6 μmol h^{-1} g^{-1}). The interfacial photogenerated charge separation and transport have demonstrated great influence on photocatalytic performance.

Chapter 4 focuses on the effect of different anatase/rutile ratios of TiO_2 HoMSs on the photocatalytic performance of $MAPbI_3/Pt/TiO_2$ HoMSs composite. A higher proportion of rutile in TiO_2 HoMSs was obtained successfully through turning calcination temperature at 700 °C. Compared with the performance of the higher proportion of rutile (510.03 μmol), the $MAPbI_3/Pt/TiO_2$ HoMSs with the higher proportion of anatase presents better performance (819.43 μmol). The EIS and transient photocurrent response curves prove that electrons transfer in $MAPbI_3$/anatase is faster than $MAPbI_3$/rutile. In addition, compared with $MAPbI_3$/Pt/rutile, $MAPbI_3$/Pt/anatase has smaller electrons transfer resistance and better electronic transfer capability. The electrons mobility of anatase may improve the electrons transfer.

5.2 Future Prospects

In this thesis, the TiO_2 HoMSs and $MAPbI_2/Pt/TiO_2$ HoMSs were successfully synthesized and applied to photocatalytic hydrogen evolution. The experiment results show an outstanding HER activity and provide an effective design strategy for photocatalytic. In this section, the prospects based on the above results are proposed as follows.

1. Co-catalyst existed in a type of single atom. The Co-catalyst is loaded on the surface of photocatalysts to accelerate charges separation and the surface chemical reaction. In this thesis, the Pt was loaded as clusters by the photoreduction method. The catalysts with the single atom present wonderful catalytic activity and lower economic cost, especially in the noble metal. hence, the single atom strategy of noble metal or non-noble metal is worthy to further study.

2. The composition of HoMSs. The heterojunctions are effective in promoting charges separation and reasonable band position for photocatalytic redox reaction. Based on the

HoMSs structure in this thesis, the heterogeneous composition in one shell is beneficial for charges separation in perovskite sensitizer. One kind of composition extract photogenerated electrons which participate in the hydrogen reduction reaction. Another kind of composition extracts holes from perovskite sensitizer. The dual charges separation pathways depress the recombination of electrons and holes.

3. The stability of perovskite sensitizer in water. The present photocatalysts in this thesis are applied in perovskite saturated HI:H_3PO_2 solution. Despite the high photocatalytic activity of photocatalysts, the further application of hybrid perovskite in pure water is impossible for now. Hence, improving the stability of hybrid perovskite in pure water requires further study. The improving strategies include packaging by polymer semiconductor or inorganic materials, modification, or doping.

4. New photocatalysts. The new photocatalysts with reasonable conduction band and bandgap are needed to find. The reasonable bandgap can absorb visible light with a wavelength range of 400-800 nm. The bandgap also needs to be bigger than the chemical potential of overall water splitting (1.23 eV). Compared with hydrogen reduction potential, the reasonable conduction band needs more negative. And the valence band is required more positive than oxygen oxidation potential.

5. Recently, the photocatalytic water splitting efficiency is not enough for the actual application. The water splitting efficiency of photo-electro catalysis maybe meets the requirement of the market. The electrolysis of water is recognized as the main part of a synergetic system. Photocatalytic water splitting is mainly used to decrease electric power consumption.

Acknowledgments

When the thesis is written here, I realize that my doctoral study career is coming to an end. Back in the autumn of 2019, I entered Gunma University and Institute of Process Engineering, Chinese Academy of Sciences, and started my doctoral study. In just a few years, a lot of things happened, both happy and sad. The COVID-19 outbreak, which occurred in the first year of my Ph.D., brought great inconvenience to our lives. In the second year of my Ph.D., I married the man I loved. In the third year of my Ph.D., my daughter was born. I believe that these three years are also my fastest-growing three years.

First of all, I would like to thank my supervisors, professor Dan Wang, professor Nobuyoshi Nakagawa, and professor Jiawei Wan. Most of all, I would like to thank prof. Wang for allowing me to join the research group and providing me the opportunity to learn and contact with a high-quality scientific research platform. During the three years of my doctorate, no matter how difficult my experiments were and how dissatisfied prof. Wang was, Mr. Wang never gave up on me. Thank prof. Wang for his help all the time. His profound knowledge, rigorous attitude, and hard spirit will affect and accompany me all my life. Professor Nobuyoshi Nakagawa provided me with the opportunity to study in Japan. When I have a problem sending him an email, he is always the first to reply to me and give me much useful advice. His views inspired me to be more inventive with my research. Besides, thank Prof. Nakagawa for help in my Ph.D. application. Professor Jiawei Wan participated in my experiment design and analysis. Thank professor Wan for his care and help in work and life.

Thank Professor Guanghui Ma for Building a China-Japan exchange learning opportunity.

Thank Akihiko Yamagishi in the charge of academic affairs in the faculty of science and technology, Yanlin Lv in the institute of process and engineering, for their timely notifications and help in my student affairs.

I would like to thank laboratory members, Prof. Naliang Yang, Prof. Jiangyan Wang, Yanze Wei, Jiang Du, Dan Mao, Yang Mei, Xu Nan, Quan Jin, Jian Qi, Lijuan Zhang, Zumin Wang in this research group. I would like to thank all teachers for their help and concern in my experiment and life. Thanks to the students of the research group: Yujing Zhu, Yasong Zhao, Huang Wang, Zijian Wang, Jilu Zhao, Feifei, You, Decai Zhao, Li Wang, Xuanbo Chen, Shuhui Zhan, Hou Ping, Peng Wei, Peng Wang, Leikai Xu, Ruyi Bi, Yingjian Ma, Wei Xu,

Xiaofan Hou, Fengmei Su, Jiao Wang, Lei Zhang, Tianye Huang, Hui Wang, Xiaolang Zhao, Juan Li, Di Li, Dan Yu, Yuan Feng, Qian Xiao, Yiping Cheng, Caini Huang, Yilei He and other students. With the accompany of these students, the boring experimental life becomes more colorful and vivid.

I want to thank my parents, wife, brothers, sisters, and lovely baby sincerely. Thank my parents for giving me life and raising me with countless care. Thank my wife, Sally Chen, for taking care of me with patience, understanding, and support. Thank brothers and sisters for helping solve every problem in my life. Thank my cute baby for coming into my life.

Finally, I would like to give many thanks to the member of the review committee, in which the specialists give me a lot of precious comments. The members of the review committee are as follows:

Professor Shinichi Kuroda, Gunma Univ.
Professor Junichi Ozaki, Gunma Univ.
Associate Professor, Hideyuki Morimoto, Gunma Univ.
Professor Dan Wang, Institute of Process and Engineering, Chinese Academy of Sciences.
Professor Nobuyoshi Nakagawa, Gunma Univ.

References

1. Guney, M. S., Solar power and application methods. *Renewable and Sustainable Energy Reviews,* **2016,** *57*, 776-785.

2. Berardi, S.; Drouet, S.; Francas, L.; Gimbert-Surinach, C.; Guttentag, M.; Richmond, C.; Stoll, T.; Llobet, A., Molecular artificial photosynthesis. *Chemical Society Review,* **2014,** *43* (22), 7501-7519.

3. Yang, X.; Wang, D., Photocatalysis: from fundamental principles to materials and applications. *ACS Applied Energy Materials,* **2018,** *1* (12), 6657-6693.

4. House, J. E.; House, K. A., Hydrogen. In *Descriptive Inorganic Chemistry,* 2016; pp 111-121.

5. Fujishima, A.; Honda, K., Electrochemical photolysis of water at a semiconductor electrode. *Nature,* **1972,** *238* (5358), 37-38.

6. Walter, M. G.; Warren, E. L.; McKone, J. R.; Boettcher, S. W.; Mi, Q.; Santori, E. A.; Lewis, N. S., Correction to Solar Water Splitting Cells. *Chemical Reviews* **2011,** *111* (9), 5815-5815.

7. Chen, S.; Takata, T.; Domen, K., Particulate photocatalysts for overall water splitting. *Nature Reviews Materials,* **2017,** *2* (10), 17050.

8. Chen, X.; Shen, S.; Guo, L.; Mao, S. S., Semiconductor-based photocatalytic hydrogen generation. *Chemical Reviews,* **2010,** *110* (11), 6503-6570.

9. Wang, Q.; Domen, K., Particulate photocatalysts for light-driven water splitting: mechanisms, challenges, and design strategies. *Chemical Reviews,* **2020,** *120* (2), 919-985.

10. Chun, W. J.; Ishikawa, A.; Fujisawa, H.; Takata, T.; Kondo, J. N.; Hara, M.; Kawai, M.; Matsumoto, Y.; Domen, K., Conduction and valence band positions of Ta_2O_5, TaON, and Ta_3N_5 by UPS and electrochemical methods. *The Journal of Physical Chemistry B,* **2003,** *107* (8), 1798-1803.

11. Fujito, H.; Kunioku, H.; Kato, D.; Suzuki, H.; Higashi, M.; Kageyama, H.; Abe, R., Layered perovskite oxychloride Bi_4NbO_8Cl: a stable visible light responsive photocatalyst for water splitting. *Journal of the American Chemical Society,* **2016,** *138* (7), 2082-2085.

12. Zuo, F.; Wang, L.; Wu, T.; Zhang, Z.; Borchardt, D.; Feng, P., Self-doped Ti^{3+} enhanced photocatalyst for hydrogen production under visible light. *Journal of the American Chemical Society,* **2010,** *132* (34), 11856-7.

13. Niishiro, R.; Kato, H.; Kudo, A., Nickel and either tantalum or niobium-codoped TiO_2 and $SrTiO_3$ photocatalysts with visible-light response for H_2 or O_2 evolution from aqueous solutions. *Physical Chemistry Chemical Physics,* **2005,** *7* (10), 2241-2245.

14. Suzuki, H.; Tomita, O.; Higashi, M.; Abe, R., Design of nitrogen-doped layered tantalates for non-sacrificial and selective hydrogen evolution from water under visible light. *Journal of Materials Chemistry A,* **2016,** *4* (37), 14444-14452.

15. Maeda, K.; Takata, T.; Hara, M.; Saito, N.; Inoue, Y.; Kobayashi, H.; Domen, K., GaN:ZnO solid solution as a photocatalyst for visible-light-driven overall water splitting. *Journal of the American Chemical Society,* **2005,** *127* (23), 8286-8287.

16. Maeda, K.; Domen, K., Solid solution of GaN and ZnO as a stable photocatalyst for overall water splitting under visible light. *Chemistry of Materials,* **2009,** *22* (3), 612-623.

17. Reynal, A.; Palomares, E., Ruthenium polypyridyl sensitisers in dye solar cells based on mesoporous TiO_2. *European Journal of Inorganic Chemistry,* **2011,** *2011* (29), 4509-4526.

18. Hou, W.; Cronin, S. B., A Review of surface plasmon resonance-enhanced photocatalysis. *Advanced Functional Materials,* **2013,** *23* (13), 1612-1619.

19. Holmes, M. A.; Townsend, T. K.; Osterloh, F. E., Quantum confinement controlled photocatalytic water splitting by suspended CdSe nanocrystals. *Chemical Communications,* **2012,** *48* (3), 371-373.

20. She, X.; Wu, J.; Xu, H.; Zhong, J.; Wang, Y.; Song, Y.; Nie, K.; Liu, Y.; Yang, Y.; Rodrigues, M.-T. F.; Vajtai, R.; Lou, J.; Du, D.; Li, H.; Ajayan, P. M., High efficiency photocatalytic water splitting using 2D α-Fe_2O_3/g-C_3N_4 Z-scheme catalysts. *Advanced Energy Materials,* **2017,** *7* (17), 1700025.

21. Pan, Z.; Zhang, G.; Wang, X., Polymeric carbon nitride/reduced graphene oxide/Fe_2O_3: all-solid-state Z-scheme system for photocatalytic overall water splitting. *Angewandte Chemie International Edtion,* **2019,** *58* (21), 7102-7106.

22. Iwase, A.; Ng, Y. H.; Ishiguro, Y.; Kudo, A.; Amal, R., Reduced graphene oxide as a solid-state electron mediator in Z-scheme photocatalytic water splitting under visible light. *Journal of the American Chemical Society,* **2011,** *133* (29), 11054-11057.

23. Banerjee, S.; Pillai, S. C.; Falaras, P.; O'Shea, K. E.; Byrne, J. A.; Dionysiou, D. D., New insights into the mechanism of visible light photocatalysis. *Journal of Physical Chemistry Letters,* **2014,** *5* (15), 2543-2554.

24. Lin, H.; Maggard, P. A., Copper(I)-rhenate hybrids: syntheses, structures, and optical properties. *Inorganic Chemistry,* **2007,** *46* (4), 1283-1290.

25. Adeli, B.; Taghipour, F., A review of synthesis techniques for gallium-zinc oxynitride solar-activated photocatalyst for water splitting. *ECS Journal of Solid State Science and Technology,* **2013,** *2* (7), 118-126.

26. O'Regan, B.; Grätzel, M., A low-cost, high-efficiency solar cell based on dye-sensitized colloidal TiO_2 films. *Nature,* **1991,** *353* (6346), 737-740.

27. Ghosh, S. K.; Nath, S.; Kundu, S.; Esumi, K.; Pal, T., Solvent and ligand effects on the

localized surface plasmon resonance (LSPR) of gold colloids. *The Journal of Physical Chemistry B,* **2004,** *108* (37), 13963-13971.

28. Zhou, P.; Yu, J.; Jaroniec, M., All-solid-state Z-scheme photocatalytic systems. *Advanced Materials,* **2014,** *26* (29), 4920-4935.

29. Maeda, K., Z-scheme water splitting using two different semiconductor photocatalysts. *ACS Catalysis,* **2013,** *3* (7), 1486-1503.

30. Hu, J.; He, H.; Li, L.; Zhou, X.; Li, Z.; Shen, Q.; Wu, C.; Asiri, A. M.; Zhou, Y.; Zou, Z., Highly symmetrical, 24-faceted, concave $BiVO_4$ polyhedron bounded by multiple high-index facets for prominent photocatalytic O_2 evolution under visible light. *Chemical Communications,* **2019,** *55* (33), 4777-4780.

31. Long, R.; Li, Y.; Liu, Y.; Chen, S.; Zheng, X.; Gao, C.; He, C.; Chen, N.; Qi, Z.; Song, L.; Jiang, J.; Zhu, J.; Xiong, Y., Isolation of Cu atoms in Pd lattice: forming highly selective sites for photocatalytic conversion of CO_2 to CH_4. *Journal of the American Chemical Society,* **2017,** *139* (12), 4486-4492.

32. Zhou, X.; Dong, H., A theoretical perspective on charge separation and transfer in metal oxide photocatalysts for water splitting. *ChemCatChem,* **2019,** *11* (16), 3688-3715.

33. Zhang, G.; Li, G.; Heil, T.; Zafeiratos, S.; Lai, F.; Savateev, A.; Antonietti, M.; Wang, X., Tailoring the grain boundary chemistry of polymeric carbon nitride for enhanced solar hydrogen production and CO_2 reduction. *Angewandte Chemie International Edtion,* **2019,** *58* (11), 3433-3437.

34. Yang, J.; Wang, D.; Han, H.; Li, C., Roles of cocatalysts in photocatalysis and photoelectrocatalysis. *Accounts of Chemical Research,* **2013,** *46* (8), 1900-1909.

35. Wei, Y.; Wan, J.; Wang, J.; Zhang, X.; Yu, R.; Yang, N.; Wang, D., Hollow multishelled structured $SrTiO_3$ with La/Rh Co-doping for enhanced photocatalytic water splitting under visible light. *Small,* **2021,** *17* (22), e2005345.

36. Tu, W.; Guo, W.; Hu, J.; He, H.; Li, H.; Li, Z.; Luo, W.; Zhou, Y.; Zou, Z., State-of-the-art advancements of crystal facet-exposed photocatalysts beyond TiO_2: Design and dependent performance for solar energy conversion and environment applications. *Materials Today,* **2020,** *33*, 75-86.

37. Bai, S.; Yang, L.; Wang, C.; Lin, Y.; Lu, J.; Jiang, J.; Xiong, Y., Boosting photocatalytic water splitting: interfacial charge polarization in atomically controlled core-shell cocatalysts. *Angewandte Chemie International Edtion,* **2015,** *54* (49), 14810-14814.

38. Jiang, J.; Zhao, K.; Xiao, X.; Zhang, L., Synthesis and facet-dependent photoreactivity of BiOCl single-crystalline nanosheets. *Journal of the American Chemical Society,* **2012,** *134* (10), 4473-4476.

39. Yanagi, R.; Zhao, T.; Solanki, D.; Pan, Z.; Hu, S., Charge separation in photocatalysts:

mechanisms, physical parameters, and design principles. *ACS Energy Letters,* **2021,** *7* (1), 432-452.

40. Fu, G.; Yan, S.; Yu, T.; Zou, Z., Oxygen related recombination defects in Ta_3N_5 water splitting photoanode. *Applied Physics Letters,* **2015,** *107* (17), 171902.

41. Wu, P.; Wang, J.; Zhao, J.; Guo, L.; Osterloh, F. E., Structure defects in g-C_3N_4 limit visible light driven hydrogen evolution and photovoltage. *Journal of Materials Chemistry A,* **2014,** *2* (47), 20338-20344.

42. Lai, Z.; Chaturvedi, A.; Wang, Y.; Tran, T. H.; Liu, X.; Tan, C.; Luo, Z.; Chen, B.; Huang, Y.; Nam, G. H.; Zhang, Z.; Chen, Y.; Hu, Z.; Li, B.; Xi, S.; Zhang, Q.; Zong, Y.; Gu, L.; Kloc, C.; Du, Y.; Zhang, H., Preparation of 1T'-Phase $ReS_{2x}Se_2(1-x)$ (x = 0-1) nanodots for highly efficient electrocatalytic hydrogen evolution reaction. *Journal of the American Chemical Society,* **2018,** *140* (27), 8563-8568.

43. Díaz, L.; Rodríguez, V. D.; González-Rodríguez, M.; Rodríguez-Castellón, E.; Algarra, M.; Núñez, P.; Moretti, E., M/TiO_2 (M = Fe, Co, Ni, Cu, Zn) catalysts for photocatalytic hydrogen production under UV and visible light irradiation. *Inorganic Chemistry Frontiers,* **2021,** *8* (14), 3491-3500.

44. Li, Z.; Klein, T. R.; Kim, D. H.; Yang, M.; Berry, J. J.; van Hest, M. F. A. M.; Zhu, K., Scalable fabrication of perovskite solar cells. *Nature Reviews Materials,* **2018,** *3* (4), 18017.

45. Xiao, M.; Wang, Z.; Lyu, M.; Luo, B.; Wang, S.; Liu, G.; Cheng, H. M.; Wang, L., Hollow nanostructures for photocatalysis: advantages and challenges. *Advanced Materials,* **2019,** *31* (38), e1801369.

46. Su, T.; Qin, Z.; Ji, H.; Wu, Z., An overview of photocatalysis facilitated by 2D heterojunctions. *Nanotechnology,* **2019,** *30* (50), 502002.

47. Karkas, M. D.; Akermark, B., Water oxidation using earth-abundant transition metal catalysts: opportunities and challenges. *Dalton Transactions,* **2016,** *45* (37), 14421-14461.

48. Pan, L.; Liu, X.; Sun, Z.; Sun, C. Q., Nanophotocatalysts via microwave-assisted solution-phase synthesis for efficient photocatalysis. *Journal of Materials Chemistry A,* **2013,** *1* (29), 8299-8326.

49. Ran, J.; Zhang, J.; Yu, J.; Jaroniec, M.; Qiao, S. Z., Earth-abundant cocatalysts for semiconductor-based photocatalytic water splitting. *Chemical Society Reviews,* **2014,** *43* (22), 7787-7812.

50. Foo, W. J.; Zhang, C.; Ho, G. W., Non-noble metal Cu-loaded TiO_2 for enhanced photocatalytic H_2 production. *Nanoscale,* **2013,** *5* (2), 759-764.

51. Wu, N., Enhanced TiO_2 photocatalysis by Cu in hydrogen production from aqueous methanol solution. *International Journal of Hydrogen Energy,* **2004,** *29* (15), 1601-1605.

52. Abe, R.; Sayama, K.; Arakawa, H., Significant effect of iodide addition on water splitting

into H_2 and O_2 over Pt-loaded TiO_2 photocatalyst: suppression of backward reaction. *Chemical Physics Letters,* **2003,** *371* (3-4), 360-364.

53. Sayama, K.; Arakawa, H., Effect of carbonate salt addition on the photocatalytic decomposition of liquid water over Pt-TiO_2 catalyst. *Journal of the Chemical Society-Faraday Transactions,* **1997,** *93* (8), 1647-1654.

54. Yi, J.; El-Alami, W.; Song, Y.; Li, H.; Ajayan, P. M.; Xu, H., Emerging surface strategies on graphitic carbon nitride for solar driven water splitting. *Chemical Engineering Journal,* **2020,** *382*, *122812*.

55. Kageshima, Y.; Gomyo, Y.; Matsuoka, H.; Inuzuka, H.; Suzuki, H.; Abe, R.; Teshima, K.; Domen, K.; Nishikiori, H., Z-scheme overall water splitting using $Zn_xCd_{1-x}Se$ particles coated with metal cyanoferrates as hydrogen evolution photocatalysts. *ACS Catalysis,* **2021,** *11* (13), 8004-8014.

56. Lawley, C.; Nachtegaal, M.; Stahn, J.; Roddatis, V.; Dobeli, M.; Schmidt, T. J.; Pergolesi, D.; Lippert, T., Examining the surface evolution of $LaTiO_xN_y$ an oxynitride solar water splitting photocatalyst. *Nature Communications,* **2020,** *11* (1), 1728.

57. Takata, T.; Pan, C.; Nakabayashi, M.; Shibata, N.; Domen, K., Fabrication of a core-shell-type photocatalyst via photodeposition of group IV and V transition metal oxyhydroxides: an effective surface modification method for overall water splitting. *Journal of the American Chemical Society,* **2015,** *137* (30), 9627-9634.

58. Low, J.; Yu, J.; Jaroniec, M.; Wageh, S.; Al-Ghamdi, A. A., Heterojunction photocatalysts. *Advanced Materials,* **2017,** *29* (20), 1601694.

59. Ge, M.; Cao, C.; Huang, J.; Li, S.; Chen, Z.; Zhang, K.-Q.; Al-Deyab, S. S.; Lai, Y., A review of one-dimensional TiO_2 nanostructured materials for environmental and energy applications. *Journal of Materials Chemistry A,* **2016,** *4* (18), 6772-6801.

60. Zhong, Y.; Peng, C.; He, Z.; Chen, D.; Jia, H.; Zhang, J.; Ding, H.; Wu, X., Interface engineering of heterojunction photocatalysts based on 1D nanomaterials. *Catalysis Science & Technology,* **2021,** *11* (1), 27-42.

61. Zhang, J.; Qiao, S. Z.; Qi, L.; Yu, J., Fabrication of NiS modified CdS nanorod p-n junction photocatalysts with enhanced visible-light photocatalytic H_2-production activity. *Physical Chemistry Chemical Physics,* **2013,** *15* (29), 12088-12094.

62. Su, T.; Shao, Q.; Qin, Z.; Guo, Z.; Wu, Z., Role of interfaces in two-dimensional photocatalyst for water splitting. *ACS Catalysis,* **2018,** *8* (3), 2253-2276.

63. Su, Q.; Li, Y.; Hu, R.; Song, F.; Liu, S.; Guo, C.; Zhu, S.; Liu, W.; Pan, J., Heterojunction photocatalysts based on 2D materials: the role of configuration. *Advanced Sustainable Systems,* **2020,** *4* (9), 2000130.

64. He, Z.; Zhang, J.; Li, X.; Guan, S.; Dai, M.; Wang, S., 1D/2D heterostructured

photocatalysts: from design and unique properties to their environmental applications. *Small,* **2020,** *16* (46), e2005051.

65. Di, J.; Xiong, J.; Li, H.; Liu, Z., Ultrathin 2D photocatalysts: electronic-structure tailoring, hybridization, and applications. *Advanced Materials,* **2018,** *30* (1), 1704548.

66. Lin, B.; Li, H.; An, H.; Hao, W.; Wei, J.; Dai, Y.; Ma, C.; Yang, G., Preparation of 2D/2D g-C_3N_4 nanosheet@$ZnIn_2S_4$ nanoleaf heterojunctions with well-designed high-speed charge transfer nanochannels towards high-efficiency photocatalytic hydrogen evolution. *Applied Catalysis B: Environmental,* **2018,** *220*, 542-552.

67. Ong, W. J.; Shak, K. P. Y., 2D/2D heterostructured photocatalysts: an emerging platform for artificial photosynthesis. *Solar RRL,* **2020,** *4* (8).

68. Mao, D.; Wan, J.; Wang, J.; Wang, D., Sequential templating approach: a groundbreaking strategy to create hollow multishelled structures. *Advacnced Materials* **2019,** *31* (38), e1802874.

69. Wei, Y.; Yang, N.; Huang, K.; Wan, J.; You, F.; Yu, R.; Feng, S.; Wang, D., Steering hollow multishelled structures in photocatalysis: optimizing surface and mass transport. *Advanced Materials,* **2020,** *32* (44), e2002556.

70. Ahn, S. H.; Kim, D. J.; Chi, W. S.; Kim, J. H., Hierarchical double-shell nanostructures of TiO_2 nanosheets on SnO_2 hollow spheres for high-efficiency, solid-state, dye-sensitized solar cells. *Advanced Functional Materials,* **2014,** *24* (32), 5037-5044.

71. Hyung, K.; Yong, K.; Yoon, L.; Wan, L.; Kyungkon, K.; Nam, P.; Nano-embossed hollow spherical TiO_2 as bifunctional material for high-efficiency dye-sensitized solar cells. *Advanced Materials,* **2008,** *20*, 195-199.

72. Wei, Y.; Wang, J.; Yu, R.; Wan, J.; Wang, D., Constructing $SrTiO_3$-TiO_2 heterogeneous hollow multi-shelled structures for enhanced solar water splitting. *Angewandte Chemie International Edtion,* **2019,** *58* (5), 1422-1426.

73. Zheng, D.; Hao, R.; Colin, M. H.; Jiangyan, W.; Ranbo, Y.; Quan, J.; Mei, Y.; Zhudong, H.; Yunfa, C.; Zhiyong T.; Huijun, Z.; Dan, W., Quintuple-shelled SnO_2 hollow microspheres with superior light scattering for high-performance dyesensitized solar cells. *Advanced Materials,* **2014,** *26*, 905-909.

74. Haque, S. A.; Tachibana, Y.; Willis, R. L.; Moser, J. E.; Grätzel, M.; Klug, D. R.; Durrant, J. R., Parameters influencing charge recombination kinetics in dye-sensitized nanocrystalline titanium dioxide films. *The Journal of Physical Chemistry B,* **2000,** *104* (3), 538-547.

75. Chen, B.; Yang, M.; Priya, S.; Zhu, K., Origin of J-V hysteresis in perovskite solar cells. *Journal of Physical Chemistry Letters,* **2016,** *7* (5), 905-917.

76. Lai, X.; Li, J.; Korgel, B. A.; Dong, Z.; Li, Z.; Su, F.; Du, J.; Wang, D., General synthesis and gas-sensing properties of multiple-shell metal oxide hollow microspheres. *Angewandte*

Chemie International Edtion, **2011,** *50* (12), 2738-2741.

77. Ren, H.; Yu, R.; Wang, J.; Jin, Q.; Yang, M.; Mao, D.; Kisailus, D.; Zhao, H.; Wang, D., Multishelled TiO_2 hollow microspheres as anodes with superior reversible capacity for lithium ion batteries. *Nano Letters,* **2014,** *14* (11), 6679-6684.

78. Yi, L.; Liu, Y.; Yang, N.; Tang, Z.; Zhao, H.; Ma, G.; Su, Z.; Wang, D., One dimensional $CuInS_2$–ZnS heterostructured nanomaterials as low-cost and high-performance counter electrodes of dye-sensitized solar cells. *Energy & Environmental Science,* **2013,** *6* (3), 835-840.

79. Dong, Z.; Lai, X.; Halpert, J. E.; Yang, N.; Yi, L.; Zhai, J.; Wang, D.; Tang, Z.; Jiang, L., Accurate control of multishelled ZnO hollow microspheres for dye-sensitized solar cells with high efficiency. *Advanced Materials,* **2012,** *24* (8), 1046-1049.

80. Bi, R.; Xu, N.; Ren, H.; Yang, N.; Sun, Y.; Cao, A.; Yu, R.; Wang, D., A hollow multi-shelled structure for charge transport and active sites in lithium-ion capacitors. *Angewandte Chemie International Edtion,* **2020,** *59* (12), 4865-4868.

81. Wang, X.; Feng, J.; Bai, Y.; Zhang, Q.; Yin, Y., Synthesis, properties, and applications of hollow micro-/nanostructures. *Chemical Reviews,* **2016,** *116* (18), 10983-11060.

82. Chen, D.; Li, F.; Ray, A. K., Effect of mass transfer and catalyst layer thickness on photocatalytic reaction. *AIChE Journal,* **2000,** *46* (5), 1034-1045.

83. Wang, L.; Wan, J.; Wang, J.; Wang, D., Small structures bring big things: performance control of hollow multishelled structures. *Small Structures,* **2020,** *2* (1), 2000041.

84. Jiangyan Wang, Y. C., Dan Wang, Design of hollow nanostructures for energy storage, conversion and production. *Advanced Materials,* **2018,** *31*, 1801993.

85. Wang, J.; Wan, J.; Wang, D., Hollow multishelled structures for promising applications: understanding the structure-performance correlation. *Accounts of Chemical Research,* **2019,** *52* (8), 2169-2178.

86. Huang, C. C.; Huang, W.; Yeh, C. S., Shell-by-shell synthesis of multi-shelled mesoporous silica nanospheres for optical imaging and drug delivery. *Biomaterials,* **2011,** *32* (2), 556-564.

87. Sun, H. H.; Juyoung. Y.; Jyongsik, J., Multi-shell porous TiO_2 hollow nanoparticles for enhanced light harvesting in dye-sensitized solar cells. *Advanced Functional Materials,* **2014,** *24*, 7619-7626.

88. Zhou, L.; Zhuang, Z.; Zhao, H.; Lin, M.; Zhao, D.; Mai, L., Intricate hollow structures: controlled synthesis and applications in energy storage and conversion. *Advanced Materials* **2017,** *29* (20), 1602914.

89. Xu, H.; Wang, W., Template synthesis of multishelled Cu_2O hollow spheres with a single-crystalline shell wall. *Angewandte Chemie International Edtion,* **2007,** *119* (9), 1511-1514.

90. Wu, C.; Zhang, X.; Ning, B.; Yang, J.; Xie, Y., Shape evolution of new-phased lepidocrocite VOOH from single-shelled to double-shelled hollow nanospheres on the basis of programmed reaction-temperature strategy. *Inorganic Chemistry,* **2009,** *48* (13), 6044-6054.

91. Zhang, G.; Xia, B. Y.; Xiao, C.; Yu, L.; Wang, X.; Xie, Y.; Lou, X. W., General formation of complex tubular nanostructures of metal oxides for the oxygen reduction reaction and lithium-ion batteries. *Angewandte Chemie International Edtion,* **2013,** *52* (33), 8643-8647.

92. Gonzalez, E.; Arbiol, J.; Puntes, V. F., Carving at the nanoscale: sequential galvanic exchange and Kirkendall growth at room temperature. *Science,* **2011,** *334* (6061), 1377-80.

93. Li, Z.; Lai, X.; Wang, H.; Mao, D.; Xing, C.; Wang, D., General synthesis of homogeneous hollow core−shell ferrite microspheres. *The Journal of Physical Chemistry C,* **2009,** *113* (7), 2792-2797.

94. Wang, J.; Yang, N.; Tang, H.; Dong, Z.; Jin, Q.; Yang, M.; Kisailus, D.; Zhao, H.; Tang, Z.; Wang, D., Accurate control of multishelled Co_3O_4 hollow microspheres as high-performance anode materials in lithium-ion batteries. *Angewandte Chemie International Edtion,* **2013,** *52* (25), 6417-6420.

95. Qi, J.; Zhao, K.; Li, G.; Gao, Y.; Zhao, H.; Yu, R.; Tang, Z., Multi-shelled $CeO_{(2)}$ hollow microspheres as superior photocatalysts for water oxidation. *Nanoscale,* **2014,** *6* (8), 4072-4077.

96. Chen, M.; Wang, J.; Tang, H.; Yang, Y.; Wang, B.; Zhao, H.; Wang, D., Synthesis of multi-shelled MnO_2 hollow microspheres via an anion-adsorption process of hydrothermal intensification. *Inorganic Chemistry Frontiers,* **2016,** *3* (8), 1065-1070.

97. Wei, Y.; Wan, J.; Yang, N.; Yang, Y.; Ma, Y.; Wang, S.; Wang, J.; Yu, R.; Gu, L.; Wang, L.; Wang, L.; Huang, W.; Wang, D., Efficient sequential harvesting of solar light by heterogeneous hollow shells with hierarchical pores. *National Science Review,* **2020,** *7* (11), 1638-1646.

98. Boyd, C. C.; Cheacharoen, R.; Leijtens, T.; McGehee, M. D., Understanding degradation mechanisms and improving stability of perovskite photovoltaics. *Chemical Reviews,* **2019,** *119* (5), 3418-3451.

99. Park, S.; Chang, W. J.; Lee, C. W.; Park, S.; Ahn, H.-Y.; Nam, K. T., Photocatalytic hydrogen generation from hydriodic acid using methylammonium lead iodide in dynamic equilibrium with aqueous solution. *Nature Energy,* **2016,** *2* (1), 16185.

100. Luo, C.; Ren, X.; Dai, Z.; Zhang, Y.; Qi, X.; Pan, C., Present perspectives of advanced characterization techniques in TiO_2-based photocatalysts. *ACS Applied Materials & Interfaces,* **2017,** *9* (28), 23265-23286.

101. Wang, Y.; Wan, J.; Ding, J.; Hu, J. S.; Wang, D., A rutile TiO_2 electron transport layer for the enhancement of charge collection for efficient perovskite solar cells. *Angewandte*

Chemie International Edtion, **2019,** *58* (28), 9414-9418.

102. Satoh, N.; Nakashima, T.; Yamamoto, K., Metastability of anatase: size dependent and irreversible anatase-rutile phase transition in atomic-level precise titania. *Scientific Reports,* **2013,** *3*, 1959.

103. Zhang, H.; Banfield, J. F., Understanding polymorphic phase transformation behavior during growth of nanocrystalline aggregates: insights from TiO_2. *The Journal of Physical Chemistry B,* **2000,** *104* (15), 3481-3487.

104. White, R. J.; Tauer, K.; Antonietti, M.; Titirici, M. M., Functional hollow carbon nanospheres by latex templating. *Journal of the American Chemical Society,* **2010,** *132* (49), 17360-17363.

105. Su, D.; Zhang, J.; Dou, S.; Wang, G., Polypyrrole hollow nanospheres: stable cathode materials for sodium-ion batteries. *Chemical Communications,* **2015,** *51* (89), 16092-16095.

106. Donath, E.; Sukhorukov, G. B.; Caruso, F.; Davis, S. A.; Möhwald, H., Novel hollow polymer shells by colloid-templated assembly of polyelectrolytes. *Angewandte Chemie International Edition,* **1998,** *37* (16), 2201-2205.

107. Xu, X.; Asher, S. A., Synthesis and utilization of monodisperse hollow polymeric particles in photonic crystals. *Journal of the American Chemical Society,* **2004,** *126* (25), 7940-7945.

108. Zhou, W.; Wang, C.; Zhang, Q.; Abruña, H. D.; He, Y.; Wang, J.; Mao, S. X.; Xiao, X., Tailoring pore size of nitrogen-doped hollow carbon nanospheres for confining sulfur in lithium-sulfur batteries. *Advanced Energy Materials,* **2015,** *5* (16), 1401752.

109. Du, F. H.; Li, B.; Fu, W.; Xiong, Y. J.; Wang, K. X.; Chen, J. S., Surface binding of polypyrrole on porous silicon hollow nanospheres for Li-ion battery anodes with high structure stability. *Advanced Materials,* **2014,** *26* (35), 6145-6150.

110. Dong, A.; Ren, N.; Tang, Y.; Wang, Y.; Zhang, Y.; Hua, W.; Gao, Z., General synthesis of mesoporous spheres of metal oxides and phosphates. *Journal of the American Chemical Society,* **2003,** *125* (17), 4976-4977.

111. Li, F.; Tang, D.-M.; Zhang, T.; Liao, K.; He, P.; Golberg, D.; Yamada, A.; Zhou, H., Superior performance of a Li-O_2 battery with metallic RuO_2 hollow spheres as the carbon-free cathode. *Advanced Energy Materials,* **2015,** *5* (13), 1500294.

112. Chen, G.; Desinan, S.; Rosei, R.; Rosei, F.; Ma, D., Hollow ruthenium nanoparticles with small dimensions derived from Ni@Ru core@shell structure: synthesis and enhanced catalytic dehydrogenation of ammonia borane. *Chemical Communications,* **2012,** *48* (64), 8009-8011.

113. Marinakos, S. M.; Novak, J. P.; Brousseau, L. C.; House, A. B.; Edeki, E. M.; Feldhaus, J. C.; Feldheim, D. L., Gold particles as templates for the synthesis of hollow polymer

capsules. control of capsule dimensions and guest encapsulation. *Journal of the American Chemical Society,* **1999,** *121* (37), 8518-8522.

114. Li, Z.; Zhang, J.; Lou, X. W., Hollow carbon nanofibers filled with MnO_2 nanosheets as efficient sulfur hosts for lithium-sulfur batteries. *Angewandte Chemie International Edition,* **2015,** *54* (44), 12886-12890.

115. Huang, X.; Yang, J.; Mao, S.; Chang, J.; Hallac, P. B.; Fell, C. R.; Metz, B.; Jiang, J.; Hurley, P. T.; Chen, J., Controllable synthesis of hollow Si anode for long-cycle-life lithium-ion batteries. *Advanced Materials,* **2014,** *26* (25), 4326-4332.

116. Ghadiri, E.; Taghavinia, N.; Zakeeruddin, S. M.; Grätzel, M.; Moser, J.-E., Enhanced electron collection efficiency in dye-sensitized solar cells based on nanostructured TiO_2 hollow fibers. *Nano Letters,* **2010,** *10* (5), 1632-1638.

117. Khapli, S.; Kim, J. R.; Montclare, J. K.; Levicky, R.; Porfiri, M.; Sofou, S., Frozen cyclohexane-in-water emulsion as a sacrificial template for the synthesis of multilayered polyelectrolyte microcapsules. *Langmuir,* **2009,** *25* (17), 9728-33.

118. Bourret, G. R.; Lennox, R. B., 1D $Cu(OH)_{(2)}$ nanomaterial synthesis templated in water microdroplets. *Journal of the American Chemical Society,* **2010,** *132* (19), 6657-6659.

119. Amstad, E.; Kim, S. H.; Weitz, D. A., Photo-and thermoresponsive polymersomes for triggered release. *Angewandte Chemie International Edition,* **2012,** *51* (50), 12499-12503.

120. Landsmann, S.; Luka, M.; Polarz, S., Bolaform surfactants with polyoxometalate head groups and their assembly into ultra-small monolayer membrane vesicles. *Nature Communications,* **2012,** *3*, 1299.

121. Shchukin, D. G.; Kohler, K.; Mohwald, H.; Sukhorukov, G. B., Gas-filled polyelectrolyte capsules. *Angewandte Chemie International Edition,* **2005,** *44* (21), 3310-3314.

122. Yunoki, A.; Tsuchiya, E.; Fukui, Y.; Fujii, A.; Maruyama, T., Preparation of inorganic/organic polymer hybrid microcapsules with high encapsulation efficiency by an electrospray technique. *ACS Applied Materials & Interfaces,* **2014,** *6* (15), 11973-11979.

123. Zhang, Q.; Zhang, T.; Ge, J.; Yin, Y., Permeable silica shell through surface-protected etching. *Nano Letters,* **2008,** *8* (9), 2867-2871.

124. Wang, J.; Tang, H.; Ren, H.; Yu, R.; Qi, J.; Mao, D.; Zhao, H.; Wang, D., pH-Regulated synthesis of multi-shelled manganese oxide hollow microspheres as supercapacitor electrodes using carbonaceous microspheres as templates. *Advanced Science,* **2014,** *1* (1), 1400011.

125. Sadhanala, H. K.; Khatei, J.; Nanda, K. K., Facile hydrothermal synthesis of carbon nanoparticles and possible application as white light phosphors and catalysts for the reduction of nitrophenol. *RSC Advances,* **2014,** *4* (22), 11481-11485.

126. Wang, H.; Wang, X.; Chen, R.; Zhang, H.; Wang, X.; Wang, J.; Zhang, J.; Mu, L.; Wu,

K.; Fan, F.; Zong, X.; Li, C., Promoting photocatalytic H_2 evolution on organic–inorganic hybrid perovskite nanocrystals by simultaneous dual-charge transportation modulation. *ACS Energy Letters,* **2018,** *4* (1), 40-47.

127. Zhao, H.; Lu, X.; Wang, Y.; Sun, B.; Wu, X.; Lu, H., Effects of additives on sucrose-derived activated carbon microspheres synthesized by hydrothermal carbonization. *Journal of Materials Science,* **2017,** *52* (18), 10787-10799.

128. Shi, Y.; Zhang, X.; Liu, G., Activated carbons derived from hydrothermally carbonized sucrose: remarkable adsorbents for adsorptive desulfurization. *ACS Sustainable Chemistry & Engineering,* **2015,** *3* (9), 2237-2246.

129. Zheng, M.; Liu, Y.; Jiang, K.; Xiao, Y.; Yuan, D., Alcohol-assisted hydrothermal carbonization to fabricate spheroidal carbons with a tunable shape and aspect ratio. *Carbon,* **2010,** *48* (4), 1224-1233.

130. Bedin, K. C.; Cazetta, A. L.; Souza, I. P. A. F.; Pezoti, O.; Souza, L. S.; Souza, P. S. C.; Yokoyama, J. T. C.; Almeida, V. C., Porosity enhancement of spherical activated carbon: influence and optimization of hydrothermal synthesis conditions using response surface methodology. *Journal of Environmental Chemical Engineering,* **2018,** *6* (1), 991-999.

131. Hanaor, D. A. H.; Sorrell, C. C., Review of the anatase to rutile phase transformation. *Journal of Materials Science,* **2010,** *46* (4), 855-874.

132. Luo, Z.; Poyraz, A. S.; Kuo, C.-H.; Miao, R.; Meng, Y.; Chen, S.-Y.; Jiang, T.; Wenos, C.; Suib, S. L., Crystalline mixed phase (Anatase/Rutile) mesoporous titanium dioxides for visible light photocatalytic activity. *Chemistry of Materials,* **2014,** *27* (1), 6-17.

133. Shiraishi, Y.; Togawa, Y.; Tsukamoto, D.; Tanaka, S.; Hirai, T., Highly efficient and selective hydrogenation of nitroaromatics on photoactivated rutile titanium dioxide. *ACS Catalysis,* **2012,** *2* (12), 2475-2481.

134. Günnemann, C.; Haisch, C.; Fleisch, M.; Schneider, J.; Emeline, A. V.; Bahnemann, D. W., Insights into different photocatalytic oxidation activities of anatase, brookite, and rutile single-crystal facets. *ACS Catalysis,* **2018,** *9* (2), 1001-1012.

135. Yang, Y.; Liu, G.; Irvine, J. T. S.; Cheng, H. M., Enhanced photocatalytic H_2 production in core-shell engineered rutile TiO_2. *Advanced Materials,* **2016,** *28* (28), 5850-5856.

136. An, X.; Hu, C.; Liu, H.; Qu, J., Hierarchical nanotubular anatase/rutile/TiO_2(B) Heterophase junction with oxygen vacancies for enhanced photocatalytic H_2 production. *Langmuir,* **2018,** *34* (5), 1883-1889.

137. Wenderich, K.; Mul, G., Methods, Mechanism, and applications of photodeposition in photocatalysis: a review. *Chemical Reviews,* **2016,** *116* (23), 14587-14619.

138. Zhao, D.; Yang, N.; Wei, Y.; Jin, Q.; Wang, Y.; He, H.; Yang, Y.; Han, B.; Zhang, S.; Wang, D., Sequential drug release via chemical diffusion and physical barriers enabled by

hollow multishelled structures. *Nature Communications,* **2020,** *11* (1), 4450.

139. Cai, C.; Teng, Y.; Wu, J. H.; Li, J. Y.; Chen, H. Y.; Chen, J. H.; Kuang, D. B., In situ photosynthesis of an $MAPbI_3$/CoP hybrid heterojunction for efficient photocatalytic hydrogen evolution. *Advanced Functional Materials,* **2020,** *30* (35), 2001478.

140. Guan, W.; Li, Y.; Zhong, Q.; Liu, H.; Chen, J.; Hu, H.; Lv, K.; Gong, J.; Xu, Y.; Kang, Z.; Cao, M.; Zhang, Q., Fabricating $MAPbI_3/MoS_2$ composites for improved photocatalytic performance. *Nano Letters,* **2021,** *21* (1), 597-604.

141. Zhu, Y.; Tian, P.; Jiang, H.; Mu, J.; Meng, L.; Su, X.; Wang, Y.; Lin, Y.; Zhu, Y.; Song, L.; Li, C., Synergistic effect of platinum single atoms and nanoclusters boosting electrocatalytic hydrogen evolution. *CCS Chemistry,* **2021,** *3* (10), 2539-2547.

142. Bresolin, B. M.; Hammouda, S. B.; Sillanpää, M., Methylammonium iodo bismuthate perovskite $(CH_3NH_3)_3Bi_2I_9$ as new effective visible light-responsive photocatalyst for degradation of environment pollutants. *Journal of Photochemistry and Photobiology A: Chemistry,* **2019,** *376*, 116-126.

143. Hu, J.; Lu, Y.; Liu, X.-L.; Janiak, C.; Geng, W.; Wu, S.-M.; Zhao, X.-F.; Wang, L.-Y.; Tian, G.; Zhang, Y.; Su, B.-L.; Yang, X.-Y., Photoinduced terminal fluorine and Ti^{3+} in $TiOF_2$ /TiO_2 heterostructure for enhanced charge transfer. *CCS Chemistry,* **2020,** *2* (6), 1573-1581.

144. Liu, F.; Wang, M.; Liu, X.; Wang, B.; Li, C.; Liu, C.; Lin, Z.; Huang, F., A rapid and robust light-and-solution-triggered in situ crafting of organic passivating membrane over metal halide perovskites for markedly improved stability and photocatalysis. *Nano Letters,* **2021,** *21* (4), 1643-1650.

145. Xia, B.; Yang, Y.; Zhang, Y.; Xia, Y.; Jaroniec, M.; Yu, J.; Ran, J.; Qiao, S.-Z., Metal-organic framework with atomically dispersed Ni–N_4 sites for greatly-raised visible-light photocatalytic H_2 production. *Chemical Engineering Journal,* **2022,** *431*, 133944.

146. Niu, P.; Dai, J.; Zhi, X.; Xia, Z.; Wang, S.; Li, L., Photocatalytic overall water splitting by graphitic carbon nitride. *InfoMat,* **2021,** *3* (9), 931-961.

147. Wang, L.; Xiao, H.; Cheng, T.; Li, Y.; Goddard, W. A., 3rd, Pb-activated amine-assisted photocatalytic hydrogen evolution reaction on organic-inorganic perovskites. *Journal of the American Chemical Society,* **2018,** *140* (6), 1994-1997.

148. Luo, J.; Zhang, W.; Yang, H.; Fan, Q.; Xiong, F.; Liu, S.; Li, D. S.; Liu, B., Halide perovskite composites for photocatalysis: A mini review. *EcoMat,* **2021,** *3* (1), e12079.

149. Li, R.; Li, X.; Wu, J.; Lv, X.; Zheng, Y.-Z.; Zhao, Z.; Ding, X.; Tao, X.; Chen, J.-F., Few-layer black phosphorus-on-$MAPbI_3$ for superb visible-light photocatalytic hydrogen evolution from HI splitting. *Applied Catalysis B: Environmental,* **2019,** *259*, *118075*.

150. Ran, J.; Zhang, H.; Qu, J.; Shan, J.; Davey, K.; Cairney, J. M.; Jing, L.; Qiao, S. Z., Significantly raised visible-light photocatalytic H_2 evolution on a 2D/2D ReS_2 /In_2 ZnS_4 van

der Waals Heterostructure. *Small,* **2021,** *17* (32), e2100296.

151. Su, D. W.; Ran, J.; Zhuang, Z. W.; Chen, C.; Qiao, S. Z.; Li, Y. D.; Wang, G. X., Atomically dispersed Ni in cadmium-zinc sulfide quantum dots for high-performance visible-light photocatalytic hydrogen production. *Science Advances,* **2020,** *6* (33), eaaz8447.

152. He, B.; Feng, M.; Chen, X.; Sun, J., Multidimensional (0D-3D) functional nanocarbon: promising material to strengthen the photocatalytic activity of graphitic carbon nitride. *Green Energy & Environment,* **2021,** *6* (6), 823-845.

153. Meng, Z.; Zhou, B.; Xu, J.; Li, Y.; Hu, X.; Tian, H., Heterostructured nitrogen and sulfur co-doped black TiO_2/g-C_3N_4 photocatalyst with enhanced photocatalytic activity. *Chemical Research in Chinese Universities,* **2020,** *36* (6), 1045-1052.

154. Zhang, J.; Hu, Y.; Li, H.; Cao, L.; Jiang, Z.; Chai, Z.; Wang, X., Molecular self-assembly of oxygen deep-doped ultrathin C_3N_4 with a built-in electric field for efficient photocatalytic H_2 evolution. *Inorganic Chemistry,* **2021,** *60* (20), 15782-15796.

155. Chen, T.; Zhong, L.; Yang, Z.; Mou, Z.; Liu, L.; Wang, Y.; Sun, J.; Lei, W., Enhanced visible-light photocatalytic activity of g-C_3N_4/nitrogen-doped graphene quantum dots/TiO_2 ternary heterojunctions for ciprofloxacin degradation with narrow band gap and high charge carrier mobility. *Chemical Research in Chinese Universities,* **2020,** *36* (6), 1083-1090.

156. Xia, B.; Zhang, Y.; Ran, J.; Jaroniec, M.; Qiao, S.-Z., Single-atom photocatalysts for emerging reactions. *ACS Central Science,* **2021,** *7* (1), 39-54.

157. Yin, Y.; Wei, S.; Zhang, L.; Guo, Z.; Huang, H.; Sai, S.; Wu, J.; Xu, Y.; Liu, Y.; Zheng, L.; Fan, X.; Cui, X., Copper-linked 1T MoS_2/Cu_2O heterostructure for efficient photocatalytic hydrogen evolution. *Chemical Research in Chinese Universities,* **2020,** *36* (6), 1122-1127.

158. Abdul Nasir, J.; Munir, A.; Ahmad, N.; Haq, T. U.; Khan, Z.; Rehman, Z., Photocatalytic Z-scheme overall water splitting: recent advances in theory and experiments. *Advanced Materials,* **2021,** *33* (52), e2105195.

159. Zhang, W.; Zong, X.; Luo, M.; Hua, M.; Zhu, L.; Liang, M.; Xue, S., Polymeric hole-transporting material with a flexible backbone for constructing thermally stable inverted perovskite solar cells. *Materials Chemistry Frontiers,* **2021,** *5* (19), 7241-7250.

160. Lopez, C. A.; Martinez-Huerta, M. V.; Alvarez-Galvan, M. C.; Kayser, P.; Gant, P.; Castellanos-Gomez, A.; Fernandez-Diaz, M. T.; Fauth, F.; Alonso, J. A., Elucidating the methylammonium (MA) conformation in $MAPbBr_3$ perovskite with application in solar cells. *Inorganic Chemistry,* **2017,** *56* (22), 14214-14219.

161. Wu, Y.; Li, X.; Zeng, H., Lead-free halide double perovskites: structure, luminescence, and applications. *Small Structures,* **2020,** *2* (3), 2000071.

162. Liu, Y.; Ono, L. K.; Qi, Y., Organic additive engineering toward efficient perovskite light-emitting diodes. *InfoMat,* **2020,** *2* (6), 1095-1108.

163. Zhou, Z.; Xu, J.; Liu, Y.; Wei, C.; Zhang, H.; Wang, Q., Zn-alloyed $MAPbBr_3$ crystals with improved thermoelectric and photocatalytic properties. *Materials Chemistry Frontiers,* **2021,** *5* (24), 8319-8332.

164. Chen, J.; Dong, C.; Idriss, H.; Mohammed, O. F.; Bakr, O. M., Metal halide perovskites for solar-to-chemical fuel conversion. *Advanced Energy Materials,* **2019,** *10* (13), 1902433.

165. Wang, H.; Zhang, H.; Wang, J.; Gao, Y.; Fan, F.; Wu, K.; Zong, X.; Li, C., Mechanistic understanding of efficient photocatalytic H_2 evolution on two-dimensional layered lead iodide hybrid perovskites. *Angewandte Chemie International Edition,* **2021,** *60* (13), 7376-7381.

166. Lee, S.; Jang, G. Y.; Kim, J. K.; Park, J. H., Solar-harvesting lead halide perovskite for artificial photosynthesis. *Journal of Energy Chemistry,* **2021,** *62*, 11-26.

167. Yang, M.-Z.; Xu, Y.-F.; Liao, J.-F.; Wang, X.-D.; Chen, H.-Y.; Kuang, D.-B., Constructing $CsPbBr_xI_{3-x}$ nanocrystal/carbon nanotube composites with improved charge transfer and light harvesting for enhanced photoelectrochemical activity. *Journal of Materials Chemistry A,* **2019,** *7* (10), 5409-5415.

168. Wu, Y.; Wang, P.; Zhu, X.; Zhang, Q.; Wang, Z.; Liu, Y.; Zou, G.; Dai, Y.; Whangbo, M. H.; Huang, B., Composite of $CH_3NH_3PbI_3$ with reduced graphene oxide as a highly efficient and stable visible-light photocatalyst for hydrogen evolution in aqueous HI solution. *Advanced Materials* **2018,** *30* (7), 1704342.

169. Wang, F.; Liu, X.; Zhang, Z.; Min, S., A noble-metal-free MoS_2 nanosheet-coupled $MAPbI_3$ photocatalyst for efficient and stable visible-light-driven hydrogen evolution. *Chemical Communications,* **2020,** *56* (22), 3281-3284.

170. Zhou, P.; Chen, H.; Chao, Y.; Zhang, Q.; Zhang, W.; Lv, F.; Gu, L.; Zhao, Q.; Wang, N.; Wang, J.; Guo, S., Single-atom Pt-I_3 sites on all-inorganic Cs_2SnI_6 perovskite for efficient photocatalytic hydrogen production. *Nature Communications,* **2021,** *12* (1), 4412.

171. Jiang, Y.; Liao, J.-F.; Chen, H.-Y.; Zhang, H.-H.; Li, J.-Y.; Wang, X.-D.; Kuang, D.-B., All-solid-state Z-scheme α-Fe_2O_3/Amine-RGO/$CsPbBr_3$ hybrids for visible-light-driven photocatalytic CO_2 reduction. *Chem,* **2020,** *6* (3), 766-780.

172. Wang, X.; Wang, H.; Zhang, H.; Yu, W.; Wang, X.; Zhao, Y.; Zong, X.; Li, C., Dynamic interaction between methylammonium lead iodide and TiO_2 nanocrystals leads to enhanced photocatalytic H_2 evolution from HI splitting. *ACS Energy Letters,* **2018,** *3* (5), 1159-1164.

173. Luo, J.; Yang, H.; Liu, Z.; Li, F.; Liu, S.; Ma, J.; Liu, B., Organic-inorganic hybrid perovskite-TiO_2 nanorod arrays for efficient and stable photoelectrochemical hydrogen evolution from HI splitting. *Materials Today Chemistry,* **2019,** *12*, 1-6.

174. Wu, L. Y.; Mu, Y. F.; Guo, X. X.; Zhang, W.; Zhang, Z. M.; Zhang, M.; Lu, T. B., Encapsulating perovskite quantum dots in iron-based metal-organic frameworks (MOFs) for efficient photocatalytic CO_2 reduction. *Angewandte Chemie International Edition,* **2019,** *58*

(28), 9491-9495.

175. Wang, M.; Zuo, Y.; Wang, J.; Wang, Y.; Shen, X.; Qiu, B.; Cai, L.; Zhou, F.; Lau, S. P.; Chai, Y., Remarkably enhanced hydrogen generation of organolead halide perovskites via piezocatalysis and photocatalysis. *Advanced Energy Materials,* **2019,** *9* (37), 1901801.

176. Zhao, Z.; Wu, J.; Zheng, Y.-Z.; Li, N.; Li, X.; Ye, Z.; Lu, S.; Tao, X.; Chen, C., Stable hybrid perovskite $MAPb(I_{1-x}Br_x)_3$ for photocatalytic hydrogen evolution. *Applied Catalysis B: Environmental,* **2019,** *253*, 41-48.

177. Zhang, Z.; Li, Y.; Liang, C.; Yu, G.; Zhao, J.; Luo, S.; Huang, Y.; Su, C.; Xing, G., In situ growth of $MAPbBr_3$ nanocrystals on few-layer MXene nanosheets with efficient energy transfer. *Small,* **2020,** *16* (17), e1905896.

178. Zhao, X.; Chen, S.; Yin, H.; Jiang, S.; Zhao, K.; Kang, J.; Liu, P. F.; Jiang, L.; Zhu, Z.; Cui, D.; Liu, P.; Han, X.; Yang, H. G.; Zhao, H., Perovskite microcrystals with intercalated monolayer MoS_2 nanosheets as advanced photocatalyst for solar-powered hydrogen generation. *Matter,* **2020,** *3* (3), 935-949.

179. Makula, P.; Pacia, M.; Macyk, W., How to correctly determine the band gap energy of modified semiconductor photocatalysts based on UV-Vis spectra. *The Journal of Physical Chemistry Letters,* **2018,** *9* (23), 6814-6817.

180. Gratzel, M., Photoelectrochemical cells. *Nature,* **2001,** *414* (6861), 338-344.

181. Kou, J.; Lu, C.; Wang, J.; Chen, Y.; Xu, Z.; Varma, R. S., Selectivity enhancement in heterogeneous photocatalytic transformations. *Chemical Reviews,* **2017,** *117* (3), 1445-1514.

182. Wang, H.; Zhang, L.; Chen, Z.; Hu, J.; Li, S.; Wang, Z.; Liu, J.; Wang, X., Semiconductor heterojunction photocatalysts: design, construction, and photocatalytic performances. *Chemical Society Reviews,* **2014,** *43* (15), 5234-5244.

183. Linsebigler, A. L.; Lu, G.; Yates, J. T., Photocatalysis on TiO_2 surfaces: principles, mechanisms, and selected results. *Chemical Reviews,* **2002,** *95* (3), 735-758.

184. Lin, H.; Ding, L.; Pei, Z.; Zhou, Y.; Long, J.; Deng, W.; Wang, X., Au deposited BiOCl with different facets: on determination of the facet-induced transfer preference of charge carriers and the different plasmonic activity. *Applied Catalysis B: Environmental,* **2014,** *160-161*, 98-105.

185. Tsai, M.-C.; Nguyen, T.-T.; Akalework, N. G.; Pan, C.-J.; Rick, J.; Liao, Y.-F.; Su, W.-N.; Hwang, B.-J., Interplay between molybdenum dopant and oxygen vacancies in a TiO_2 support enhances the oxygen reduction reaction. *ACS Catalysis,* **2016,** *6* (10), 6551-6559.

186. Deshlahra, P.; Schneider, W. F.; Bernstein, G. H.; Wolf, E. E., Direct control of electron transfer to the surface-CO bond on a Pt/TiO_2 catalytic diode. *Journal of the American Chemical Society,* **2011,** *133* (41), 16459-16467.

187. Leng, W. H.; Barnes, P. R. F.; Juozapavicius, M.; O'Regan, B. C.; Durrant, J. R., Electron

diffusion length in mesoporous nanocrystalline TiO_2 photoelectrodes during water oxidation. *The Journal of Physical Chemistry Letters,* **2010,** *1* (6), 967-972.

188. Wang, Q.; Fang, X.; Hao, P.; Ren, H.; Zhao, Y.; Huang, F.; Xie, J.; Cui, G.; Tang, B., Controllable fabrication of TiO_2 anatase/rutile phase junctions by a designer solvent for promoted photocatalytic performance. *Chemical Communications,* **2020,** *56* (79), 11827-11830.

189. Lee, J.-W.; Lee, T.-Y.; Yoo, P. J.; Grätzel, M.; Mhaisalkar, S.; Park, N.-G., Rutile TiO_2-based perovskite solar cells. *Journal of Materials Chemistry A,* **2014,** *2* (24), 9251-9259.

190. Zhu, Y.; Deng, K.; Sun, H.; Gu, B.; Lu, H.; Cao, F.; Xiong, J.; Li, L., TiO_2 phase junction electron transport layer boosts efficiency of planar perovskite solar cells. *Advanced Science,* **2018,** *5* (3), 1700614.

191. Yan, M.; Chen, F.; Zhang, J., Synthesis of controllable crystalline nano-TiO_2 at low temperature. *Chemistry Letters,* **2004,** *33* (10), 1352-1353.

192. Huang, Q.; Tian, S.; Zeng, D.; Wang, X.; Song, W.; Li, Y.; Xiao, W.; Xie, C., Enhanced photocatalytic activity of chemically bonded TiO_2/graphene composites based on the effective interfacial charge transfer through the C-Ti bond. *ACS Catalysis,* **2013,** *3* (7), 1477-1485.

193. Amorim, S. M.; Steffen, G.; de S Junior, J. M. N.; Brusamarello, C. Z.; Romio, A. P.; Domenico, M. D., Synthesis, characterization, and application of polypyrrole/TiO_2 composites in photocatalytic processes: a review. *Polymers and Polymer Composites,* **2020,** *29* (7), 1055-1074.

194. Liu, W.; Sun, M.; Ding, Z.; Zeng, Q.; Zheng, Y.; Sun, W.; Meng, X., Ball milling synthesis of porous g-C_3N_4 ultrathin nanosheets functionalized with alkynyl groups for strengthened photocatalytic activity. *Separation and Purification Technology,* **2022,** *282*, 120097.

195. Shen, Y.; Li, D.; Dang, Y.; Zhang, J.; Wang, W.; Ma, B., A ternary calabash model photocatalyst (Pd/MoP)/CdS for enhancing H_2 evolution under visible light irradiation. *Applied Surface Science,* **2021,** *564*, 150432.

196. Salvador, P., Analysis of the transient photocurrent-time behaviour of a sintered n-$SrTiO_3$, electrode in water photoelectrolysis. *Journal of Electroanalytical Chemistry,* **1984,** *160* (1-2), 117-130.

197. Baram, N.; Ein-Eli, Y., Electrochemical impedance spectroscopy of porous TiO_2 for photocatalytic applications. *The Journal of Physical Chemistry C,* **2010,** *114* (21), 9781-9790.

198. Zhang, D.; Cui, X.; Liu, L.; Xu, Y.; Zhao, J.; Han, J.; Zheng, W., 2D Bismuthene metal electron mediator engineering super interfacial charge transfer for efficient photocatalytic reduction of carbon dioxide. *ACS applied materials & interfaces,* **2021,** *13* (18), 21582-21592.

199. Baral, B.; Mansingh, S.; Reddy, K. H.; Bariki, R.; Parida, K., Architecting a double charge-transfer dynamics $In_2S_3/BiVO_4$ n-n isotype heterojunction for superior photocatalytic oxytetracycline hydrochloride degradation and water oxidation reaction: unveiling the association of physicochemical, electrochemical, and photocatalytic properties. *ACS Omega,* **2020,** *5* (10), 5270-5284.

200. Gao, X.; An, L.; Qu, D.; Jiang, W.; Chai, Y.; Sun, S.; Liu, X.; Sun, Z., Enhanced photocatalytic N_2 fixation by promoting N_2 adsorption with a co-catalyst. *Science Bulletin,* **2019,** *64* (13), 918-925.

201. Fan, J.; Xiong, J.; Liu, D.; Tang, Y.; He, S.; Hu, Z., A cathodic photocorrosion-assisted strategy to construct a CdS/Pt heterojunction photocatalyst for enhanced photocatalytic hydrogen evolution. *New Journal of Chemistry,* **2021,** *45* (23), 10315-10324.

202. Liu, Y.; Mu, K.; Zhang, Y.; Wang, L.; Yang, G.; Shen, F.; Deng, S.; Zhang, X.; Zhang, S., Facile synthesis of a narrow-gap titanium dioxide anatase/rutile nanofiber film on titanium foil with high photocatalytic activity under sunlight. *International Journal of Hydrogen Energy,* **2016,** *41* (24), 10327-10334.

List of Publications

[1] Wensheng, Han.; Yanze, Wei.; Jiawei, Wan.; Nobuyoshi, Nakagawa.; Dan, Wang.; Hollow Multishell-Structured TiO_2/$MAPbI_3$ Composite Improves Charge Utilization for Visible-Light Photocatalytic Hydrogen Evolution. *Inorg. Chem.,* **2022**, *61*, 5397-5404.

List of Participated Conferences